Interface Fracture in Composite Materials and Structures

Østergaard, Rasmus Christian

Publication date:
2008

Document Version
Publisher's PDF, also known as Version of record

Technical
University of
Denmark

Interface Fracture in Composite Materials and Structures

Rasmus C. Østergaard

PhD thesis

November 2007

DCAMM Special Report No. S102

Department of
Mechanical
Engineering

MEK

Solid Mechanics

Interface Fracture in Composite Materials and Structures

by

Rasmus C. Østergaard

Preface

This thesis is submitted in fulfillment with the requirements for obtaining the degree of Ph.D. in mechanical engineering. The work was carried out at the Material Research Department, Risø DTU and the Department of Mechanical Engineering, Solid Mechanics Dept., Technical University of Denmark in the period April 13, 2004 to November 9, 2007. The Ph.D. study was funded by the Danish Technical Research Council through a project entitled Interface Design of Composite Materials. The supervisers were Dr.techn. Viggo Tvergaard, Ph.D. Bent F. Sørensen and Ph.D. Lars P. Mikkelsen and I am very grateful for their qualifyed guidance and the many inspiring discussions. Furthermore, I wish to acknowledge my many collegues at Risø for creating a comfortable working invironment.

Finally, I wish to express my deepest gratitude to Sara and Emil who put up with being left in neglect in parts of my study.

Roskilde, November 9, 2007.

Rasmus C. Østergaard

Abstract

Fracture of composite materials and structures has been studied with special focus on the influence of material interface properties. The approaches depolyed include cohesive zone modeling integrated in a finite element framework and linear elastic fracture mechanics. Face sheet / core debonding of sandwich structures was studies from different perspectives: A LEFM analysis was used to analyse a sandwich-debonding fracture specimen that followingly was used for experimental investigations of face sheet/core debonding. An analysis of collapse of sandwich columns with initial debonds was conducted using a cohesive zone FE model. Furthermore, a micromechanical model of the composite failure mechanism cross-over fiber briding was developed to obtain fundamental understanding of how microscopical details on the fiber/matrix interface level link to composite fracture behavior. The results from the thesis indicate that interfaces play a very important role for the fracture properties of composite materials and structures and in the future improved composites can be manufactured by selecting the right interface properties for the composite.

Abstrakt

Brud i kompositmaterialer og strukturer er blevet studeret med speciel fokus på indflydelsen af materialegrænseflader. Metoderne som er blevet anvendt inkluderer kohæsiv-zone-modellering integreret i en finite-element model og lineær elastisk brudmekanik. Skind/kerne adskillelse in sandwichstrukturer er blevet undersøgt fra forskellige synsvinkler: En lineær elastisk brudmekanik-analyse blev anvendt til at analysere et sandwich brudprøveemne og dette blev derefter brugt til eksperimentelle målinger af skind/kerne brud. Kollaps af sandwich strukturer med skind/kerne-interfaceskader blev undersøgt med en kohæsiv-zone-FE-model. Desuden blev grundlæggende egenskaber for brud med fiber-overkrydsning studeret med en mikromekanisk model og fokus var på sammenhængen mellem fiber/matrix adhæsion og sejheden på kompositniveau. Samlet set indikerer resultaterne af afhandlingen at grænseflader spiller en meget vigtig rolle for kompositters brudegenskaber. På sigt kan vi forbedre kompositmaterialerne ved at vælge de rette egenskaber for grænsefladerne.

Publications

[P1] Østergaard, R. C. and Sørensen, B. F., 2007. *Interface crack in a sandwich specimen*, International Journal of Fracture **143**(4), 301-316.

[P2] Østergaard, R.C., Sørensen, B.F. and Brøndsted, P., 2007. *Measurement of interface fracture toughness of sandwich structures under mixed mode loadings*, Journal of Sandwich Structures and Materials **9**(5), 445-466.

[P3] Østergaard, R.C., *2008. Buckling driven debonding in sandwich structures,* International Journal of Solids and Structures **45**, 1264-1282.

[P4] Østergaard, R.C. and Sørensen, B. F., Prediction of composite scale cohesive laws for delamination with fiber bridging, Included as section 4.4, To be submitted.

Contents

1 Interface fracture of composite materials and composite structures

1.1 Introduction

Through the last decades composite materials have been increasingly used in large engineering structures, see figure 1. In primary structures of large aircrafts composite materials are used extensively. For instance, the center wing box in the Airbus A380-800 is a monolithic composite structure (Ferguson, 2004). Sandwich structures are also potential building elements for primary structures in aircrafts, but improved evaluation methods are still required to ensure structural reliability (Herrmann et al., 2006). Wind turbine blades are complex composite structures and consist of fiber laminates, adhesive joints and sandwich structures. The blades have lengths reaching beyond 60 meters and the demands for the materials are increasing in order to make the blades even longer and more durable (Brøndsted et al., 2005), (Thomsen, 2006).

To improve the materials and their reliability it is important to understand the mechanics of the materials. This can be done through modeling and experiments. When we have an understanding of the mechanics of the materials we can start to tailor the materials to get the most optimum properties. Based on a range of experimental and theoretical studies, the present thesis aims at improving our understanding of the fracture mechanics of composite structures and materials.

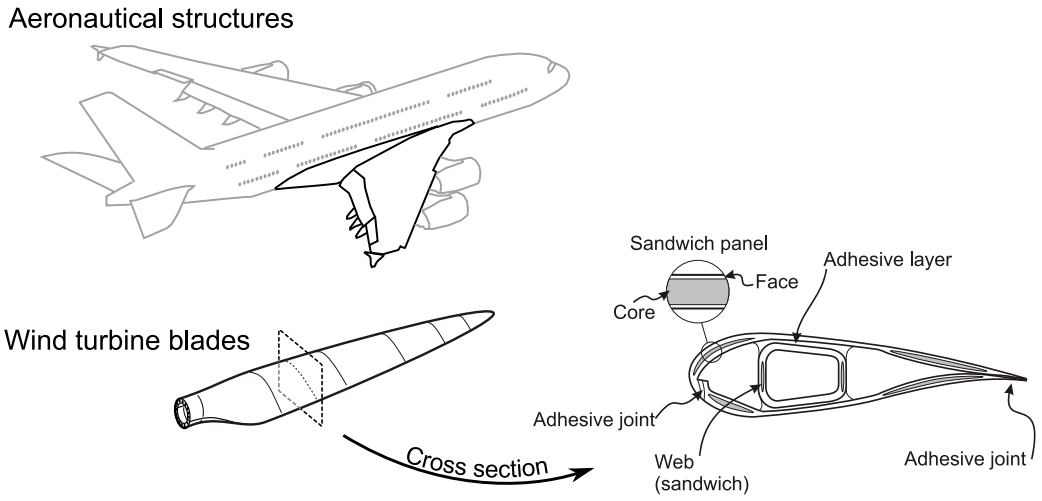

Figure 1: Large engineering structures containing composite materials and structures.

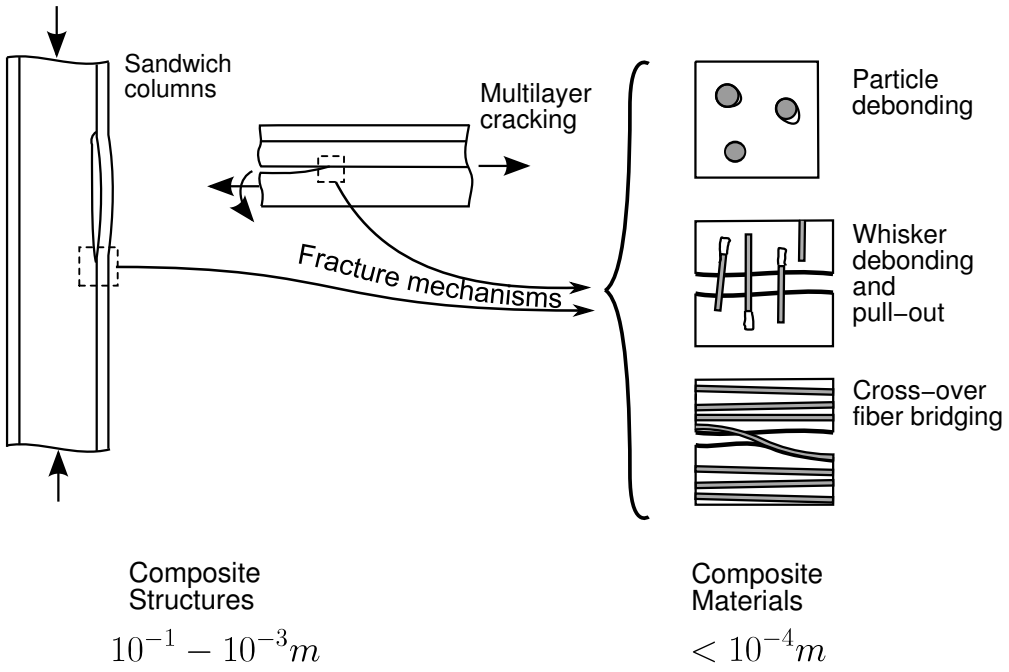

Figure 2: Structural response and failure modes are often influenced by the microstructural features and behavior of interfaces. Left side: Composite structures for which interfaces play an important role. Right side: Composite material failure-mechanisms for which interface properties play an important role.

Material interfaces comprise an integral element of composite materials and structures and in many situations the mechanics of interfaces plays an important role for the endurance properties. The studies that form this thesis apply fracture mechanics to model the influence of interfaces on the performance of composite materials and structures. Figure 2 shows some composite materials and composite structures for which interfaces play an important role. Amongst the examples in figure 2, interface fracture in sandwich structures and delamination by cross-over fiber bridging will be studied in detail.

Sandwich structures are lightweight (multi-layer) construction elements that are used in aeronautical structures, boats, wind turbine blades etc. Sandwich structures possess high specific bending stiffness and high buckling resistance when subjected to in-plane loads. The structural integrity of the sandwich structure is closely connected to the interface between the face sheet and the core. If the sandwich structure contains a debonded area as the sandwich structure in figure 2, a weak zone is formed. As a result the struc-

ture can suffer an abrupt collapse. In the papers [P1], [P2] and [P3] aspects of interface fracture of sandwich structures are studied: Paper [P1] contains a theoretical analysis of face sheet/core interface fracture in an isotropic sandwich specimen. Paper [P2] is an experimental study that concerns measurements of face sheet/core interface fracture toughness of two sandwich structure systems. The tested sandwich structures consist of glass/polyester face sheet laminates and PVC foam cores. Paper [P3] concerns a numerical model of a compression loaded sandwich column containing an initial interface debond. The results in [P3] provide insight on the influence of geometrical imperfections and face sheet/core interface fracture properties on the collapse of sandwich columns.

Several failure mechanisms of composite materials are closely related to interface fracture. These are typically related to the micron length scale. In figure 2 some failure mechanisms of composite materials are shown; particle debonding, fiber pull-out, fiber bridging etc. In the present thesis, cross-over fiber bridging is studied. The cross-over fiber bridging is observed experimentally in a wide range of fibrous composite materials. Typically, cross-over fiber bridging is the main contributor to delamination fracture toughness: As the crack faces are separated, the bridging fiber is detached from the matrix material by interface crack growth. The force from each bridging fiber is very low but typically fiber bridging is characterized by many bridging fibers. The opening of the crack faces is significant and therefore the mechanism accounts for large total energy dissipation. The fiber bridging mechanism is studied in the paper [P4] (that at time of writing only comprises a manuscript draft that is included in its full length in section 4.4).

A common element connecting the studies is fracture mechanics applied to interfaces. Therefore, I will initially present a review of interface fracture mechanics. The review starts off by a brief historical review (section 1.2). Next, a comprehensive theoretical review is given (section 2 and 3). After this, a summary of the major results obtained in the Ph.D. work is given (section 4). The thesis is rounded off by discussion and conclusion.

1.2 Fracture mechanics in a historical perspective

Linear elastic fracture mechanics

The first steps towards establishing fracture mechanics as a scientific field were taken by Griffith almost one century ago, in 1920. His study concerned fracture of brittle glass. The basic idea of Griffith's theory was that there is a driving force for crack extension (that results from the release of potential energy in the body) along with an inherent resistance against crack extension.

This resistance was believed to be associated with surface energy γ needed to create new surface. Although these early results created the foundation for the fracture mechanics field they were not directly applicable to the practical design of engineering structures.

After the Second World War Griffith's understanding of fracture was improved by Irwin and Kies (1952) and Orowan (1948) who realized that in metallic materials plastic flow around a crack tip also contributes to the resistance against crack growth. Later, it was realized that other energy dissipating mechanisms can also add to the resistance against crack growth (e.g. crack bridging mechanisms).

An important aspect of Irwin's developments is that the energy release rate of Griffith was related to the singular near crack-tip stresses that had already been identified by Inglis (1913). The stress intensity factor, K, was introduced and was calculated by various methods for a wide range of practical engineering structures e.g. Sih et al. (1961), Tada (1985). Nowadays, the theory is known as linear elastic fracture mechanics (LEFM) and it is has been widely used in the practical analysis and design of engineering structures.

Since Irwin's work in the 1950's, fracture mechanics has undergone an intense development and some subfields have emerged; for instance, LEFM for cracking along interfaces between elastically dissimilar materials. This is of special interest for many advanced composite materials. The interface crack tip stress field was determined by Williams (1959) but the results were difficult to interpret and did not gain widespread success until three decades later. In 1988 Rice proposed a sound interpretation of the interface crack tip fields in terms of an energy release rate and a mode mixity.

On the experimental front, LEFM was used as a framework to characterize and determine the fracture properties of interfaces. The results indicated that the fracture toughness of weak interfaces depends on the mode mixity e.g. (Liechti and Chai, 1992). Therefore, the determination of mode mixity has taken a central role in the analysis of interface fracture problems (Hutchinson and Suo, 1992).

Nonlinear fracture mechanics

LEFM is based on linear elasticity. However, for many construction materials the crack tip is strongly influenced by nonlinear mechanisms and LEFM is therefore insufficient. Barenblatt (1959) and Dugdale (1960) worked with the concept of cohesive forces for modeling nonlinear fracture. Barenblatt's theory supposes that cohesive forces hold the crack faces together in a zone near the crack tip. As the loading increases the cohesive forces at the crack

tip also will increase. However, since there is a limit to a materials ability to restrain the crack faces from opening, crack growth will eventually take place. Cohesive zone modeling (CZM) has shown to be adequate for the modeling of fracture in composite structures that can fail by large-scale-bridging (LSB) e.g. (Bao and Suo, 1992b).

The cohesive zone approach gained increased popularity after Needleman (1987) adopted the cohesive zone concept into FEM. Recently, several complex fracture/solid interaction problems have been understood from results obtained by CZM/FEM e.g. (Tvergaard and Hutchinson, 1993). New computational methods such *partition of unity* also uses cohesive zones to allow for crack growth along paths that are not predefined (contrary to ordinary FEM implementation where cracking paths typically are predefined) *e.g.* (Remmers et al., 2003).

2 Linear elastic fracture mechanics for interfaces

Linear elastic fracture mechanics (LEFM) is a theory for the fracture of solids for which the extent of non-linear and inelastic deformations is confined within a small zone in the neighborhood of the crack tip. What "small" is in this context, I will briefly return to in section 3.2.

Crack propagation in a homogeneous material follows a direction where the crack is in mode I loading i.e. perpendicular to the principal stress direction. For a crack propagating in an interface between dissimilar materials this is rarely the case. Then, the crack may not be free to kink into the direction where pure mode I conditions prevail (He and Hutchinson, 1989). Consequently, crack propagation along an interface is generally a mixed mode fracture problem and both shear and normal stresses exist in front of the crack tip.

In the present section LEFM for cracks along interfaces is summarized. First we introduce the mechanics of an interface crack between two *isotropic* solids which is used in [P1]. Next, we present the generalization to cracking between *orthotropic* media that is used in [P2].

2.1 Mechanics of an interface crack between two isotropic elastic solids

The crack is located between two isotropic elastic solids denoted #1 and #2, see figure 3. The materials are joined along the interface at $x_2 = 0$

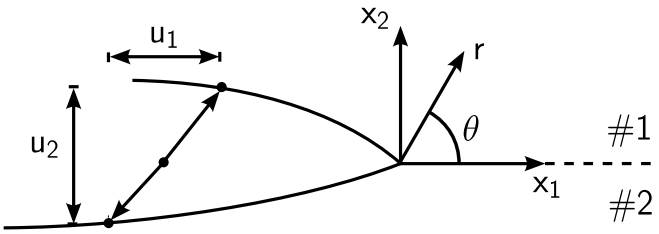

Figure 3: Interface crack

with material #1 above and material #2 below. Let μ_i, E_i and ν_i $(i = 1, 2)$ denote the shear modulus, Young's modulus and the Poisson's ratio, of the respective materials.

Having introduced the problem, one can see that four material parameters (two Poisson's ratios and two Young's moduli) uniquely define the materials. In a dimensionless framework these parameters can be reduced to three. However, Dundurs (1969) showed that under certain restrictions only two non-dimensional material parameters influence the stress field. The two parameters have been referred to as the Dundurs' elastic mismatch parameters:

$$\alpha = \frac{\mu_1(\kappa_2 + 1) - \mu_2(\kappa_1 + 1)}{\mu_1(\kappa_2 + 1) + \mu_2(\kappa_1 + 1)} \text{ and } \beta = \frac{\mu_1(\kappa_2 - 1) - \mu_2(\kappa_1 - 1)}{\mu_1(\kappa_2 + 1) + \mu_2(\kappa_1 + 1)}, \qquad (1)$$

where $\kappa_i = 2 - 4\nu_i$ for plane strain and $\kappa_i = (3 - \nu_i)/(1 + \nu_i)$ for plane stress conditions.

The Dundurs' elastic mismatch parameters have been used in a wide range of parameter studies e.g. Bogy (1971). In [P1] a parameter study is also conducted in terms of the Dundurs parameters. However, in [P1] α is interchanged with a (for that problem) more convenient parameter

$$\Sigma = \frac{\bar{E}_1}{\bar{E}_2}, \qquad (2)$$

where $\bar{E}_i = E_i/(1 - \nu_i^2)$ under plane strain conditions and $\bar{E}_i = E_i$ in a plane stress situation. α is related to Σ via the relation $\Sigma = (\alpha + 1)/(1 - \alpha)$, whereby it can be seen that α is actually a measure of the mismatch of the Young's moduli. β is interpreted as a measure of the bulk-modulus mismatch (Hutchinson and Suo, 1992). Using Dundurs' mismatch parameters, parameter studies become more viable to conduct since fewer parameters must be varied to determine influence of the elastic mismatch over the interface.

The singular stress field in the vicinity of the interface crack tip was first derived by Williams (1959) but here we adopt the notation by Rice

(1988). The stress field is taken as a first order solution to the Muskhelishvili representation of the problem since this includes the singular stresses that dominate at the crack tip

$$\sigma_{kl} = \Re[Kr^{i\epsilon}](2\pi r)^{-1/2}\sigma_{kl}^{I}(\theta,\,\epsilon) + \Im[Kr^{i\epsilon}](2\pi r)^{-1/2}\sigma_{kl}^{II}(\theta,\,\epsilon), \qquad (3)$$

here $i = \sqrt{-1}$, r is the radial distance from the crack tip, k and l are indices that can take the values 1 and 2 and $r^{i\epsilon} = \cos(\epsilon \ln r) + i \sin(\epsilon \ln r)$. ϵ is referred to as *the oscillatory parameter* which is given as

$$\epsilon = \frac{1}{2\pi} \ln\left(\frac{1-\beta}{1+\beta}\right). \qquad (4)$$

$\Im$, $\Re$ denote the imaginary and real parts, respectively. K is the complex stress intensity factor

$$K = K_1 + iK_2, \qquad (5)$$

σ_{kl}^{I} and σ_{kl}^{II} are non-dimensional trigonometric functions that prescribe the stress variation with the angle θ, they are given in (Rice et al., 1990).

For the studies in the present thesis, the elastic field along a line defined by $\theta = 0$ is needed. For $\theta = 0$ equation 3 can be rewritten as

$$\sigma_{22} + i\sigma_{12} = (K_1 + iK_2)(2\pi r)^{-1/2} r^{i\epsilon}. \qquad (6)$$

The crack opening components Δu_j are defined from the displacements u_j of two material points coinciding in the undeformed state

$$\Delta u_j = u_j(r, \theta = \pi) - u_j(r, \theta = -\pi), \qquad (7)$$

where, j takes the values 1 and 2, which refer to the directions in the coordinate system in figure 3. The crack opening components are related to the complex stress intensity factor, K, through

$$\Delta u_2 + i\Delta u_1 = \frac{c_1 + c_2}{2\sqrt{2\pi}(1 + 2i\epsilon)\cosh(\pi\epsilon)} K r^{i\epsilon + 1/2}, \qquad (8)$$

where

$$c_m = \frac{\kappa_m + 1}{\mu_m},$$

here $m = 1$ for material #1 and $m = 2$ for material #2, respectively. The factor $r^{i\epsilon}$ that has been referred to as the oscillatory singularity brings some complications into the problem. For instance, it predicts overlapping of the crack faces very close to the crack tip (Rice, 1988). In practice this overlapping has not been attributed with great importance. It has been discussed

that fracture toughness measurements may be influenced by frictional forces that result from this overlapping (in reality contact) (Liechti and Chai, 1992).

From (6) and (8) it can be seen that K has the following form

$$K = \sigma C L^{i\epsilon+1/2}, \tag{9}$$

where σ has units [stress] C is a complex number and $L^{i\epsilon+1/2}$ has units [length raised to $i\epsilon+1/2$]. This peculiar unit makes the interpretation of K difficult. However, K can be related to two other parameters that are more practical for describing the singularity (Rice, 1988): The energy release rate G with units $[J/m^2]$ and the mode mixity ψ with units $[radians]$. The complex stress intensity factor, K, can be related to the energy release rate (Malyshev and Salganik, 1965) through

$$G = \frac{c_1 + c_2}{16\cosh^2(\pi\epsilon)}|K|^2, \tag{10}$$

where $|K|$ is the modulus of K. G is a measure of the potential energy released from the body for an infinitesimal crack advance.

A definition of the mode mixity is complicated: First, let us consider a case where $\beta = 0$. Then, also $\epsilon = 0$ and the oscillatory singularity $r^{i\epsilon}$ equals unity. In this case the definition of mode mixity is straightforward and can be defined as the amount of mode 2 to mode 1 at the crack tip:

$$\psi = \tan(K_2/K_1). \tag{11}$$

However, in the general case ($\epsilon \neq 0$) K_1, K_2 have different units and (11) would give no meaning. To bypass this problem, Rice (1988) introduced an arbitrary chosen length ℓ and defined the mode mixity as the phase angle of $K\ell^{i\epsilon}$

$$\psi = \tan^{-1}\left[\frac{\Im(K\ell^{i\epsilon})}{\Re(K\ell^{i\epsilon})}\right]. \tag{12}$$

The choice of ℓ truly is arbitrary, furthermore Hutchinson and Suo (1992) have shown that ψ is only weakly affected by the actual choice of ℓ.

A criterion for crack growth is

$$G = G_c(\psi), \tag{13}$$

where $G_c(\psi)$ is the interface fracture toughness. It must be noted that ψ in the crack growth criterion (13) is calculated with a specific ℓ. Therefore, a given material dataset $G_c(\psi)$ must be accompanied with the value of ℓ used to calculate ψ.

The dependence on the mode mixity has been observed experimentally for different materials combinations. For instance, for a glass/epoxy interface the fracture toughness is as much as 10 times higher for $\psi \approx 90°$ than for $\psi \approx 0°$ (Liechti and Chai, 1992). For crack growth in weak interfaces between elasto-plastic materials the variation with mode mixity has been explained by increasing plastic deformation for ψ approaching 90° (Tvergaard and Hutchinson, 1993). However, as it will be shown later other micro mechanisms such as cross-over fiber bridging can also show a dependence on the mode of loading.

2.2 Mechanics of an interface crack between orthotropic elastic solids

In the previous section LEFM for interfaces was summarized. However, those results are limited to crack growth between isotropic solids. In [P2] the corresponding equations for crack growth between an isotropic and an orthotropic solid are required.

The elastic deformations in the materials are described by the following relation between the stress vector, σ_i, and the strain vector, ϵ_i

$$\epsilon_i = \sum_{j=1}^{6} s'_{ij}\sigma_j, \qquad i = 1 \text{ to } 6, \tag{14}$$

where

$$\epsilon_i = \epsilon_{11}, \epsilon_{22}, \epsilon_{33}, 2\epsilon_{23}, 2\epsilon_{13}, 2\epsilon_{12},$$
$$\sigma_i = \sigma_{11}, \sigma_{22}, \sigma_{33}, \sigma_{23}, \sigma_{13}, \sigma_{12},$$

and the compliance matrix s'_{ij} is given by (Lekhnitskii, 1981)

$$s'_{ij} = \begin{cases} s_{ij} & \text{for plane stress} \\ s_{ij} - s_{i3}s_{j3}/s_{33} & \text{for plane strain,} \end{cases}$$

i, j relate to the directions in the coordinate system in figure 3. The relation between the engineering constants and the compliance matrices for an orthotropic and an isotropic material can be found in various text books e.g. Jones (1975). For an orthotropic material:

$$s_{ij} = \begin{bmatrix} \frac{1}{E_{11}} & -\frac{\nu_{21}}{E_{22}} & -\frac{\nu_{31}}{E_{33}} & 0 & 0 & 0 \\ -\frac{\nu_{12}}{E_{11}} & \frac{1}{E_{22}} & -\frac{\nu_{32}}{E_{33}} & 0 & 0 & 0 \\ -\frac{\nu_{13}}{E_{11}} & -\frac{\nu_{23}}{E_{22}} & \frac{1}{E_{33}} & 0 & 0 & 0 \\ 0 & 0 & 0 & \frac{1}{G_{23}} & 0 & 0 \\ 0 & 0 & 0 & 0 & \frac{1}{G_{31}} & 0 \\ 0 & 0 & 0 & 0 & 0 & \frac{1}{G_{12}} \end{bmatrix} \tag{15}$$

A full characterization of an orthotropic material in terms of these constants is a comprehensive task that involves non-standard material tests (Toftegaard and Goutianos, 2007).

For an isotropic material the compliance matrix is:

$$s_{ij} = \frac{1}{E} \begin{bmatrix} 1 & -\nu & -\nu & 0 & 0 & 0 \\ -\nu & 1 & -\nu & 0 & 0 & 0 \\ -\nu & -\nu & 1 & 0 & 0 & 0 \\ 0 & 0 & 0 & 2(1+\nu) & 0 & 0 \\ 0 & 0 & 0 & 0 & 2(1+\nu) & 0 \\ 0 & 0 & 0 & 0 & 0 & 2(1+\nu) \end{bmatrix} \tag{16}$$

The shear stress σ_{12} and the normal stress σ_{22} in front of the crack tip are given by (Suo, 1989):

$$\sqrt{\frac{H_{22}}{H_{11}}}\sigma_{22} + i\sigma_{12} = \frac{1}{\sqrt{2\pi}} K r^{i\epsilon - 1/2}, \tag{17}$$

where ϵ is the oscillatory index given by (4), where the β is a generalization of the Dundurs parameter

$$\beta = \frac{[(s'_{11}s'_{22})^{1/2} + s'_{12}]_{\#2} - [(s'_{11}s'_{22})^{1/2} + s'_{12}]_{\#1}}{\sqrt{H_{11}H_{22}}}, \tag{18}$$

where #1 and #2 refer to material #1 and material #2, respectively. The parameters H_{11} and H_{22} are given by

$$H_{11} = \left[2m\widehat{\lambda}^{1/4}(s'_{11}s'_{22})^{1/2}\right]_{\#1} + \left[2m\widehat{\lambda}^{1/4}(s'_{11}s'_{22})^{1/2}\right]_{\#2} \tag{19}$$

and

$$H_{22} = \left[2m\widehat{\lambda}^{-1/4}(s'_{11}s'_{22})^{1/2}\right]_{\#1} + \left[2m\widehat{\lambda}^{-1/4}(s'_{11}s'_{22})^{1/2}\right]_{\#2}, \tag{20}$$

where $m = \sqrt{\frac{(1+\rho)}{2}}$,

$$\widehat{\lambda} = \frac{s'_{11}}{s'_{22}} \tag{21}$$

and

$$\rho = \frac{2s'_{12} + s'_{66}}{2\sqrt{s'_{11}s'_{22}}}, \tag{22}$$

Note that in order to compute ρ the compliance parameter s_{66} is needed. This involves the determination of G_{12} which according to figure 3 is an out-of-plane shear stiffness. This is complicated to measure.

The crack opening components (eq. 7) are related to the complex stress intensity factor, K, through

$$\sqrt{\frac{H_{11}}{H_{22}}}\Delta u_2 + i\Delta u_1 = \frac{2H_{11}Kr^{i\epsilon+1/2}(2\pi)^{1/2}}{(1+2i\epsilon)\cosh(\pi\epsilon)}, \tag{23}$$

and the energy release rate is related to the complex stress intensity factor through

$$G = \frac{H_{11}}{4\cosh^2(\pi\epsilon)}\left|K\right|^2. \tag{24}$$

The mode mixity is defined as for isotropic materials, see equation 12.

For interfaces between isotropic materials, the stress field depends only on the material mismatch through the two Dundurs elastic mismatch parameters. For interfaces between orthotropic materials a reduction of the number of dependent material parameters can also be made: For the sandwich structure analyzed in [P2] the crack is located between an isotropic core and an orthotropic face sheet. The total number of material constants characterizing the materials is: 9 for the face sheet and 2 for the core, cf. (15) and (16). However, these can be reduced to (Suo, 1989):

ρ, $\hat{\lambda}$	characterizing the orthotropy of the face sheet
Σ, β	characterizing the elastic mismatch over the interface,

where

$$\Sigma = \frac{(s'_{11})^{\#2}}{(s'_{11})^{\#1}},$$

consequently, the problem is reduced by seven parameters. Furthermore, results by Bao et al. (1992) have indicated that the stress field is only moderately dependent on ρ (however, a more extended study would be desirable since their study was based on a narrow selection of ρ values). From a

practical point of view, insensitivity to ρ is an attractive feature since the engineering constants that goes into determining ρ are difficult to measure. Instead, a rough estimate of ρ could be used. This approach was not used in [P2], but it could have reduced the experimental work in determining the compliance constants. Further reduction of certain orthotropic problems can be obtained through a orthotropic rescaling technique (Suo et al., 1991).

LEFM has been widely used for modeling fracture of composites. The mathematical framework of LEFM can be used for making analytical analysis of even complex problems. Paper [P1] serves as an example to this. In that paper the complexity of a problem is reduced by using LEFM. For instance it shown that the mode mixity can be determined analytically apart from a single load-independent parameter (that only varies slowly for fairly alike material combinations and geometries).

LEFM solutions (determination of K_I and K_{II} for homogeneous materials and determination of $K = K_1 + iK_2$ for interfaces) can often be calculated and presented in tables so the stress field for any relevant specimen proportion or crack length can be calculated easily. This has given engineers easy to use results for fracture in real engineering structures. Stress fields for various homogeneous specimens of engineering relevance can be found in e.g. Tada (1985). Solutions for cracking along interfaces in layered structures can be found in e.g. (Suo and Hutchinson, 1989), (Suo and Hutchinson, 1990), (Hutchinson and Suo, 1992), (Li et al., 2004) and paper [P1] in this thesis.

For problems where analytical methods do not suffice and the literature does not contain any usable results, numerical methods based on FEM can be deployed. For cracking of homogeneous media the VCCT method first used by Rybicki and Kanninen (1977) can be invoked. For interface cracking where both K_1 and K_2 must be determined a method was suggested by Matos et al. (1989). For cracking between orthotropic materials methods are proposed by Beuth (1996) and Charalambides and Zhang (1996). Alternatively, integral equations can be used (Suo and Hutchinson, 1990). In paper [P1] and [P2] yet another FEM based method is proposed for extracting the crack tip parameters of interface fracture problems.

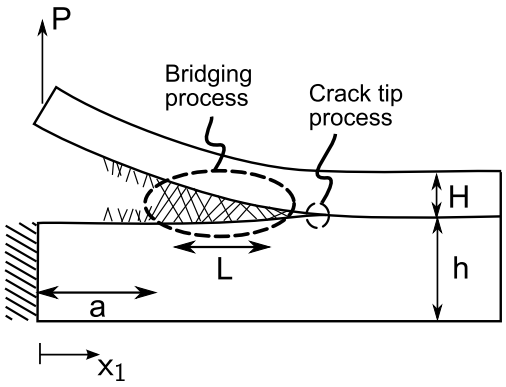

Figure 4: The fracture process of a composite can be decomposed into a bridging prosess and a crack tip process.

3 Cohesive zone modeling

3.1 Fundamental aspects of cohesive zone modeling

Within LEFM the fracture process is characterized by a single material parameter G_c (that can be a function of mode mixty, ψ). This parameter denotes the energy dissipation of the fracture mechanism that is assumed to be active only in a small zone near the crack tip. The external loading and geometry of the specimen is communicated to the fracture process only through the crack tip singularity (characterized by stress intensity factor K).

For many composite materials crack bridging mechanisms are involved in the fracture process, see figure 2. For such composites, the fracture process can normally be divided into a crack tip process and a bridging process where particles, fibers or material ligaments bridge the crack faces e.g. (Yang and Cox, 2005), see figure 4. The bridging mechanisms typically accounts for the majority of the fracture resistance. The length, L, of the bridging zone will often be significant in comparison with other characteristic lengths of the specimen (crack length a, heights H, h, width W etc.). This situation is referred to as large-scale-bridging (LSB) and it causes LEFM to loose its validity: Under LSB the fracture process interacts with the global stresses through the bridging forces on a finite sized zone on the crack faces. Therefore, the stress intensity parameter, K, (that only characterizes the crack tip stresses) becomes inadequate as a measure of the stresses transferred into the fracture process zone.

Cohesive zone modeling constitutes a more detailed way of considering fracture. In cohesive zone modeling the continuum deformations and the fracture process are modeled by separate laws, see figure 5a. The continuum

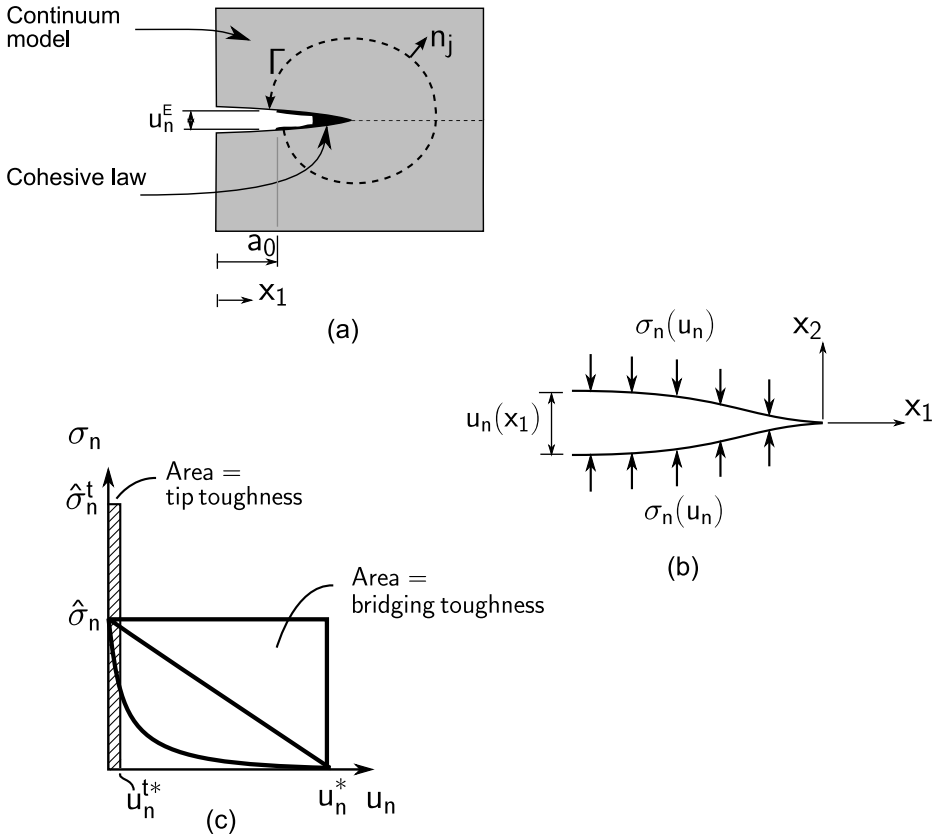

Figure 5: Principles of cohesive zone modeling for a mode I problem.

is represented by a continuum model and the fracture process is represented by tractions on the crack faces.

Considering pure normal crack-opening, the normal tractions σ_n on the crack faces are typically functions of the crack face openings $u_n(x_1)$ (see figure 5b).

$$\sigma_n = \sigma_n(u_n). \tag{25}$$

The traction functions are often referred to as cohesive laws. Some examples of cohesive laws are shown in figure 5c: When the stress on the interface, σ_n, reaches the peak stress, $\hat{\sigma}$, the fracture mechanism is activated (before that point, all deformation is accommodated by the continuum). The activation of the fracture mechanism is associated with crack face opening. Increasing the crack face opening at a given point the tractions change and at a critical opening, u_n^*, the stress reaches zero because the material has ultimately failed.

The actual shape of the cohesive law must be determined by micro-

mechanical modeling or through experiments. Bridging response of fiber-pull-out in ceramics has been studied by Marshall et al. (1985), Hutchinson and Jensen (1990), Budiansky et al. (1995), Cross-over fiber bridging has been studied experimentally and through modeling by Spearing and Evans (1992), Kaute et al. (1993), Sørensen (2003, 2006, 2007). As an alternative to cohesive laws for specific mechanisms, several modeling studies have been conducted using phenomenological cohesive laws e.g. (Needleman, 1987), (Tvergaard and Hutchinson, 1992) etc. Higher-order cohesive laws also exist. For instance, Tvergaard and Hutchinson (1996) proposed a cohesive zone that not only dependents on the crack opening but also on the plastic straining along the crack path.

An important tool in non-linear fracture mechanics is the J integral (Rice, 1968)

$$J = \int_\Gamma \Phi dy - \sigma_{ij} n_j \frac{\partial u_i}{\partial x_1} ds,$$

where Γ can be any path with normal n_j going counterclockwise from crack face to crack face, see figure 5a. Φ is the strain energy density $\Phi = \int_0^\epsilon \sigma_{ij} d\epsilon_{ij}$. Evaluating the J integral around the fracture process links the cohesive law to the fracture resistance (Bao and Suo, 1992b)

$$J_R = \int_0^{u_n^E} \sigma_n \delta u_n + G_{tip}, \tag{26}$$

where u_n^E is the end-opening; for instance in figure 5a $u_n^E \equiv u_n(x_1 = a_0)$. The fracture resistance, J_R, is monotonically increasing until the end opening, u_n^E, exceeds the critical opening u_n^* where the stresses vanish. Then, the bridging zone is fully developed and the steady state fracture resistance is attained $J_{ss} = \Gamma_0 + G_{tip}$, where $\Gamma_0 = \int_0^{u_n^*} \sigma_n du_n^E$ is the work of separation pr. unit area contributed from the bridging mechanism. Differentiating (26) the cohesive stresses can be found according to

$$\sigma(u_n) = \frac{dJ_R(u_n)}{du_n^E}. \tag{27}$$

This equation is used in section 4.4 for experimental determination of the bridging stress in a specimen.

In many composite materials G_{tip} is very small compared to Γ_0. From a modeling point of view this allows us to ignore G_{tip} or account for it by using a slightly modified cohesive law (Cox and Marshall, 1994), (Li et al., 2005). For instance, the cohesive law could initially have a higher peak stress $\hat{\sigma}^{tip}$ that is maintained over a small opening $u_n^{tip,*}$. When the opening exceeds

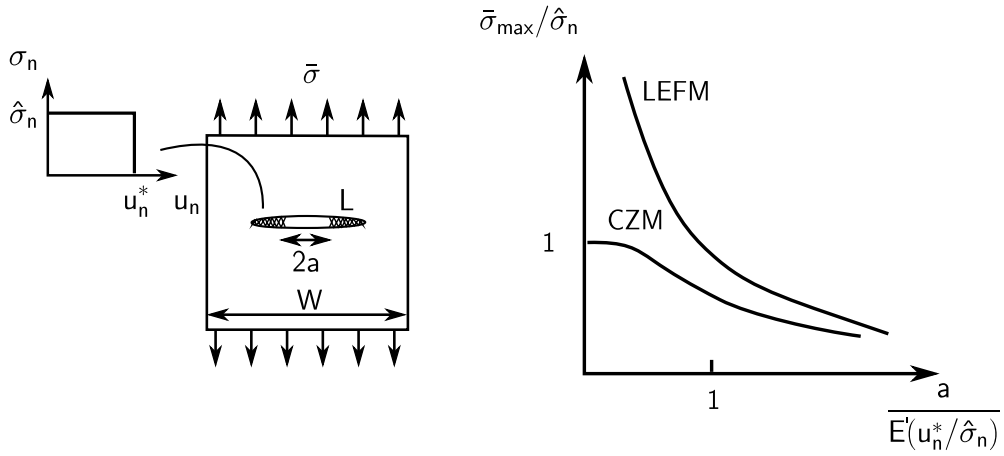

Figure 6: Strength of a plate with a flaw predicted by cohesive zone modeling and LEFM. From Bao and Suo (1992b).

$u_n^{tip,*}$ the stress from the bridging mechanism is attained, see figure 5c where the hatched rectangle represents the crack tip process.

Crack growth can be predicted by the criterion

$$J = J_R, \tag{28}$$

where J is the externally applied J integral. The criterion is valid irrespective of the length of the fracture process zone. i.e. it is also valid under LEFM.

3.2 Implications of large-scale-bridging

The deviation between a LEFM prediction and a CZM prediction is gradually increasing as the length of the fracture process zone becomes larger compared to relevant specimen lengths. This is illustrated by two examples:

Center flaw in a large plate

From (Bao and Suo, 1992b): Consider a plate of width W with an effective stiffness modulus E' and flaw of length $2a$, $a << W$, see figure 6. The plate is loaded along its edges by $\bar{\sigma}$. The plate fails by a fracture mechanism having the cohesive law shown in figure 6.

The predictions of maximum strength $\bar{\sigma}_{max}$ normalized with $\hat{\sigma}$ versus the crack length a normalized with a characteristic material length scale $u_n^* E'/\hat{\sigma}$ are shown in figure 6. The material length scale $u_n^* E'/\hat{\sigma}$ is closely related to the fully developed bridging zone length L (Bao and Suo, 1992b) (For the present example $L = \frac{\pi}{8} u_n^* E'/\hat{\sigma}$, (Bilby et al., 1963)). The results show that

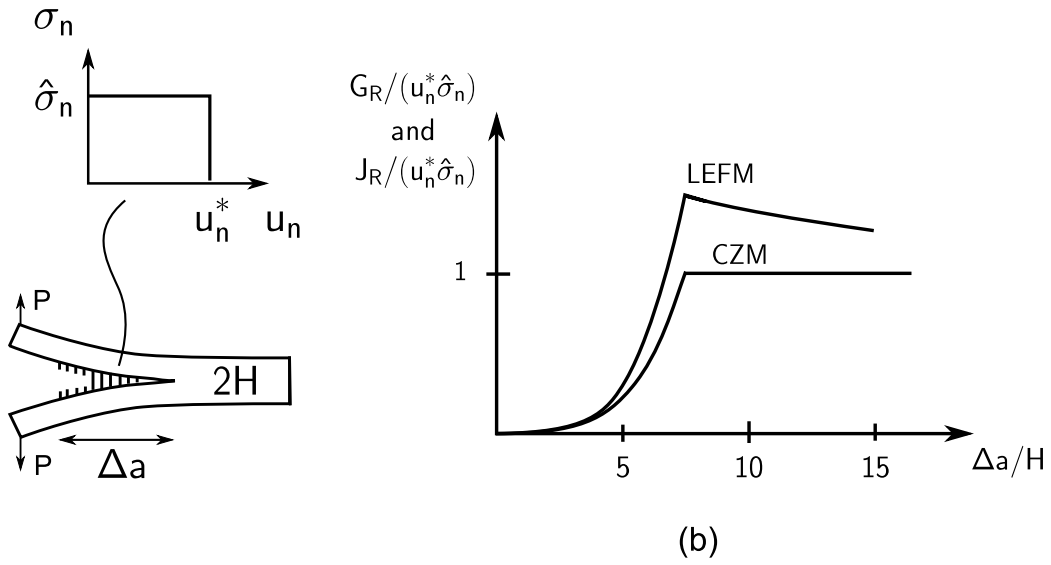

Figure 7: Strength of a DCB specimen. From (Sørensen and Jacobsen, 2000).

for $a/(u_n^* E'/\hat{\sigma})$ smaller than one, LEFM predicts the strength of the plate to exceed $\bar{\sigma}/\hat{\sigma} = 1$. This is physically unrealistic! Using a CZM approach the prediction for $a/(u_n^* E'/\hat{\sigma}) \to 0$ is $\bar{\sigma}/\hat{\sigma} \to 1$ i.e. when the plate is flawless the strength is $\hat{\sigma}$. This is a plausible prediction!

The deviation is acceptable when $a/(u_n^* E'/\hat{\sigma}) > 2$. Lets consider a plate that fails by fiber bridging. Parameters representable for fiber bridging are $u_n^* = 0.004m$ and $\hat{\sigma} = 1MPa$ (Sørensen and Jacobsen, 1998). The E-modulus of the plate is $E' = 40GPa$. Consequently, for LEFM to have an acceptable accuracy the crack length must fullfill $a > 320m$. Next, we consider cracking of a polymer foam material (Divinycell H130). The E-modulus is $E = 120MPa$. The cohesive law parameters are estimated by $\hat{\sigma} = \sigma^{uts} = 3MPa$ and $u_n^* = G_{Ic}/\hat{\sigma} = 300J/m^2/3MPa = 0.0001m$. Thus, for LEFM to give accurate results the crack length must fullfill $a \gtrsim 1cm$.

Double cantilever beam specimen

From (Sørensen and Jacobsen, 2000): A double-cantilever-beam is loaded by end-forces of magnitude P. The fracture process is a bridging mechanism with a response as that in figure 7. As parameters for the model is chosen: Initial crack length $a_0/H = 7.5$. Maximum cohesive stress $\hat{\sigma}_n/E = 1.92 \cdot 10^{-5}$. Critical separation $u_n^*/H = 0.122$.

In figure 7 the response of the specimen is computed using both LEFM

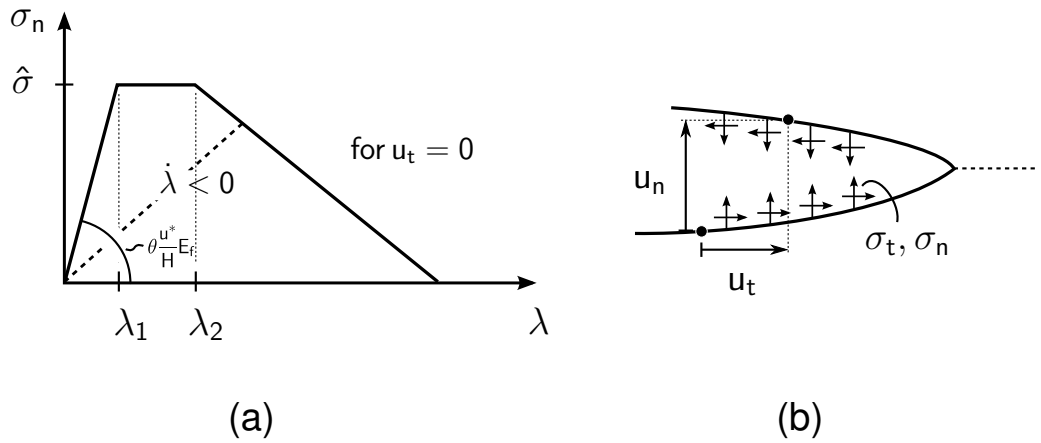

Figure 8: (a) The normal stress component, σ_n, under pure normal opening. (b) Definitions of the crack face openings.

and a CZM. On the vertical axis is the normalized energy release rate and on the horizontal axis is the normalized crack extension. The cohesive zone model predicts crack growth when $J = u_n^* \hat{\sigma}_n$, which is a correct prediction. On the contrary, LEFM predicts an over-shoot compared to the cohesive zone model. This is an effect of large-scale-bridging, since it is predicted that $L/H \approx 7$.

3.3 A cohesive law for finite element modeling

A widely used mixed mode cohesive law formulation was proposed by Tvergaard and Hutchinson (1993). The cohesive law specifies the dependence of the displacements u_t and u_n on the tractions σ_t^I and σ_n^I , see figure 8. Here, u_n and u_t are the normal and tangential components of the displacement difference across the interface, while σ_n^I and σ_t^I are the corresponding normal and shear stresses in the interface (See figure 8b). A measure of the opening of the interface is introduced. Let u_n^* and u_t^* be characteristic values of u_n and u_t and define a non-dimensional damage zone measure as:

$$\lambda = \sqrt{\left(\frac{u_n}{u_n^*}\right)^2 + \left(\frac{u_t}{u_t^*}\right)^2}, \; u_n \geq 0 \tag{29}$$

such that the tractions σ_n and σ_t drop to zero at $\lambda = 1$. The parameter defines a coupling between the tangential opening and the normal opening of the crack faces.

As λ is monotonically increasing the tractions in the interface are given by

$$\sigma_n^I = \frac{u_n/u_n^*}{\lambda}\sigma(\lambda) \quad \text{and } \sigma_t^I = \frac{u_t/u_t^*}{\lambda}\frac{u_n^*}{u_t^*}\sigma(\lambda), \tag{30}$$

where $\sigma(\lambda)$ denotes the interface normal stress under pure normal separation ($u_t \equiv 0$). $\sigma(\lambda)$ should be selected so it represents the mechanism taking place. Eq. 30 is derived from a potential and therefore the cohesive law is loading-history independent.

The studies included in the present work all applies a trapezoidal shape for $\sigma(\lambda)$. This starts at $\sigma = 0$ at $\lambda = 0$ and increases linearly to a peak value $\hat{\sigma}$ at $\lambda = \lambda_1$. This stress level is retained until $\lambda = \lambda_2$ where after it decreases linearly to zero. For $0 < \lambda < 1$ this can be written as:

$$\sigma(\lambda) = \begin{cases} \hat{\sigma}\frac{\lambda}{\lambda_1} & \text{for} \quad 0 < \lambda \leq \lambda_1 \\ \hat{\sigma} & \text{for} \quad \lambda_1 < \lambda \leq \lambda_2 \\ \hat{\sigma}\frac{\lambda-1}{\lambda_2-1} & \text{for} \quad \lambda_2 < \lambda < 1 \end{cases} \text{, for } \dot{\lambda} \geq 0 \text{ and } \lambda = \lambda_{max}, \tag{31}$$

where $\dot{\lambda} = \frac{\partial\lambda}{\partial u_n}\dot{u}_n + \frac{\partial\lambda}{\partial u_t}\dot{u}_t$ and $\dot{u}_n$ and $\dot{u}_t$ are the increments of u_n and u_t. λ_{max} is the highest λ attained through the loading history. $\lambda = \lambda(x_1)$ constitutes a measure of the state of the interface at x_1 : For $\lambda < \lambda_1$ the interface is undamaged. For $\lambda_1 \leq \lambda < 1$ the interface is damaged and for $\lambda \geq 1$ the interface has fractured.

It is seen that the cohesive law initially has a finite stiffness. Therefore deformations appear in the interface before the damage stress $\hat{\sigma}$ is reached which should not be the case. However, the effect of the initial deformation is typically small when the slope of the initial part ($\lambda < \lambda_1$) is kept sufficiently high. But, if the slope becomes too large numerical problems can be encountered. Consequently, for a given problem, convergence studies should be carried out to determine an acceptable slope of the initial part.

The work of separation per unit area of interface (fracture toughness), Γ, is given by

$$\Gamma = \frac{1}{2}\hat{\sigma}u_n^*[1 - \lambda_1 + \lambda_2], \tag{32}$$

which can be found by integrating the cohesive stresses σ_n^I and σ_t^I over the crack opening components $u_n^*$and u_t^*. For this particular cohesive law, Γ, is thus independent of the mode of the opening.

Unloading

In order to account for non-monotonic openings, a linear unloading (see figure 8a) is used to represent the partly damaged interface:

$$\sigma_n^I = \frac{u_n}{u_n^*}\frac{\sigma(\lambda_{max})}{\lambda_{max}} \quad \text{and } \sigma_t^I = \frac{u_t}{u_t^*}\frac{u_n^*}{u_t^*}\frac{\sigma(\lambda_{max})}{\lambda_{max}}, \; \lambda < \lambda_{max} \text{ or } \dot{\lambda} < 0 \tag{33}$$

Resisting material interpenetration

To resist material interpenetration (zones along the interface where $u_n < 0$) we can modify the cohesive law so negative cohesive stress arise for increasing interpenetration. The stresses are still calculated according to (30)-(33), but with the change that (30a) and (33a) become replaced by:

$$\sigma_n^I = k_n u_n, \; u_n < 0, \tag{34}$$

where k_n is a stiffness constant.

The shear stresses are still given by (30) but with the dimensionless opening parameter defined as

$$\lambda = |u_t/u_t^*| \, , \; u_n < 0. \tag{35}$$

In [P3] we use

$$k_n = \frac{\hat{\sigma}_n}{\lambda_1 u_n^*}. \tag{36}$$

Note that the cohesive law is formulated such that the interface can fracture even if $u_n < 0$.

3.4 Numerical aspects of cohesive zones in finite element modeling

The crack growth problems in paper [P3] and [P4] are solved using a cohesive zone model integrated with an implicit, finite-strain finite-element-formulation that is solved incrementally. The numerical solution can be difficult and numerical instability are easily encountered when using conventional solution methods. Therefore, the cohesive zone problems in the present thesis are solved using a special Rayleigh-Ritz finite element method (RR-FEM)

The Rayleigh-Ritz finite element method

The incremental displacements $\dot{v}_n$ of the N finite element degrees of freedom (DOF) are in the case of prescribed displacements obtained by solving the finite element equation

$$\sum_{n=1}^{N} A_{mn}\dot{v}_n = C_n, \quad m = 1, 2...N, \tag{37}$$

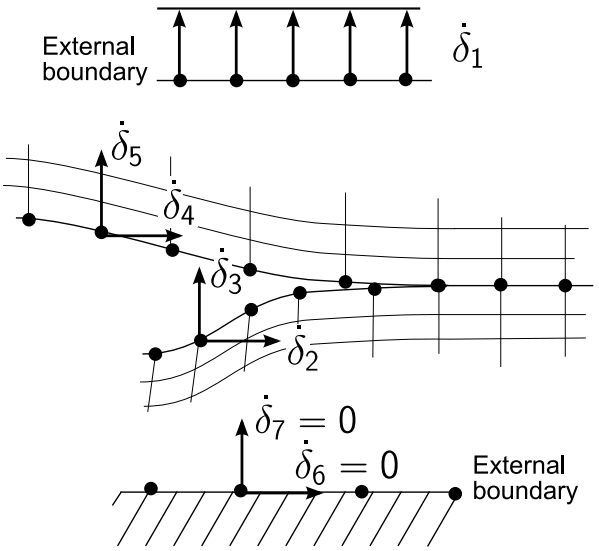

Figure 9: Nodes on the crack faces are prescriped to obtain stable solutions.

where, A_{mn} is the global stiffness matrix and C_m is the equilibrium correction vector.

A small number $r-1$ of the total N finite element DOF with incremental displacements $\dot{v}_n$ are chosen to make up a reduced system of DOF. The $r-1$ DOF are referred to as Rayleigh-Ritz-DOF and they have displacements denoted $\dot{\delta}_1, \dot{\delta}_2 ... \dot{\delta}_{r-1}$. The finite element method is now used for determining r trial functions V_{nl}. Such that $V_{n1} = \dot{v}_n$ is a solution to (37) with $\dot{\delta}_1 = 1$ and all other $\dot{\delta}_j = 0$; $V_{n2} = \dot{v}_k$ is a finite element solution with $\dot{\delta}_2 = 1$ and all other $\dot{\delta}_j = 0$; etc. The trial function V_{nl} for $l = r$ is computed by solving for $\dot{\delta}_1$, $\dot{\delta}_2 ... \dot{\delta}_{r-1} = 0$ while applying the equilibrium correction calculated from the previous increment.

A solution to the RR-FEM system in terms of $\dot{\delta}_j$ can then be obtained by solving the equation system (Tvergaard, 1976):

$$\sum_{j=1}^{r} a_{ij}\dot{\delta}_j = c_i, \quad i = 1, 2, ...N, \tag{38}$$

where

$$a_{ij} = \sum_{(m,n)=1}^{N} A_{mn}V_{mi}V_{nj}$$

and

$$c_i = \sum_{n=1}^{N} C_n V_{ni}.$$

In equation 38 boundary conditions are inserted and when the equation is solved a solution vector $\dot{\delta}_i$ results. The components of this vector are the magnitudes of the trial functions and the solution in terms of the finite element DOF is obtained from

$$\dot{v}_n = \sum_{l=1}^{r} V_{nl}\dot{\delta}_l, \quad n = 1, 2.....N \tag{39}$$

Application of the RR-FEM method for solving crack growth problems

In equation 38 the finite element problem has been reformulated so it consists of a reduced number of RR-DOF. In crack growth problems situations are often encountered where the deformations are much larger around the crack tip than at the external boundary where the displacements are prescribed. Such a situation often results in a numerical unstable solution where equilibrium is not maintained.

With the RR-FEM method crack openings can be prescribed. This we will illustrate with an example. In figure 9 seven RR-DOF are defined. $\dot{\delta}_1$ denotes the prescribed displacement at the exterior boundary of the body. $\dot{\delta}_{i=2..5}$ denote incremental displacements of nodes near the crack tip. $\dot{\delta}_6$ and $\dot{\delta}_7$ denote the displacements at the boundary (that is clamped). The DOF $i = 2..5$ are rewritten into crack-opening RR-DOF in the x_1 and x_2 direction, respectively:

$$\dot{\Delta}_1 = \dot{\delta}_4 - \dot{\delta}_2 \text{ and } \dot{\Delta}_2 = \dot{\delta}_5 - \dot{\delta}_3.$$

A new vector $\dot{\delta}^*$ including the crack opening DOF is defined as

$$\dot{\delta}^* = \{\dot{\delta}_1,\ \dot{\Delta}_1,\ \dot{\Delta}_2,\ \dot{\delta}_4,\ \dot{\delta}_5,\ \dot{\delta}_6,\ \dot{\delta}_7\}$$

in terms of this vector the solution can be written as

$$\sum_{j=1}^{5} a^*_{ij}\dot{\delta}^*_j = c_i, \quad i = 1,\ 2, ...6, \tag{40}$$

where a^*_{ij} is a manipulated version of a_{ij}

$$a^*_{ij} = \{a_{i1},\ a_{i2},\ a_{i3},\ (a_{i4} + a_{i2}),\ (a_{i5} + a_{i3}),\ a_{i6},\ a_{i7}\}.$$

Lets consider a case where crack openings are large compared to the outer displacements i.e. $\dot{\delta}_1 << \dot{\Delta}_1$. Then, a stable solution may require that $\dot{\Delta}_1$ is prescribed. To get a more compact notation we ignore $\dot{\Delta}_2$, $\dot{\delta}_5$ and δ_7 since

these are included according to the same principle. Equation 40 is written as

$$\left\{\begin{array}{c} a_{11} \\ a_{21} \\ a_{41} \\ a_{61} \end{array}\right\}\dot{\delta}_1 + \left\{\begin{array}{c} a_{12} \\ a_{22} \\ a_{42} \\ a_{62} \end{array}\right\}\dot{\Delta}_1 + \left\{\begin{array}{c} a_{14}+a_{12} \\ a_{24}+a_{22} \\ a_{44}+a_{42} \\ a_{64}+a_{62} \end{array}\right\}\dot{\delta}_4 + \left\{\begin{array}{c} a_{16} \\ a_{26} \\ a_{46} \\ a_{66} \end{array}\right\}\dot{\delta}_6 = \left\{\begin{array}{c} c_1 \\ c_2 \\ c_4 \\ c_6 \end{array}\right\}.$$

The boundary condition $\dot{\delta}_6 = 0$ is applied

$$\left\{\begin{array}{c} a_{11} \\ a_{21} \\ a_{41} \\ 0 \end{array}\right\}\dot{\delta}_1 + \left\{\begin{array}{c} a_{12} \\ a_{22} \\ a_{42} \\ 0 \end{array}\right\}\dot{\Delta}_1 + \left\{\begin{array}{c} a_{14}+a_{12} \\ a_{24}+a_{22} \\ a_{44}+a_{42} \\ 0 \end{array}\right\}\dot{\delta}_4 + \left\{\begin{array}{c} 0 \\ 0 \\ 0 \\ 1 \end{array}\right\}\dot{\delta}_6 = \left\{\begin{array}{c} c_1 \\ c_2 \\ c_4 \\ 0 \end{array}\right\}.$$

The external loading $\dot{\delta}_1$ is defined and set equal to $\dot{\delta}_0$:

$$\left\{\begin{array}{c} 1 \\ a_{21} \\ a_{41} \\ 0 \end{array}\right\}\dot{\delta}_1 + \left\{\begin{array}{c} 0 \\ a_{22} \\ a_{42} \\ 0 \end{array}\right\}\dot{\Delta}_1 + \left\{\begin{array}{c} 0 \\ a_{24}+a_{22} \\ a_{44}+a_{42} \\ 0 \end{array}\right\}\dot{\delta}_4 + \left\{\begin{array}{c} 0 \\ 0 \\ 0 \\ 1 \end{array}\right\}\dot{\delta}_6 = \left\{\begin{array}{c} 0 \\ c_2 \\ c_4 \\ 0 \end{array}\right\} + \left\{\begin{array}{c} 1 \\ 0 \\ 0 \\ 0 \end{array}\right\}\dot{\delta}_0.$$

The crack opening in the x_1 direction $\dot{\Delta}_1$ is prescribed by Δ_0:

$$\left\{\begin{array}{c} 1 \\ a_{21} \\ a_{41} \\ 0 \end{array}\right\}\dot{\delta}_1 + \left\{\begin{array}{c} 1 \\ 0 \\ 0 \\ 0 \end{array}\right\}(-\dot{\delta}_0) + \left\{\begin{array}{c} 0 \\ a_{24}+a_{22} \\ a_{44}+a_{42} \\ 0 \end{array}\right\}\dot{\delta}_4 + \left\{\begin{array}{c} 0 \\ 0 \\ 0 \\ 1 \end{array}\right\}\dot{\delta}_6 = \left\{\begin{array}{c} 0 \\ c_2 \\ c_4 \\ 0 \end{array}\right\} - \left\{\begin{array}{c} 0 \\ a_{22} \\ a_{42} \\ 0 \end{array}\right\}\Delta_0. \tag{41}$$

This equation is solved to obtain $\dot{\delta}_1$, $\dot{\delta}_0$, $\dot{\delta}_4$, $\dot{\delta}_6$. Solving the full RR-FEM equation that also includes $\dot{\Delta}_2$, $\dot{\delta}_5$ and $\dot{\delta}_7$ the solution vector to (41) will instead contain

$$\dot{\delta}_1,\ \dot{\delta}_0,\ \dot{\Delta}_2,\ \dot{\delta}_4,\ \dot{\delta}_5,\ \dot{\delta}_6,\ \dot{\delta}_7.$$

By using the boundary conditions $\dot{\delta}_6 = 0$, $\dot{\delta}_7 = 0$ and $\dot{\Delta}_1 = \Delta_0$ all the components of the solution $\dot{\delta}^* = \{\dot{\delta}_1,\ \dot{\Delta}_1,\ \dot{\Delta}_2,\ \dot{\delta}_4,\ \dot{\delta}_5,\ \dot{\delta}_6,\ \dot{\delta}_7\}$ are known:

$$\dot{\delta}^* = \{\dot{\delta}_1,\ \Delta_0,\ \dot{\Delta}_2,\ \dot{\delta}_4,\ \dot{\delta}_5,\ 0,\ 0\}.$$

Finally, the FEM DOFs are then obtained using (39) together with

$$\dot{\delta} = \{\dot{\delta}_1,\ (\dot{\delta}_4 - \Delta_0),\ (\dot{\delta}_5 - \dot{\Delta}_2),\ \dot{\delta}_4,\ \dot{\delta}_5,\ 0,\ 0\}.$$

Selecting the RR-DOF that ensures numerical stability

The difficult part of obtaining a numerically stable solution is to determine where, when and how much to prescribe crack openings. The procedure that was applied in the present studies is the following:

Where:

- The crack-opening RR-DOF is chosen amongst node pairs for which $\lambda_1 < \lambda < 1$. If none such exists it is chosen arbitrarily.
- The actual node pair chosen as crack-opening RR-DOF is that with largest $\dot{\lambda}$.
- If $|\dot{u}_t| > |\dot{u}_n|$ for the chosen node pair, then the tangential opening is prescribed. If $\dot{u}_t| \leq |\dot{u}_n|$ the normal opening is prescribed.

When:

When is the external boundary $\dot{\delta}_1$prescribed and when are the crack openings prescribed?

If $\dot{\delta}_1/10 > \dot{\Delta}_1$ and $\dot{\delta}_1/10 > \dot{\Delta}_2$ the external boundary (δ_1) is prescribed. Otherwise, the largest of $\dot{\Delta}_1$and $\dot{\Delta}_2$ is prescribed.

How much:

The size of the increments is controlled by a criterion that ensures the incremental crack opening is small:

$$\dot{\lambda} < \lambda_1/10 \text{ and } \dot{\lambda} < 0.01,$$

for points along the interface where $\lambda < 1$. $\dot{\lambda}$ is the increase of the crack opening parameter, λ_1 is the λ value where the initial slope of the cohesive law changes, cf. 31. The step-size is reduced if this criterion is violated while incrementing through the solution.

4 Summary of results

In paper [P1] and [P2] LEFM is applied to face sheet / core debonding of sandwich structures. [P1] contains a theoretical analysis of a fracture specimen and [P2] concerns experimental measurement of fracture toughness for face sheet / core debonding. Results from these papers will be presented first. Next, main results from [P3] are given. [P3] concerns collapse of a sandwich column with emphasis on the interaction of face sheet/core fracture and buckling modes. Finally, results from [P4] that establishes a micro mechanical model of the cross-over fiber bridging is presented. The study in [P4] relates to the previous studies in the sense that the cross-over fiber bridging is a potential fracture mechanism for face sheet / core debonding in some sandwich structures with fiber reinforced (FRP) face sheets. This relation is illustrated in figure 2. However, in [P4] the study is not specifically aimed at sandwich structures since cross-over fiber bridging is relevant to other classes of fibrous composite materials too.

4.1 Face sheet / core debonding of sandwich structures

4.1.1 Introduction

For sandwich structures, debond imperfections (areas between the face sheet and core with no adhesion) comprise an important damage type that can lead to debonding crack growth i.e. crack growth in the interface between face sheet and core. Interface cracking is generally mixed mode cracking (Williams, 1959; Rice, 1988) and experiments have shown that the fracture toughness of interfaces can depend on the mode mixity (Cao and Evans, 1989), (Wang and Suo, 1990), (Liechti and Chai, 1992). A complete LEFM analysis of a sandwich specimen should therefore include the determination of both the energy release rate and the mode mixity. Such an analysis is carried out in [P1].

The paper analyses a unit width sandwich specimen of length L with a crack of length a starting at $x_1 = -a$, $x_2 = 0$ (See figure 10). The face sheets have equal heights H and the core has height h. The sandwich specimen is loaded along its ends by moments pr. unit width M_k, $k = 1..3$ and by forces pr. unit width P_k, $k = 1..3$. For the first part of the analysis it is required that $\frac{a}{H} >> 1$ and $\frac{L}{2H+h} >> 1$ so that the crack tip is remote from the ends. Then, the energy release rate and mode mixity attain steady state values i.e. the values does not change with a and $L - a$.

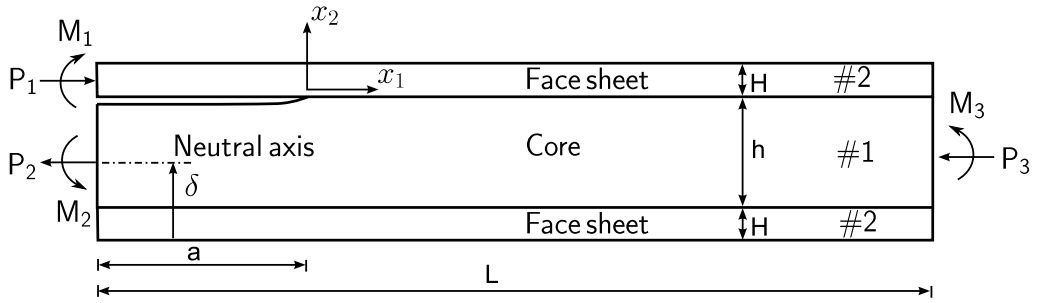

Figure 10: Interface cracking of a sandwich specimen with equal thickness face sheets is analyzed in [P1].

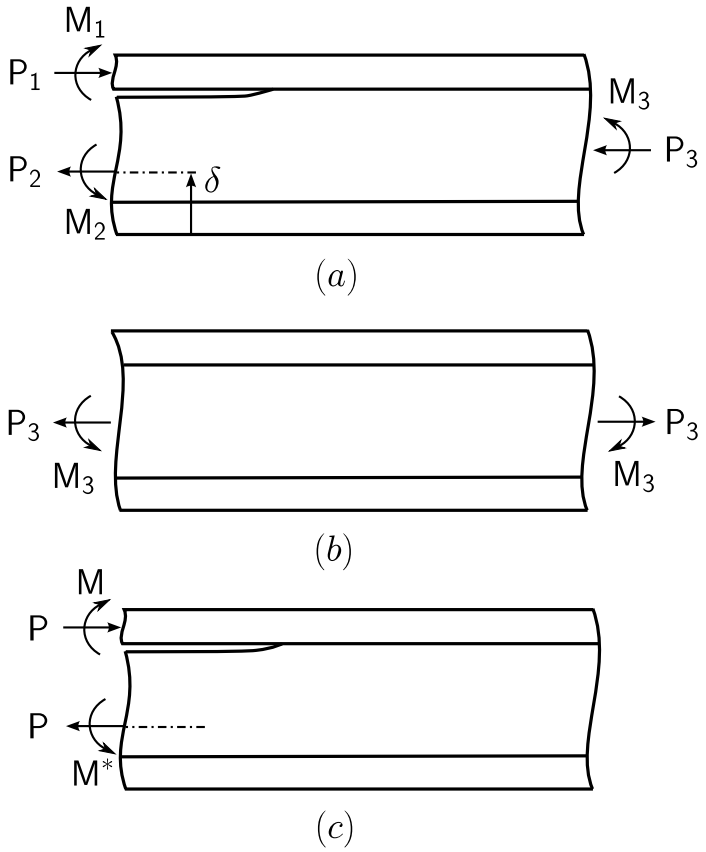

Figure 11: By superimposing the stress field (b) on the stress field of the original problem (a) the stress field of a reduced problem (c) is obtained, where $M^* = Ph\chi + M$ and χ is given in the appendix of [P1].

4.1.2 Analysis

The analysis in [P1] is based on classical beam theory and LEFM for interfaces (reviewed in section 2.1). Through two steps, the general load situation in figure 10 is transformed to a reduced problem: First, by static moment and force equilibrium requirements, it is clear that two of the six loads are statically determined. Next, the stress field from an intact sandwich specimen loaded by moments and forces, as shown in figure 11b, is superimposed on situation 11a whereby M_3 and P_3 cancel out. The stress field for the problem in figure 11b only contains stress components parallel to the crack. Therefore, superimposing this stress field on that of problem 11a does not alter the singular (σ_{12} and σ_{22}) stresses at the crack tip. Using these two steps it is shown that, the stress singularity at the crack tip only depends on the reduced load parameters P and M. These are given by

$$P = -P_1 + C_1 P_3 + C_2 M_3/h$$

$$M = -M_1 + C_3 M_3, \tag{42}$$

where C_1,C_2 and C_3 are dimensionless constants given in the appendix of [P1].

For the next part of the analysis, the sandwich specimen is loaded only with the reduced loads M and P (However, as accounted for above these represent any combination of the original loads). From (6) it is realized that K must have the SI units $Pa\,m^{1/2-i\epsilon}$ (see discussion in section 2.1) and since the analysis is based on LEFM, K can be written as a linear combination of P/H and M/H^2 according to

$$K = K_1 + iK_2 = \left[\frac{P}{H} z_1 + \frac{M}{H^2} z_2\right] H^{1/2-i\epsilon}, \tag{43}$$

where z_1 and z_2 are complex numbers. By combining (43) with (10) and an analytical calculation of G the complex numbers z_1 and z_2 can be calculated analytically apart from a phase shift angle ω that has to be determined by analytical means. Then, according (10) the energy release rate can be cast in the following form

$$G = \frac{c_2}{16}\left(\frac{P^2}{hU} + \frac{M^2}{h^3 V} + 2\frac{PM}{\sqrt{UV}h^2}\sin\gamma\right), \tag{44}$$

where U, V and γ are non-dimensional constants that depend on α (or Σ) and $\eta = h/H$, the constants are given in the appendix of [P1]. In the case of plain strain the factor $c_2/16 = \bar{E}_2/2$.

By using (43) and the solutions to z_1 and z_2 together with (12) the mode mixity can be expressed as

$$\psi = \arctan\left[\frac{\lambda\sin\omega - \cos(\omega+\gamma)}{\lambda\cos\omega + \sin(\omega+\gamma)}\right], \tag{45}$$

where

$$\lambda = \sqrt{\frac{V}{U}}\frac{Ph}{M}$$

for $M \neq 0$ and

$$\psi = \omega$$

for $M = 0$.

In the derivation of (45) $\ell = h$ was used (cf. eq. 12). The energy release rate for the specimen is computed purely analytical but the mode mixity contains the phase angle ω that yet remains to be determined. This phase angle is independent of P and M. The following describes a numerical approach proposed in [P1] for determining ω.

The complex stress intensity factor, K, is related to the crack face displacement components, Δu_1 and Δu_2, via (8). Rewriting (8) to modulus-argument form we get

$$\Delta u_1 + i\Delta u_2 = |\Delta u|e^{i\phi} = \frac{c_1+c_2}{2\sqrt{2\pi}\sqrt{1+4\epsilon^2}\cosh\pi\epsilon}Kr^{i\epsilon+1/2}e^{-i\varphi}, \tag{46}$$

where $\varphi = \arctan 2\epsilon$, $|\Delta u| = \sqrt{\Delta u_1^2 + \Delta u_2^2}$ and $\phi = \arctan\frac{\Delta u_1}{\Delta u_2}$. The equation is multiplied with $\ell^{i\epsilon}$ and it is used that $K\ell^{i\epsilon} = |K\ell^{i\epsilon}|e^{\psi}$. Thereby all the complex numbers can be written in the modulus-argument form giving an equation for which the arguments must be equal on each side of the equality sign:

$$\psi^* = \phi - \epsilon\ln(r/\ell) + \arctan 2\epsilon, \tag{47}$$

the * only indicates that ψ^* is determined from the crack face displacements.

By combining (46) with (10) it is found that the energy release rate is related to the crack face displacements via

$$G^* = \frac{\Delta u_2^2 + \Delta u_1^2}{r}\frac{(\frac{1}{2}+2\epsilon^2)\pi}{c_1+c_2}. \tag{48}$$

The crack face displacement components (Δu_1 and Δu_2) are found from a finite element solution. When calculating G^* and ψ^* it turns out that these are not independent of r. To remove this variation with r the mode mixity was found by extrapolating crack opening components in vicinity of the crack

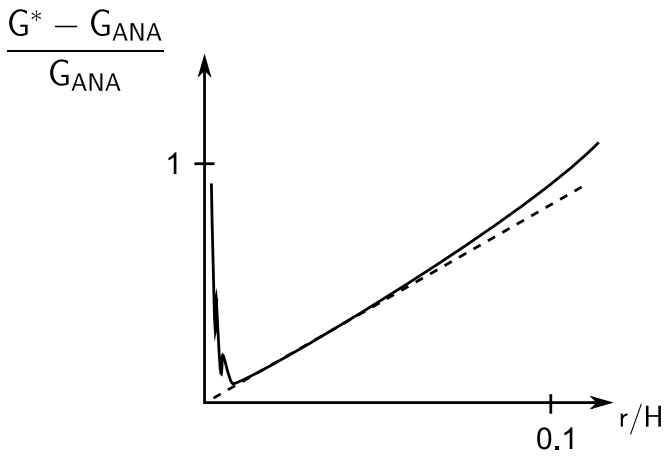

Figure 12: Example of G determined from the nodal displacements of a finite element solution.

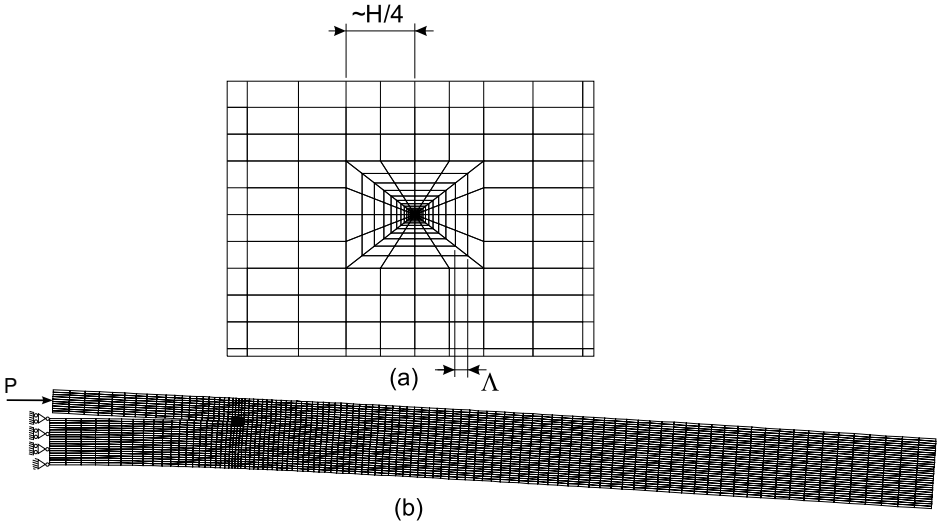

Figure 13: Mesh and loading used in the analysis for determining ω.

tip to $r = 0$ i.e. $\psi_{NUM} = \psi^*(r \to 0)$ and $G_{NUM} = G^*(r \to 0)$. In figure 12 the relative deviation between the analytical G (eq. 44) and G^* calculated from the crack opening components (eq. 48) is plotted against the normalized distance from the crack tip. For all computations in [P1] the accuracy of the method was checked; the deviation between the exact G calculated from (44) and G_{NUM} was less that 0.5% for all computations. Figure 13 shows a mesh used in the calculations.

The phase angle ω is obtained from a load case with $M = 0$ and $P \neq 0$ since then $\omega = \psi$ (cf. equation 45), see figure 13.

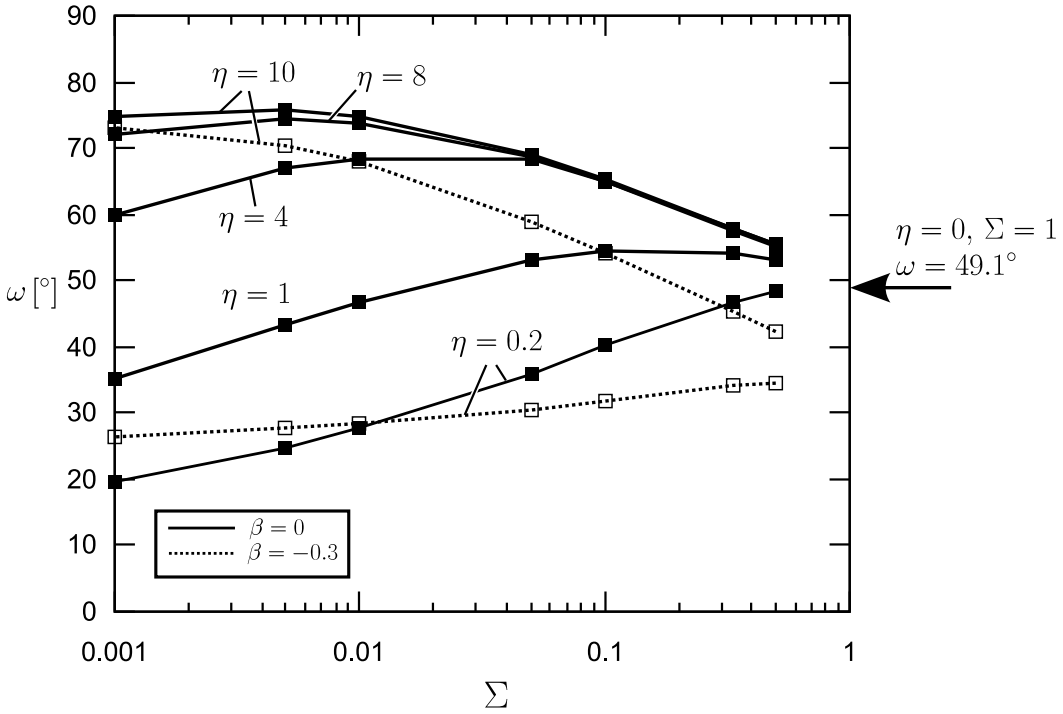

Figure 14: The load independent phase angle ω as function of the elastic mismatch parameter Σ for a number of different thickness ratios. The arrow indicate the value corresponding to a symmetric, homogeneous DCB specimen loaded by an axial force.

4.1.3 Results

The phase angle ω was determined for a wide range of sandwich specimens with elastic mismatch and finite core thicknesses: Sandwich specimens with up to 1000 times stiffer face sheet than core and face sheet/core thickness ratio (h/H) in the range 0.2 to 10. The solutions can be found in paper [P1]. In figure 14 some selected results are shown. The curves show that ω increases for increasing core thickness (and the larger the elastic mismatch, the stronger this trend becomes). A point not discussed in [P1] is that this variation with core thickness can be used for designing a mixed mode fracture test: Let us assume we have a test setup that can impose a pure normal force P, like the load situation in 13. Then, different mode mixities can be obtained by making specimens with different core thicknesses; since $\psi = \omega$ for $M = 0$. As an example, consider a specimen consisting of glass fiber face sheets and polymer foam core. Then $\Sigma \approx 0.005$. In that case the results in figure 14 show that the mode mixity can be changed from $\psi \approx 22^\circ$ to $\psi \approx 77^\circ$

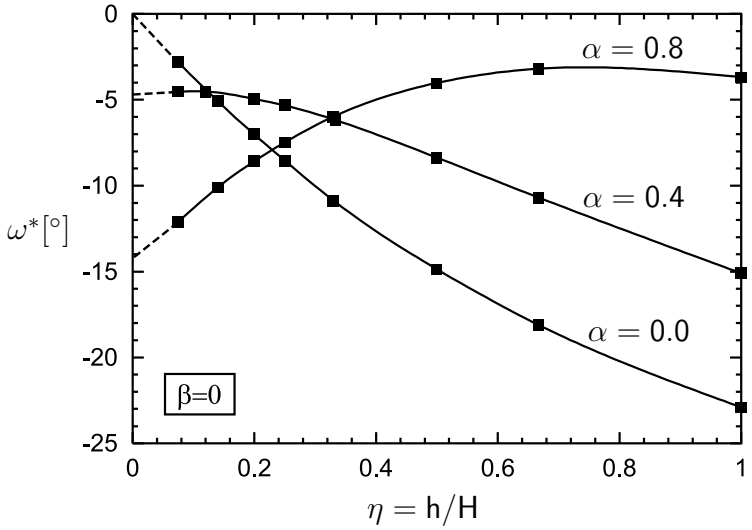

Figure 15: The phase angel $\omega* = \omega + \gamma - 90°$ determined for sandwich specimens with thin core. The dashed line shows the extrapolation to $\eta = 0$.

simply by changing the thickness of the core. It is worth noting that the test specimen will promote stable crack growth since it is a steady state specimen. This test method has not been used in the Ph.D. work. In [P1] another test method was proposed for measuring interface fracture toughness of sandwich structures under mixed mode conditions. That test method is used in [P2].

Next, ω is determined for sandwich specimens having an infinite thin core (representing e.g. a thin layer of glue). A similar study already exists, but for a more narrow selection of elastic mismatch-values (Suo and Hutchinson, 1989). The earlier study was based on solving integral equations, whereas the present makes use of a much simpler method. The present solution method uses linear extrapolation of two solutions with relatively thin cores $\eta = h/H = 0.15$ and $\eta = 0.1$ to $\eta = 0$. In figure 15, the dashed lines represent the extrapolations for some sandwich configurations with solutions determined by (Suo and Hutchinson, 1989). Our solutions match the solutions by S&H with a accuracy better that 0.5°. More results for material combinations with large elastic mismatch are given in [P1].

The analytical expression for the energy release rate (44) is derived by evaluating the J-integral along the exterior boundaries of the specimen using the stress fields found from classical beam theory. However, this distribution of the stresses is only true when the stress field from the crack tip is far from the ends of the specimen. If the specimen gets too short, the crack tip stress field reaches the ends along which the J-integral is evaluated. Figure 16

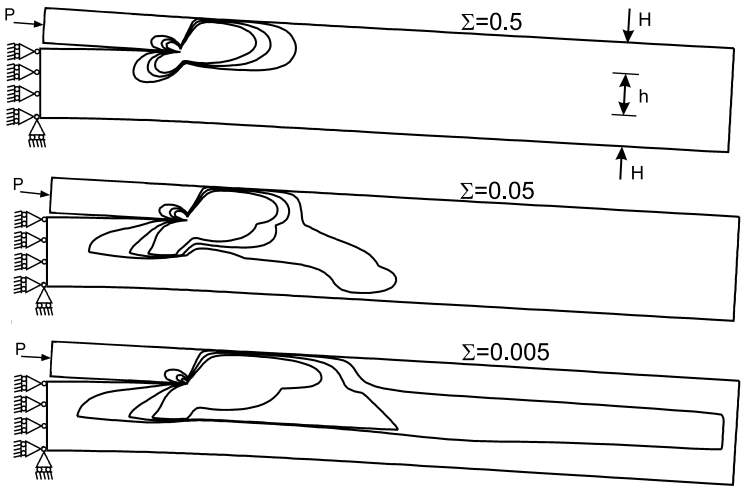

Figure 16: The shear stress contours $\sigma_{12}H/P = 0.1,\ 0.05,\ 0.01$ for a sandwich specimen with $\eta = 1$, $\beta = -0.2$ and $\Sigma = 0.5,\ 0,05$ and 0.005, respectively.

shows how the material parameter Σ affects the crack tip stress field. From the figure it is clear that, as the elastic mismatch between core and face sheet becomes larger, the stress field elongates, in particular towards the uncracked end of the specimen.

When choosing the dimensions for a test specimen, it therefore crucial to ensure that the specimen is long enough for the ends of the sandwich specimen to be unaffected by the stresses from the crack tip. For that purpose it is analyzed when the analytical energy release rate denoted G_{ANA} (eq. 44) will deviate from the true energy release rate G_{true}. G_{true} is estimated with the CSDE method. An error measure is defined as $\xi = \left|\frac{G_{\mathrm{ANA}} - G_{\mathrm{true}}}{G_{\mathrm{true}}}\right|$. A complexity in determining ξ is that the combination of M and P that gives the largest error ξ must be determined. Details on the procedure for doing this are found in the appendix of paper [P1]. Figure 17 shows curves for the length $(L-a)/H$ that gives an error of 5% in a specimen with $h/H = 1$. It is seen that for moderate elastic mismatch ($\Sigma \approx 0.01$) the specimen must have a length approximately 10 times the face sheet thickness.

4.2 Measurement of fracture toughness for face sheet / core debonding of sandwich structures

In [P2] debonding fracture toughness as function of mode mixity is determined experimentally. The paper also includes in-depth discussions of the observed fracture mechanisms.

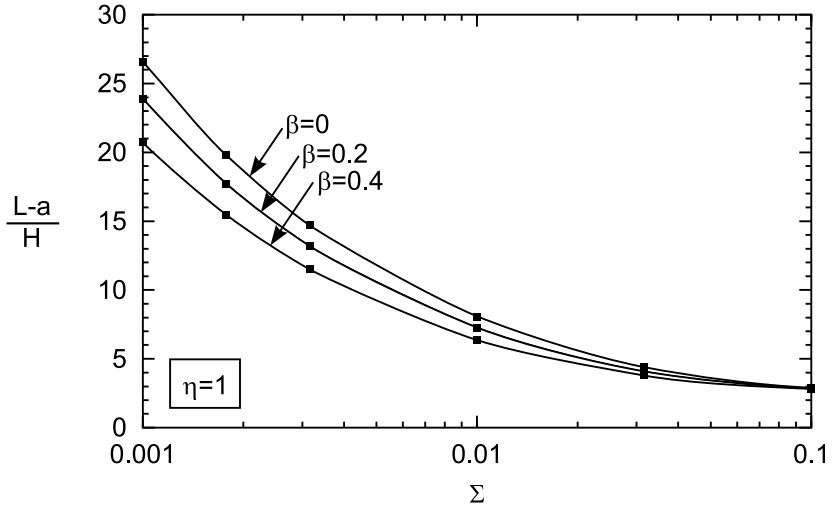

Figure 17: The curves shows lengths of the intact part of the sandwich specimen normalized with the face sheet thickness that gives 5% error in the energy release rate calculated by (44).

4.2.1 Materials and background

In [P2], debonding fracture toughness of two types of sandwich structure is measured experimentally. The sandwich structures are commercially manufactured and have plain weave glass fiber reinforced polyester face sheets. The interface between face sheet and core contains a layer of chopped strand mat (CSM). The CSM layer is randomly oriented fibers bundles and is used in sandwich structures to improve the adhesion. The elastic properties of the face sheet material have been measured through a comprehensive range of material tests (Toftegaard and Goutianos, 2007). The measured elasticity constants are: $E_{11} = 14.9GPa$, $E_{22} = 7.53GPa$, $E_{33} = 16.5GPa$, $\nu_{13} = 0.2$, $\nu_{12} = 0.199$, $\nu_{32} = 0.16$ and $G_{12} = 2.2GPa$. Here, E, v and G denote the Young's modulus, the Poisson's ratio and the shear modulus, respectively; the subscripts refer to the material direction defined in the coordinate system in figure 10. Note that G_{12} is the out-of-the-plane shear modulus. The thickness of the sandwich face sheets are $6mm$. The cores consist of Polyvinyl chloride (PVC) foam Divinycel H80 and H130, respectively. The elastic constants for the core materials are taken from (Zenkert, 1995): For the H80 PVC foam $E = 85MPa$, $\nu = 0.3$ and for H130 $E = 175MPa$, $\nu = 0.3$. The thickness of the cores is $40.0mm$.

Paper [P2] uses LEFM for interfaces between orthotropic media (see section 2.2) for determining the stress situation at the crack tip. The energy release rate for the sandwich structure is calculated by evaluating the J inte-

gral along the exterior boundaries of the sandwich structure. The sandwich specimen is loaded by end moments [Nm] and end normal-forces [N] and the width of the specimen is B, see figure 10. The solution to the J integral is:

$$G = \frac{(s'_{11})_{\#2}}{2B^2}\left(\frac{P^2}{hU} + \frac{M^2}{h^3V} + \frac{PM}{\sqrt{UV}h^2}\sin\gamma\right), \tag{49}$$

where $(s'_{11})_{\#2}$ is the compliance parameter s'_{11} for the face sheet material. The constants U, V and γ are given in the appendix of [P2] (they differ slightly from γ, U and V in eq. 44 for an isotropic sandwich specimen). P and M are the reduced loads from (42) but calculated with the $C's$ provided in the appendix of [P2]. Equation (44) and (49) converge for isotropic materials.

The derivation of the expression for the mode mixity in [P2] follows the same steps as in [P1]. The results show that the mode mixity also can be calculated from equation (45) but with U and V taken from the appendix of [P2]. The phase angle ω is determined using the CSDE method described in the previous section and equation (47): $\psi^* = \phi - \epsilon\ln(r/l) + \arctan 2\epsilon$ is also valid here. However, the oscillatory parameter ϵ (see equation 4) must be calculated using β defined in equation (18); a generalization of the Dundurs parameter for orthotropic materials. The values of ω are found from the CSDE method:

Configuration	ω
GFRP/H80	60.2°
GFRP/H130	66.0°

The characteristic length parameter was selected as $\ell = h = 40mm$. The choice of ℓ must follow the results since ℓ must be known when using the results elsewhere.

4.2.2 Experimental setup

The face sheet/core interface fracture toughness is measured using an experimental setup that can apply bending moments to the DCB specimen. The test setup is shown in figure 18. The double cantilever beam sandwich specimen is loaded by uneven moments via two arms. The arms are loaded through a wire/roller system that is connected to a special loading device. The force, F, is the same all along the wire (apart from the neglectable resistance from the rollers) and, thus, the moments are calculated by $M_1 = (+/-)F\ell_1$ and $M_2 = (+/-)F\ell_2$. The signs of the moments are changed by rearranging the wire as shown in figure 18(a1) to 18(a2). The magnitudes of the moments relative to each other are changed by changing the arm lengths ℓ_1 and ℓ_2. The

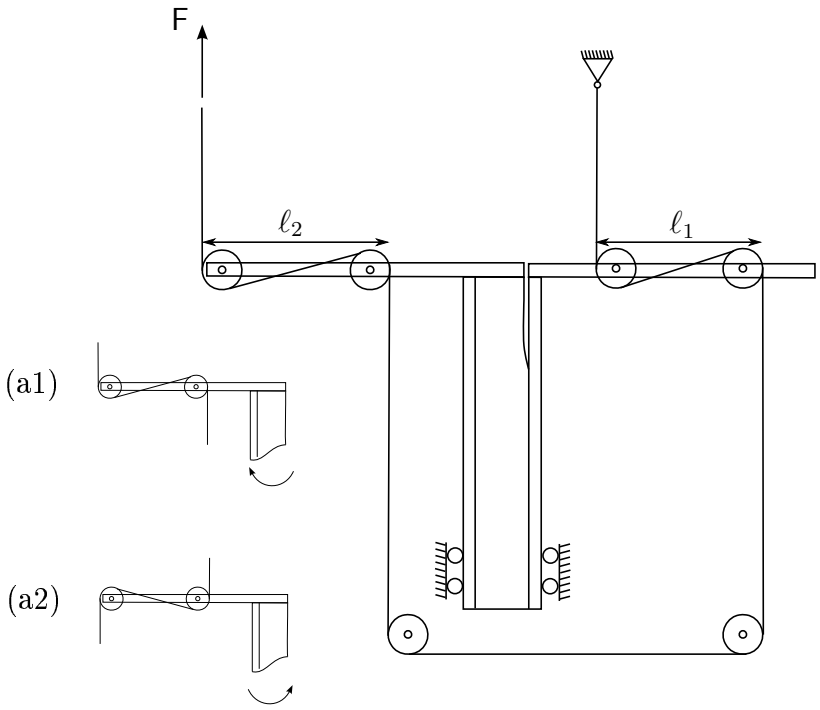

(a)

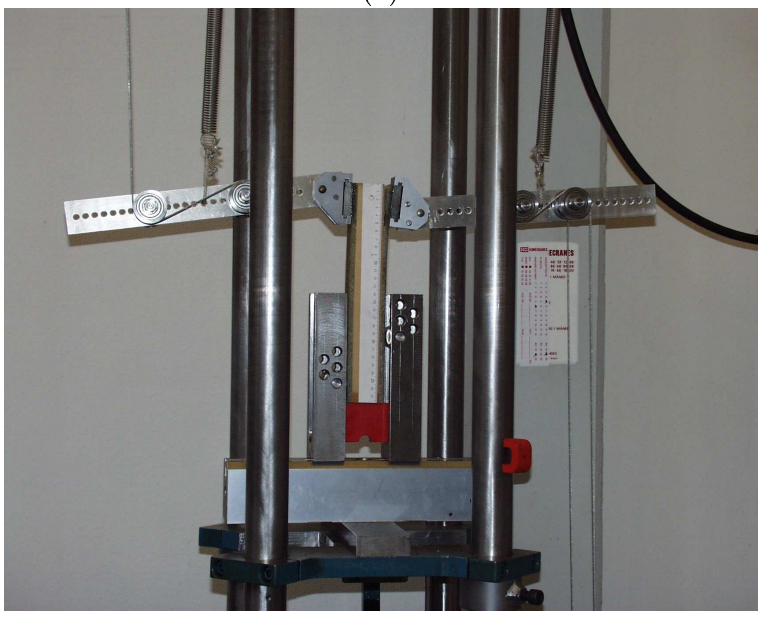

(b)

Figure 18: (a) Sketch of the test setup. (a1) shows the arrangement of the wires that gives $M_2 > 0$ and (a2) shows the arrangement of the wires that gives $M_2 < 0$. (b) Test setup with a specimen mounted.

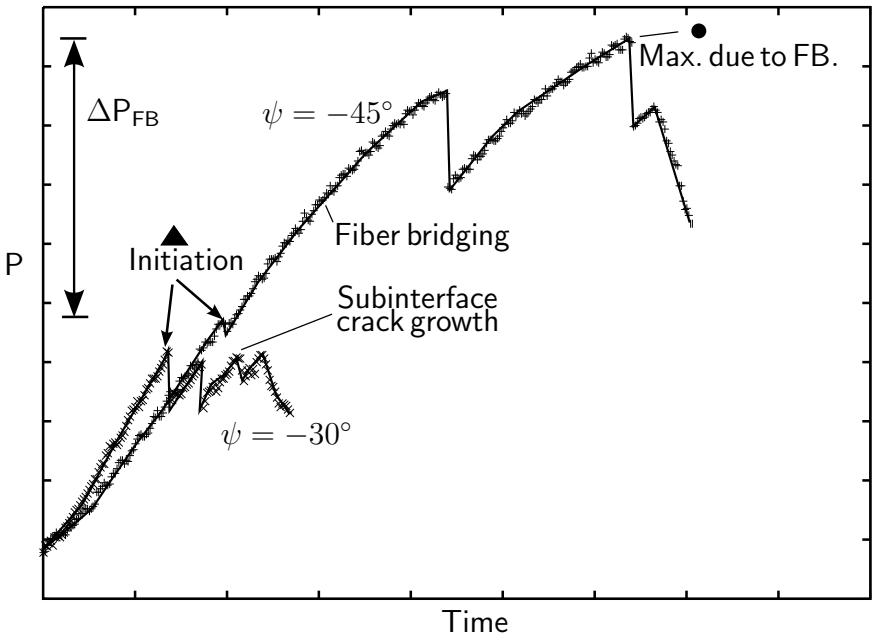

Figure 19: Two distinctively different loading curves for tests dominated by normal opening ($\psi = -30°$) and tests dominated by tangential opening ($\psi = -45°$), respectively.

un-cracked end of the specimen is supported by a roller system that provides a moment $M_3 = M_1 - M_2$. A more detailed description of the test method can be found in (Sørensen et al., 2006). Twelve pre-cracked specimens were tested for each sandwich type.

The applied G was computed from the analytical expression (49) with the reduced load parameters P and M calculated from (42). It must be noted the equations (49) and (42) are derived for a more general load situation consisting of normal forces and moments. In this test only moments are applied and the normal forces are set equal to zero, $P_n = 0$, $n = 1..3$ when computing the reduced loads M and P. The mode mixity ψ was calculated by inserting the moments M_1, M_2 and $M_3 (= M_1 - M_2)$ in (42) and (45).

4.2.3 Results

Figure 19 shows applied wire force versus time for two tests carried out under two different mode mixities; $\psi = -30°$ and $\psi = -45°$, respectively. The curves represent two fundamentally different fracture behaviors.

The curve for $\psi = -30°$ is representative for the behavior observed under mode mixities in the approximate range $-35° < \psi < -15°$ (dominated

normal crack opening): Initially, the load increased almost linearly with time apart from a few minor kinks on the curve. These kinks were not accompanied by any visual changes of crack length. At a critical load value, a major load drop occurred. This was accompanied by a 10-20 mm unstable crack propagation. After this event, the load increased again and propagation occurred at almost the same load level. The crack was either propagating in the core material or in an (apparently) weak plane between the face sheet and core, see figure 21a. Eye-inspection during the test indicated that the fracture process was small compared to the face sheet thickness (extent of plastic deformation was, however, not investigated). For this kind of load curve, the load value at each crack propagation was used as a data point; e.g. the curve for $\psi = -30^\circ$ in figure 19 gave four data points corresponding to the four peaks on the curve.

For mode mixities below -35° (dominated tangential crack opening), another behavior was observed. The curve $\psi = -45^\circ$ is representative for this behavior: Initially 1-2 unstable crack jumps were seen. Then, the crack grew into the CSM layer and fiber bridging was formed, see figure 21b. As shown in figure 19 the load curve for $\psi = -45^\circ$ has a significant increase in fracture resistance (indicated by ΔP_{FB}) after the first onset of growth. Prior to fiber bridging was observed, each point at the onset of crack growth was used as a (▲) data point. As fiber bridging sets in, only the maximum load achieved was used as a (•) data point. Figure 19 shows where these data points are taken from on the load curve.

Test were also made with mode mixities near -5° degrees, but here the crack kinked and grew a distance into the core where it found a stable path. For even larger mode mixities (e.g. $\psi = 10^\circ$) the crack deflected to the opposite side of the core. Crack kinking in sandwich structures is discussed in detail elsewhere (Carlsson et al., 2005). And crack kinking in general (Hutchinson, 1989).

The fracture resistance measured as function of the mode mixity is shown in figures 20a and 20b. The left side of the graphs corresponds to tangential-crack-opening. The right side corresponds normal-crack-opening. The data points are segregated into two types: The triangular data points represents applied energy release rate at crack propagation in the cases where no fiber bridging was observed. Filled circles (•) represent maximum values of the fracture toughness in the cases where an increase in fracture resistance was seen (due to fiber bridging). The thick lines in the figures 20a and 20b are trend curves that are added in order to visualize how the fracture toughness changes with the mode mixity.

The measurements in figure 20 show that for dominating tangential-crack-

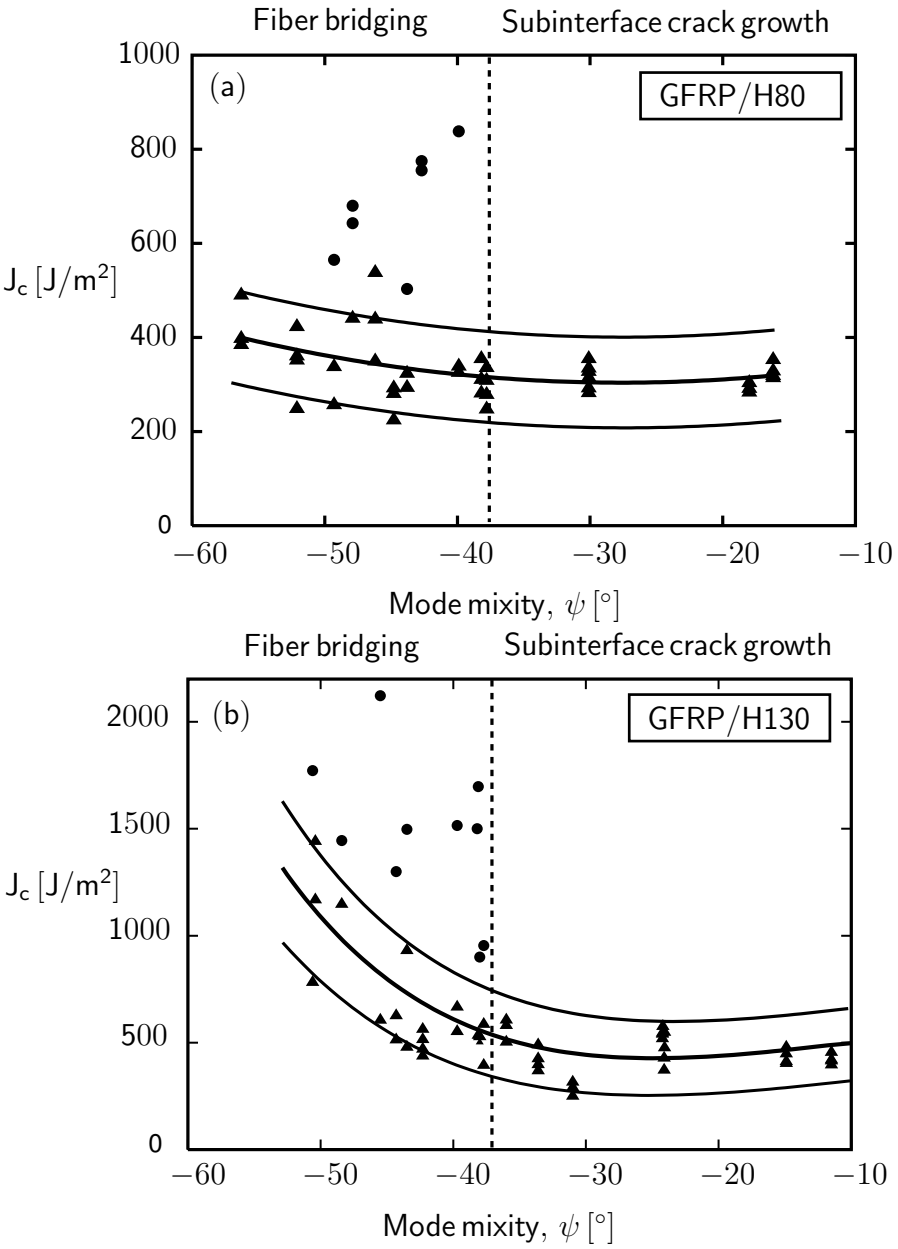

Figure 20: The measured fracture toughness as function of mode mixity. (a) shows the fracture toughness as function of mode mixity for the sandwich configuration with GFRP face sheet and H80 core. (b) GFRP/H130.

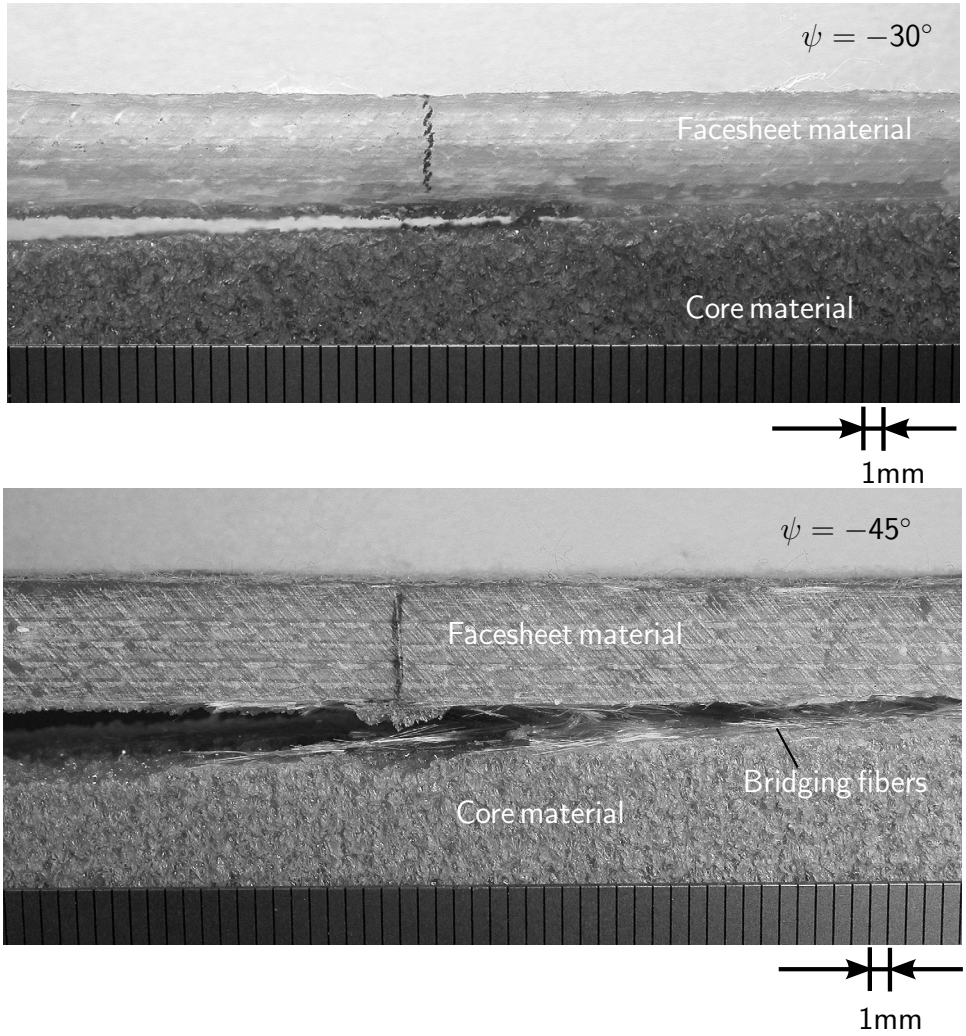

Figure 21: (a) When the specimen has been loaded with normal crack opening the crack grows just below the interface in the core material. (b) Broken fibers are left in the wake of the propagating crack tip.

opening ($\psi \lesssim -35°$) the maximum fracture toughness (•) is significantly higher than the initiation toughness (▲) but for dominated normal-crack-opening ($\psi \gtrsim -35°$) no increase in fracture toughness is seen at all.

For both sandwich structure types, the initiation fracture toughness values (•) are almost constant over the mode mixity range $-10°$ to $-30°$. However, for the sandwich specimen with H130, an increasing trend is apparent when moving left on the horizontal axis.

As mentioned, LEFM is not valid when LSB prevails. Consequently, in the cases where fiber bridging was active the results must be interpreted

with caution. The mode mixity is a LEFM concept so in the cases with fiber bridging this is not strictly invalid. However, the right hand side of (49) is derived using the J-integral that is also valid for large-scale-bridging.

The results in figure 20a and 20b exhibit a significant spread which is typical for sandwich structures. For initiation values the spread was in the order $200\,J/m^2$. For the data points where fiber bridging was present the spread was much larger and in some cases fiber bridging did not even evolve. These fracture property variations could be explained by spatial material property variation.

The literature contains results for interfacial fracture toughness for different sandwich structures. However, the fracture toughness appears to be very sensitive to the exact choice materials. Ratcliffe and Cantwell (2001) measured the fracture toughness of a number of different configurations and found values ranging from $170\,J/m^2$ to $2750\,J/m^2$. For a sandwich specimen with a H80 core various test methods gave an average fracture toughness of approx $2.7 \times 10^2 J/m^2$. In the present study, the fracture toughness values for loading under dominated crack normal opening were approximately $300\,J/m^2$. The discrepancies between our results and those of Ratcliffe and Cantwell (2001) are reasonably small and can be attributed to the dissimilarities in manufacture process and differences in the face sheet lay-up.

4.3 Buckling driven debonding in sandwich structures

Background

Despite its geometrical simplicity, predicting the strength of sandwich structures is complicated since many potential failure modes exist (Allen, 1969; Zenkert, 1995; Fleck and Sridhar, 2002). In general, for structures where more buckling modes (e.g. global buckling and a local buckling mode) are critical near the same external load, severe strength reduction can be experienced because the buckling modes can interact with each other. In that case, the structure can also be strongly sensitive to geometrical imperfections; especially imperfections having the same shape as the buckling modes (Van Der Neut, 1968). This is an undesired feature since even very small imperfections can reduce the strength significantly below that of the perfect structure. Furthermore, interaction of buckling modes results in unstable collapse under load-control. In sandwich structures different buckling modes can potentially interact with each other and cause a reduction of the compressive strength (Hunt et al., 1988; Frostig, 1998; Kim and Sridharan, 2005).

Further complexity is added to the problem when the sandwich structure contains a debond that can grow. A few experimental papers exist

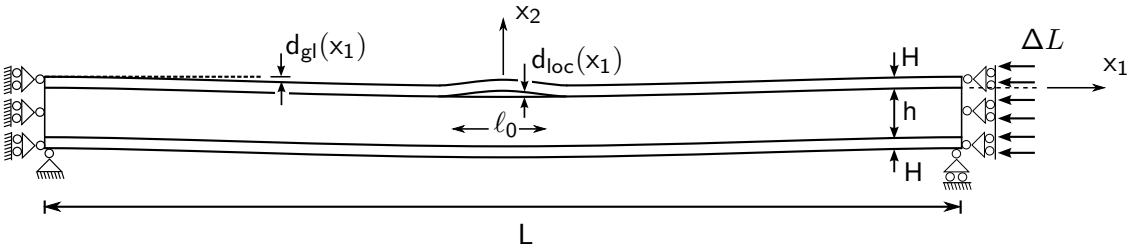

Figure 22: Specification of the analyzeds sandwich column.

Jeelani et al. (2005); Vadakke and Carlsson (2004); Zenkert and Shipsha (2005); Kwon and Yoon (1997) and these confirm that pronounced sensitivity to debond size exists. By modeling Wadee (2002) has shown that when debonding from an initial debond is considered highly unstable snap-back behavior can be expected for the sandwich structure.

4.3.1 The analyzed sandwich column

In the present study we analyze a sandwich column of length L, which has face sheets with thickness H and core with thickness h (see figure 22). Both the face sheet material and the core material are taken to be isotropic and linear elastic. The face sheet material is defined by the Young's modulus E_f and the Poisson's ratio ν_f and the core material is defined by E_c and ν_c.

The column contains a debonded region of length, ℓ_0, located in the interval $-\frac{1}{2}\ell_0 < x_1 < \frac{1}{2}\ell_0$, $x_2 = 0$ (see figure 22). Along the one interface ($x_2 = 0$), the interface bonding is represented by a cohesive law. The cohesive law is described in the section 3.3.

The sandwich column has two sinusoidal geometrical imperfections; a global geometrical imperfection $d^{gl}(x_1)$ of the column axis and a local imperfection, $d^{loc}(x_1)$ of the debonded face sheet, see [P3] for details. The imperfections are characterized by

$$\alpha = \frac{d^{loc}_{max}}{H},\ \beta = \frac{d^{gl}_{max}}{2H+h} \quad \text{and} \quad \xi = \frac{\ell_0}{L}, \tag{50}$$

where d^{loc}_{max} is the amplitude of the local imperfection, $d^{gl}_{max}$is the amplitude of the global imperfection. The choice of α and β as measures of the imperfection amplitude is unpractical in this summary since they are also used for measuring elastic mismatch in earlier sections. The choice was made because α and β were also used as imperfection measures by Van Der Neut (1968).

At $x_1 = L/2$ the sandwich column-end is displaced by a uniform, incremental displacement in the negative x_1-direction. The current end-shortening is denoted ΔL.

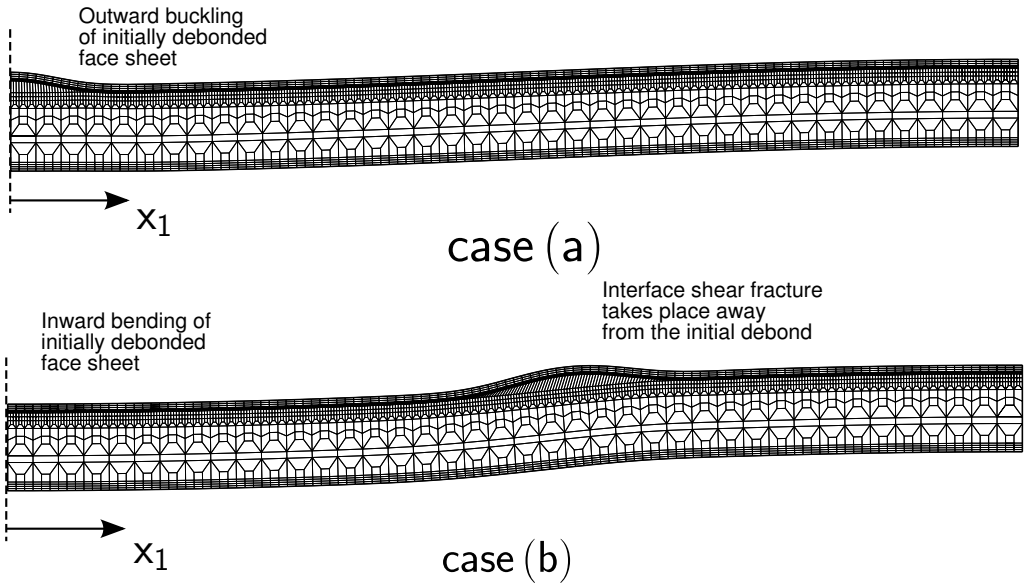

Figure 23: The sandwich column fails by local buckling of the initially debonded face sheet when $\alpha = 0.01$ and $\beta = 0.01$. When $\alpha = 0.0$ and $\beta = 0.01$, the face sheet bends inwards and rests against the core. Eventually an interface crack emerges due to shear stress in the interface. The displacements are scaled $\times$ 10.

4.3.2 Results

Imperfection sensitivity - effect of debond crack growth

The following parameters are taken for the cohesive law:

$$\Gamma = 10^{-6} E_f H,\ u^* = H/10,\ \lambda_1 = 0.01 \text{ and } \lambda_2 = \lambda_1 + 0.4,$$

and these constitute realistic parameters for fiber bridging. In [P3], the influences of the three imperfections ℓ_0/L, α and β are pursued. Initially, the study concerns two cases that result in outward buckling and inward bending of the debond, respectively. The two cases are specified with imperfections given by:

- case (a): $\alpha = 0.01$, $\beta = 0.01$ (outward buckling)
- case (b): $\alpha = 0$, $\beta = 0.01$ (inward bending).

The initial debond length is chosen as $\ell_0/L = 0.075$ for both cases.

Figure 24 shows the responses of the two sandwich columns in terms of normalized axial load P/P^{gl} versus average-column-strain $\Delta L/L$. P^{gl} is

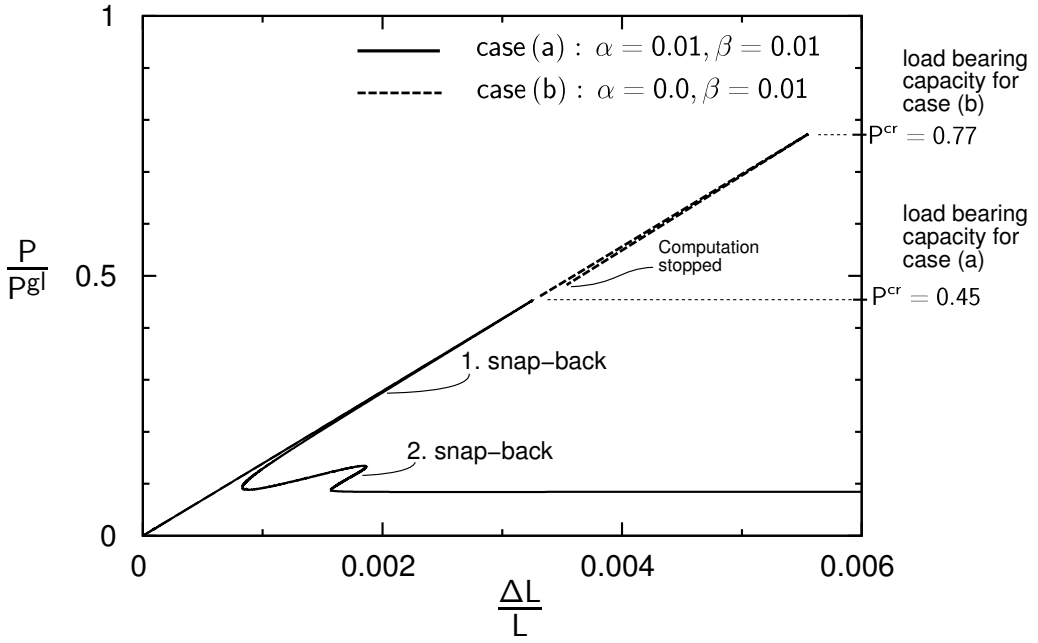

Figure 24: Load curves resulting from two different combinations of the imperfections. In both cases the columns fails by a snap-back. The sandwich column from case (a) failed by local buckling of the face sheet and the sandwich column from case (b) failed by interface sheer fracture.

an analytical prediction of the global buckling load of an intact sandwich column. Initially, the forces rise in a linear manner for increasing average-column-strains. When the load bearing capacities, P^{cr}, are reached both structures suffer unstable snap-back collapse.

For case (a) the collapse takes place at the same time as the debonded face sheet buckles outward and the interface fractures. Figure 23a shows the deformed shape of the sandwich column just after the maximum load for the structure is reached. The displacements are scaled $\times 10$. The post buckling response can be divided into a number of stages that include two snap-backs. The final part of the response for case (a) consists of a horizontal segment that corresponds to the buckling load of the fully debonded sandwich column.

The circumstances associated with the collapse of the sandwich column in case (b) are different: In this case, the debonded face sheet bends inwards and gets supported by the core. Therefore, the load continues to increase and the sandwich structure is compressed beyond the failure level for case (a) where the face sheet buckled outward. However, due to the geometrical imperfections, deformation in the global mode increases as the global buckling load is approached. This makes shear stresses build up in the interface

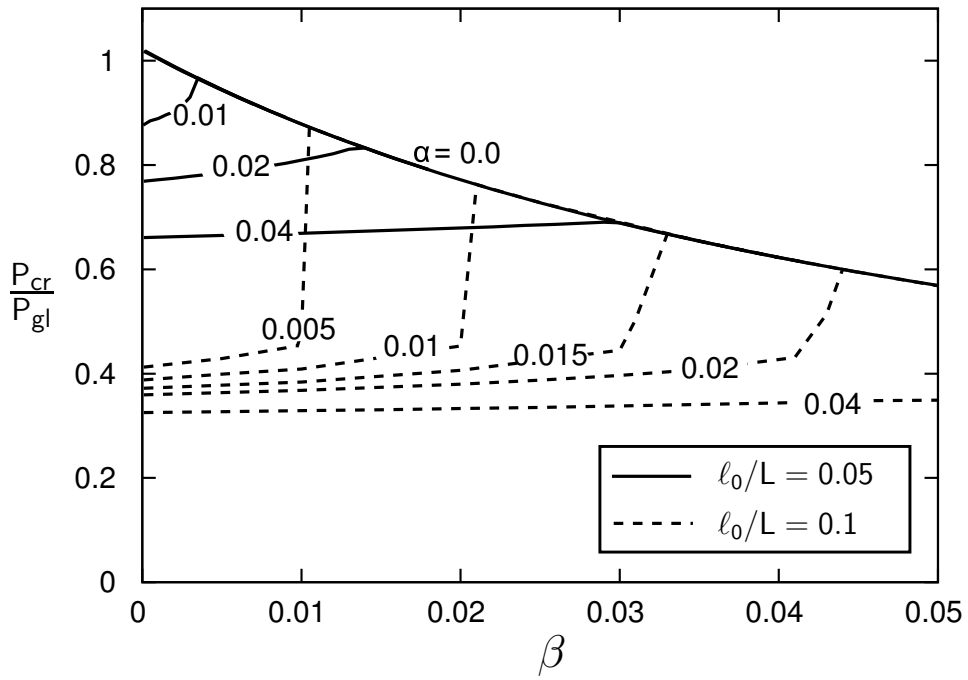

Figure 25: Influence of the global imperfection parameter β and the local imperfection parameter α on the compressive strength of the sandwich structure.

and eventually interface shear fracture initiates near $x_1 = L/4$. At that point the load bearing capacity, P^{cr}, is also reached. The structure experiences unstable snap-back collapse as seen from the dashed line in figure 24 (The computation for case (b) was stopped just after the onset of crack growth). Figure 23b shows a deformed mesh from case (b) with the displacements scaled $\times 10$. The load carrying capacity for the two structures are quite different; for case (a) where the debond buckled outward $P^{cr}/P^{gl} = 0.45$ and for case (b) $P^{cr}/P^{gl} = 0.77$. However, the results for case (b) will be sensitive to the presence of debonds located near the point where the interface shear fracture initiates ($x_1 \approx L/4$).

Inside the window of α and β combinations that result in outward buckling of the face sheet, a significant dependence on α and β is seen. Figure 25 shows the load bearing capacity, P^{cr}, normalized by P^{gl} versus β for a range of α-values and different initial crack lengths, ℓ_0/L.

Taking for instance, $\alpha = 0.01$ and $\ell_0/L = 0.1$, the maximum load increases slightly in the interval $\beta = 0$ to $\beta = 0.021$. In this range, failure starts by the face sheet buckling and debond crack growth, a failure mode as in case (a). At $\beta = 0.021$, the curve displays a rapid rise of the failure load

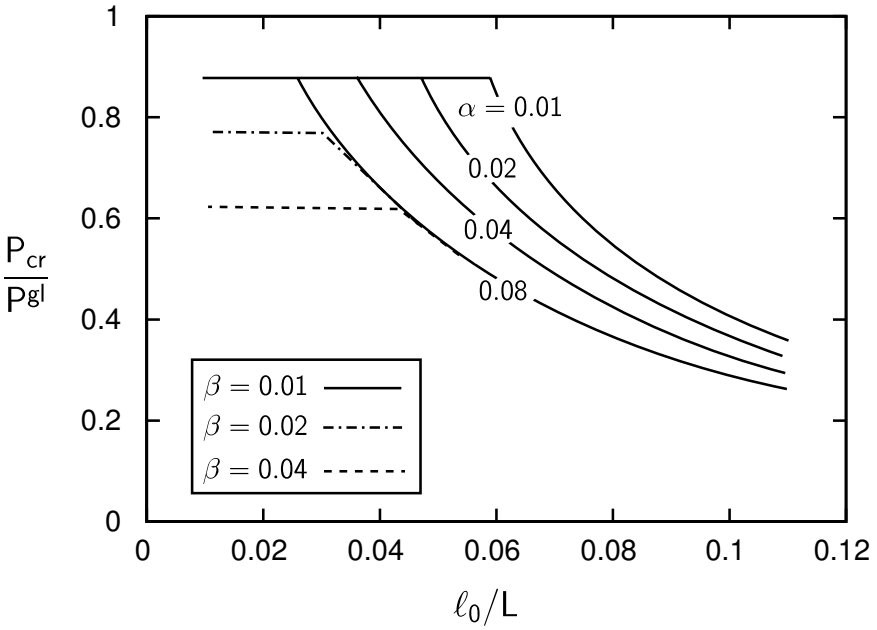

Figure 26: The relation between crack length and maximum load the column can carry.

to $P^{cr}/P^{gl} = 0.76$. This rise reflects the shift in the failure mode into failure by global buckling and interface shear fracture, failure mode as in case (b).

The face sheet imperfection, α, has a strong influence on the load-bearing capacity in the cases where the column fails by outward buckling of the debonded face sheet. For instance, for a debond length $\ell_0/L = 0.05$ and global imperfection $\beta = 0.0035$ the onset of failure is reduced from 87% to 66% of the global buckling load when the face sheet imperfection is increased from $\alpha = 0.01$ to $\alpha = 0.04$. For a real sandwich column having a face sheet thickness $H = 3mm$ the difference between these values corresponds to no more than $90\mu m$. Face sheet irregularities of this order of magnitude are easily encountered. If the face sheets are fiber-reinforced polymers a slightly unsymmetrical lay-up may have imperfections of this magnitude or larger and would seem perfect prior to loading. In an experimental context the imperfection sensitivity implies that severe scatter of the load-bearing capacity can be expected. Other structures that are very sensitive to imperfections such as circular cylindrical shells also exhibit large experimental scatter. For these structures, the imperfection sensitivity has lead to the practice where the theoretical strength is multiplied with a knock-down factor to achieve more useful predictions (Brush and Almroth, 1975).

Another parameter that has a major influence on the load bearing ca-

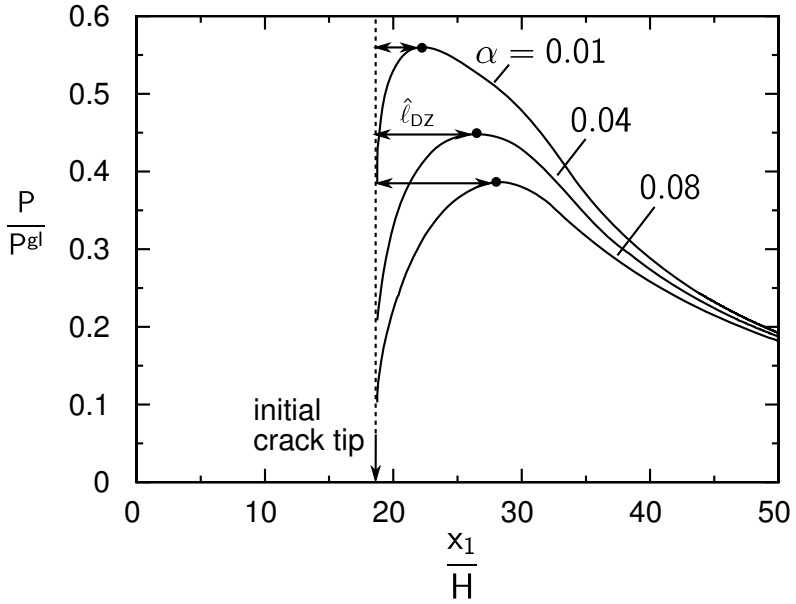

Figure 27: Influence of α on the formation of the damage zone at the debond crack tip.

pacity of the sandwich column is the initial debond length ℓ_0/L. Figure 26 shows the maximum load as a function of the initial debond length. The curves consist of a horizontal line (constant P/P^{gl}) and a decreasing part for increasing ℓ_0/L. When ℓ_0/L is below a critical value, the load reaches the horizontal line at $P_{cr}/P^{gl} = 0.87$, where interface shear fracture takes place as a result of the global buckling, as in case (b). For $\ell_0/L-$values exceeding the critical length, failure mode (a) outward buckling becomes active and the load bearing capacity is rapidly reduced for increasing ℓ_0/L. The critical value of ℓ_0/L is affected by the imperfections α and β as is seen in figure 26: When the face sheet imperfection, α, is increased the critical ℓ_0/L decreases. The column-axis imperfection, β, has the opposite effect - when this is increased the critical $\ell_0/L-$value also increases.

It is of interest to study details near the debond crack tip when the fracture process zone is modeled by a cohesive zone. The dependence on the imperfection amplitude α may be attributed to the crack growth mechanism and the development of a damage zone prior to collapse. In order to clarify this we study how α influences the formation of the fracture process zone.

In figure 27 the horizontal axis is the position, x_1/H, of the damage front and the vertical axis is the load, P/P^{gl}. The lines represent the location of the damage front (x_1-value where $\lambda = \lambda_1$) for different values of α. Taking

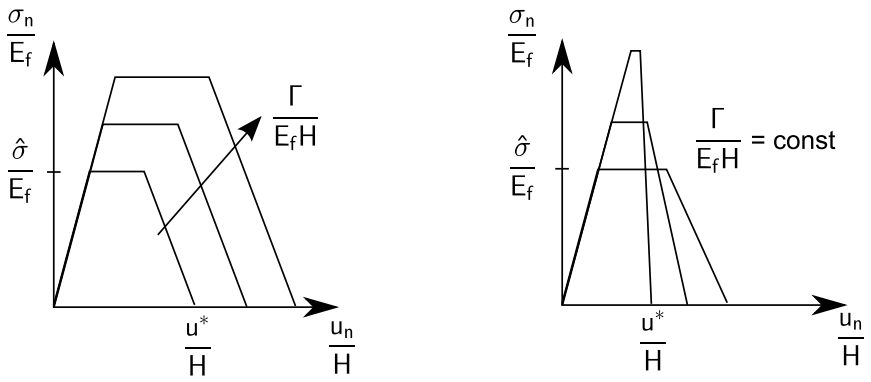

Figure 28: The cohesive law is modified: (a) The work of separation is varied by varying the critical separation, u^*/H, and the maximum cohesive stress $\hat{\sigma}/E_f$ proportionally. (b) $\hat{\sigma}/E_f$ and u^*/H are varied inverse proportionally so the work of separation is kept constant.

for instance $\alpha = 0.02$ the damage front forms at the debond crack tip when $P/P_{gl} = 0.175$. The damage front then moves forward and when it is at $x_1/H = 26$ the maximum load is reached and the load starts to decrease. The different curves show that, for increasing face sheet imperfection, α, the length of the damage zone at the maximum load, $\hat{\ell}_{DZ}$, increases. At the same time, the maximum load the column can carry decreases. A physical explanation of this behavior is now proposed. Initially, the debonded face sheet acts as an imperfect strut that has some rotational flexibility at its ends, $x_1 = \pm\ell_0/2$. Since the interface is very rigid, the rotational flexibility at the ends results mainly from flexibility of the core. However as the sandwich column is loaded, the debonded face sheet bends outward and interface tractions increase. Eventually, the peak stress, $\hat{\sigma}$, is reached and a damage zone starts to develop from the debond crack tip. The damaged zone is softer and adds extra rotational flexibility at the ends of the debond. This makes the face sheet deform like an effectively longer strut and the buckling of it takes place at a lower load.

4.3.3 Effects of modifying the fracture properties of the interface

The non-dimensional interface fracture toughness is modified by changing the critical opening u^*/H and the peak stress $\hat{\sigma}/E_f$ proportionally, see figure 28a. The present results (figure 29a+b) show that increasing the values of the non-dimensional interface fracture toughness raise the post buckling response that ultimately reaches a limit defined by a curve for $\Gamma/E_f H \to \infty$. Along with this tendency, increasing $\Gamma/E_f H$ also changes the characteristics of the

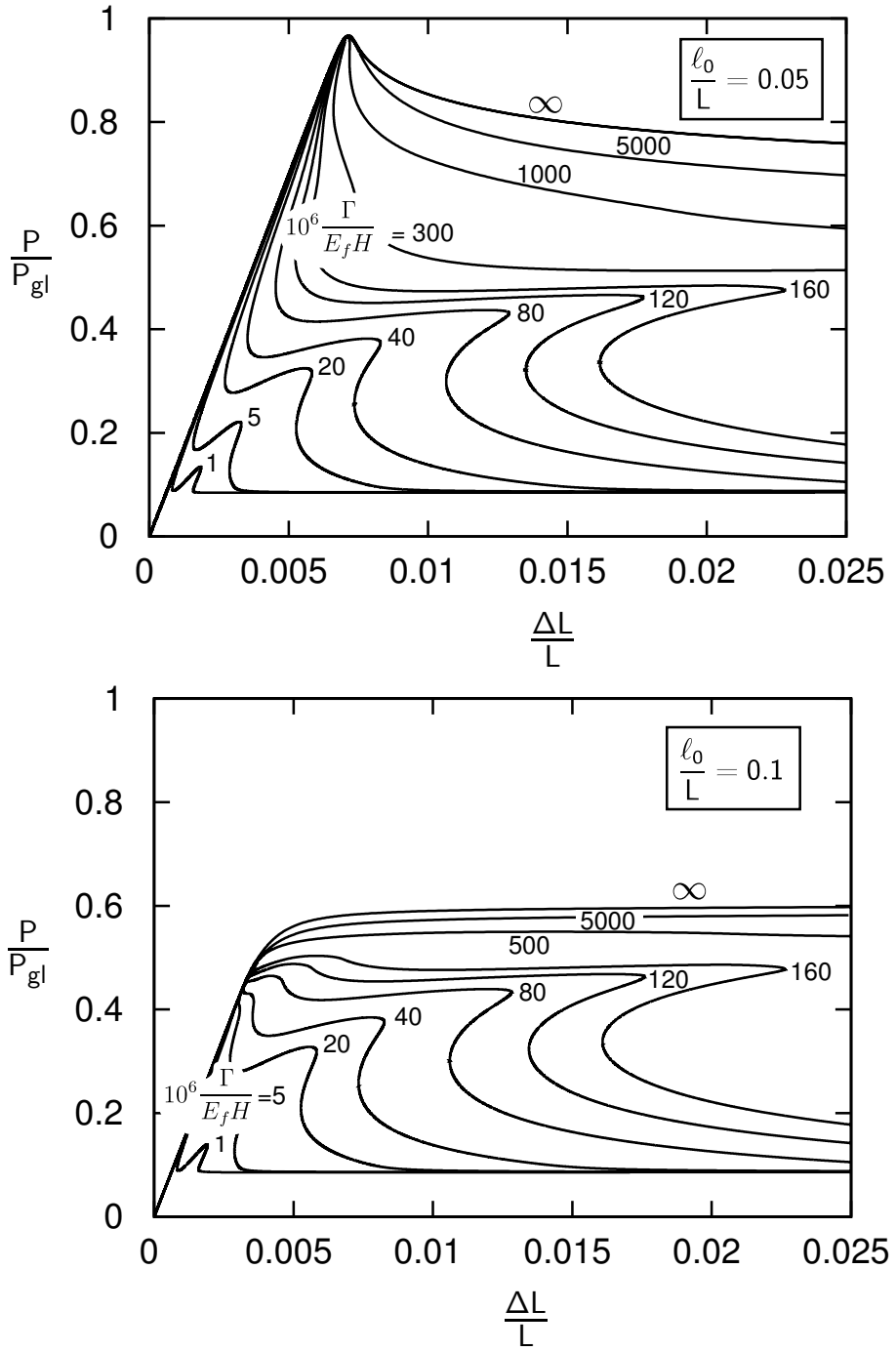

Figure 29: Response of a sandwich columns with debond length $\ell_0/L = 0.05$ and $\ell_0/L = 0.1$, respectively. Results for different interface fracture toughness values are shown. (The imperfections are $\alpha = \beta = 0.01$.)

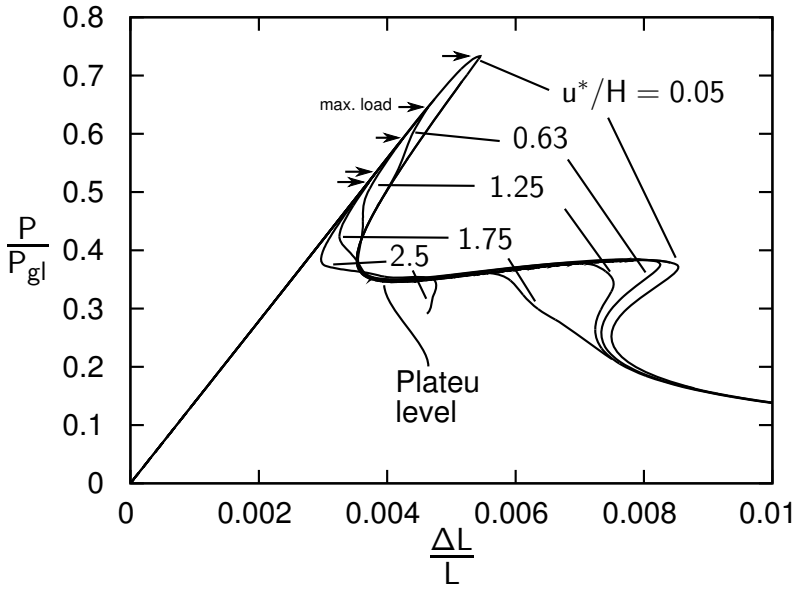

Figure 30: The response of a sandwich column with a interface fracture toughness of $\Gamma/(HE_f \cdot 10^{-6}) = 40$. The curves represents different combinations of $\hat{\sigma}$ and u^*. The maximum loads are indicated by the arrows. (The imperfections are $\alpha = \beta = 0.01$.)

first snap-back. Taking for instance $\ell_0/L = 0.05$ (figure 29a), we see that as the fracture toughness is increased, the slope of the curve right after the maximum load is changed. Thus, the slope is negative for $\Gamma/(E_f H \cdot 10^{-6}) > 1000$. From a practical point-of-view this implies that the structure is stable under prescribed displacement. Taking instead $\ell_0/L = 0.1$ (figure 29b), we see that while $\Gamma/(E_f H \cdot 10^{-6}) = 20$ results in a snap-back, the snap back has disappeared for $\Gamma/(E_f H \cdot 10^{-6}) = 80$. These two examples show the general trend that the longer the debond is, the lower interface fracture toughness is required to ensure stable response under displacement-control.

Now, the response of the sandwich column is computed with different combinations of the critical separation, u^*/H and $\hat{\sigma}/H$ while $\Gamma/E_f H$ kept is unchanged, see figure 28b (the area under the cohesive law is constant and the slope of the initial part is constant). This way of varying the cohesive law represents the effect of changing the type of fracture mechanism. For this study, $\Gamma/(E_f H \cdot 10^{-6}) = 40$ is selected to represent the interface fracture toughness and the initial debond is selected as $\ell_0/L = 0.075$. The results are shown in figure 30 for values of u^* ranging from $0.05H$ to $2.5H$. According to (32) every u^* corresponds to one $\hat{\sigma}$.

The results show that the load carrying capacity increases as u^* decreases

(and $\hat{\sigma}$ increases). This is because, when the interface peak stress, $\hat{\sigma}$, is increased, a larger finite deflection of the debonded face sheet is needed to initiate damage at the crack tip and therefore the sandwich structure fails at a higher external load level.

Figure 30 also shows that after the first snap-back, all curves temporarily coincide at a plateau level that is independent of the actual combination of u^* and $\hat{\sigma}$.

4.4 Prediction of composite scale cohesive laws for delamination with cross-over fiber bridging

4.4.1 Background

Delamination in fiber composites is often accompanied by a zone of bridging ligaments left in the wake of the propagating crack tip. These ligaments have thicknesses ranging from one to several fiber diameters, see figure 31. The ligaments bridge between the crack faces and as the delamination crack is opened further the ligament length ℓ_f is increased by fracture along a fiber/matrix interface. As the ligament is detatched from the crack faces by this process, it exerts forces that tend to reduce the crack opening and inhibit crack propagation, see figure 32. This crack bridging phenomenon is often refered to as *cross-over fiber bridging* and it plays a major role for the fracture resistance under delamination in many fiber composite systems (Foote et al., 1986), (Whitney, 1989), (Hashemi et al., 1990) and the paper [P2].

When the crack faces are separated, the cross-over fiber bridging mechanism takes up energy which increases the fracture resistance of the composite. Although the bridging force from each individual ligament is small, the total energy uptake can be significant. This is because a large number of ligaments are involved and they remain intact to a relatively large opening.

The bonding between fiber and matrix plays an essential role for cross-over fiber bridging; the stronger the fiber and matrix interface is, the larger force is needed to pull the ligament off the crack faces. This also suggests that if the fiber/matrix interface becomes too strong the ligament might fail instead of being detatched from the crack faces. Ligament failure is undesired since the ligament then stops contributing to the fracture resistance. Prior to composite manufacture, the surface of the fibers are chemically treated by a sizing that provides a nanometer thin physico-chemical link between fiber and matrix (Gao and Mader, 2002). One important role for the sizing is to improve the strength of the bonding between fiber and matrix. However, this might not be the most optimum from a composite toughness point of

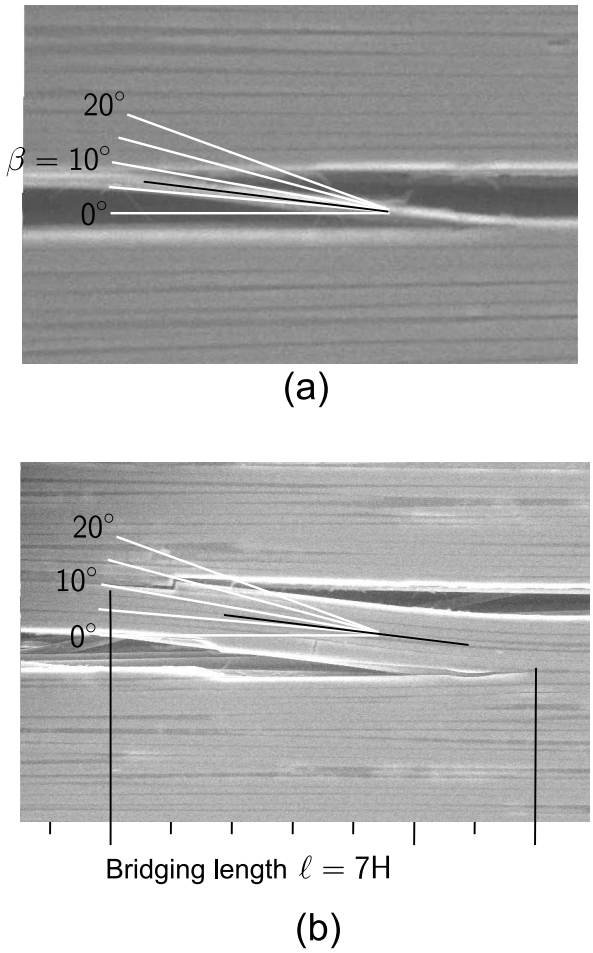

Figure 31: A fiber (a) and a ligament (b) bridging the crack faces during mode I testing of a carbon composite. The picture is taken with an electron microscope during testing. Tests conducted by B.F. Sørensen. The thickness of the ligament is $60\mu m$ and the fiber is $7\mu m$.

view. Feih et al. (2005) has shown experimentally, that a composite with weak bonds between fibers and matrix forms a denser web of bridging fibers than a composite with strong bonds. In their study, they also attempted to measure fracture toughness but their results were inconclusive.

Fiber bridging leads to a rise of the fracture resistance with increasing crack length. This feature is commonly refered to as R-curve behavior and this is highly desired since it facilitates stable cracking behavior e.g. (Broek, 1986). R-curve behavior occurs because the fracture process zone develops: When delamination crack growth has just initiated, only a few ligaments have been formed near the crack initiation point. As the crack tip prop-

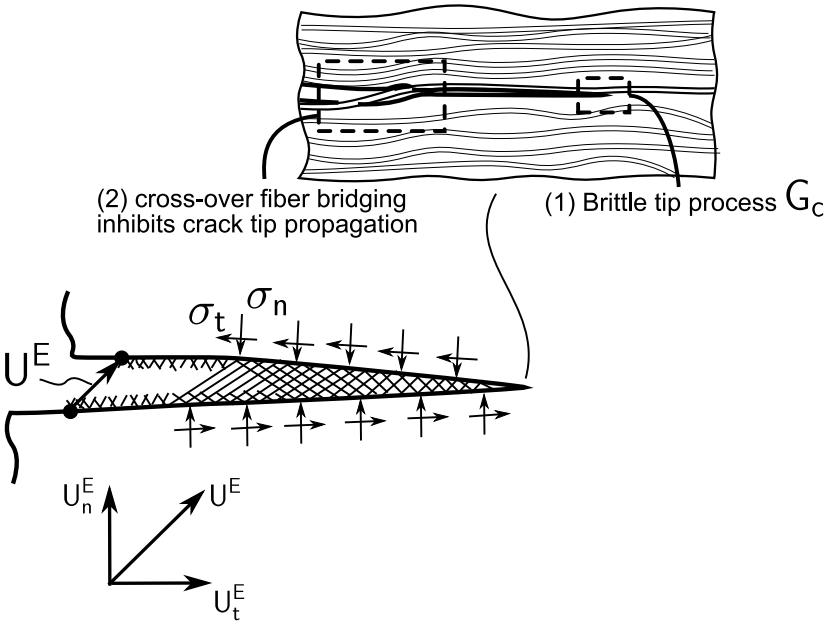

Figure 32: Fibers bridging the crack faces exerts forces on the crack faces that inhibit crack tip propagation.

agates, more and more ligaments are formed and the total energy uptake increases. Usually, at a certain opening magnitude, the ligaments start to break. Then, the fracture process zone is fully developed and it will merely translate along the crack path. R-curve behavior is observed experimentally for both carbon fiber composites and glass fiber composites. Table 1 contains experimental measurements of fracture toughness values for delamination of different composite materials. For most of the materials, rising fracture resistance and fiber bridging were observed. For carbon/epoxy delamination, however, the fracture toughness was constant with crack length. A general observation in Table 1 is that glass fiber composites have a more pronounced rise of the fracture resistance.

The fracture resistance of the composite J_R is linked to the bridging tractions σ_n and σ_t through

$$J_R = \int_0^{U_n^*} \sigma_n dU_n^E + \int_0^{U_t^*} \sigma_t dU_t^E + G_c, \tag{51}$$

where U_n^E and U_t^E are openings at the initial crack tip, U_n^* and U_t^* are openings where the bridging stresses vanish and G_c is the crack tip energy dissipation, see figure 32. When the bridging tractions at the initial crack tip has reached zero $J_R = J_{ss}$.

Material	$G_{Ic}[kJ/m^2]$	J_{ss} $[kJ/m^2]$
Carbon/epoxy[1]	0.3	0.3
Carbon/PES [1]	0.8	2.0
Carbon/Epoxy (intra laminar) [2]	0.3	1.8
Glass/Epoxy [3]	0.3	4.0
Glass/Polyester [3]	0.17	3.8

Table 1: Initiation fracture toughness values and steady state fracture toughness values for delamination in composites. The data are taken from (1) (Hashemi et al., 1990), (2) (Jacobsen and Sørensen, 2001) and (3) (Feih et al., 2005).

Several models of cross-over fiber bridging have already been proposed in the literature. Spearing and Evans (1992) modeled a single fiber by a cantilever beam taking shear deformations into account. The model predicts that the bridging stress decrease asymptotically towards zero as ℓ_f increases. This model we will return to. Kaute et al. (1993) developed a numerical model for ceramic composites based on LEFM. Nandy et al. (1998) made a finite element model that within the frames of LEFM modeled a single fiber and incorporated effects as friction and matrix chipping. These existing models gives a picture of the fundamental behavior of bridging fibers and they even attempt to handle the complex mix of processes observed for ceramic fiber composites (friction, matrix chipping etc.). Experimental measurements of macroscopic cohesive laws for cross-over fiber bridging was conducted by Sørensen and Jacobsen (2003). The present study has emphasis on two aspects of cross-over fiber bridging: a) The link between the matrix/fiber interface properties and the fracture behavior of the composite. b) The response of cross-over fiber bridging under mixed mode loading conditions.

4.4.2 Delamination experiments

A few delamination tests on two types of glass fiber laminates are conducted. The laminates are $5mm$ thick glass fiber/epoxy laminates. Both laminates have Reichold GT 125 resin. Laminate type 1 has PPG 2002 fibers whereas type 2 has PPG 2032. The laminates are filament wet-wounded with an approximated fiber content of 60%. The fiber and resin of laminate type 2 are according to the manufacturer incompatible and therefore a lower fiber/matrix adhesion can be expected. The experiments will be used to measure influence of fiber/matrix bonding strength on the composite fracture behavior.

From the laminates, two DCB specimens for each type are prepared. The specimens consist of the laminate glued in-between two steel bars. The width of the specimens is 30mm. A 30mm long pre-crack is fabricated by sawing and cutting with a razor blade. The specimens are loaded in mode I by symmetric bending moments imposed the fixture also used in [P2], see figure 18. The end-opening, U_n^E, of the initial crack tip was measured using a LVDT, see the wignet in figure 33. The J integral is calculated analytically from the applied moments.

Figure 33 shows measured J versus end-opening, U_n^E. Therefore, the slope of the curves can be interpreted as the cohesive normal stress. Initially, J increases while U_n^E remains zero, however at $J = J_{tip} \approx 250 J/m^2$ crack growth initiates and U_n^E starts to increase. After crack initiation, the crack opening increases and the slopes of the curves reduce. The curve for laminate type 1 continues to flatten out (cohesive stresses continue to decrease) whereas the curves for laminate type 2 attains a constant slope (constant cohesive stress). This effect can be explained by ligament failures in laminate type 1, i.e. it has attained a steady state situation where the fracture process translates along the specimen. At a opening of $40mm$ the bridging stress in lam. type 1 is approximately $\sigma = 5kPa$. For lam type 2 the bridging stress is $20 - 35kPa$. The final fracture toughness values J_{ss} obtained when the measurements were stopped were higher and still increasing for the lam. type 2 i.e. it does not reach a steady state situation.

4.4.3 Model specification

The micromechanical model consists of an elastic isotropic ligament of height H that is bonded to two elastic isotropic substrates (see figure 34). The height of the substrates are h and the length is denoted L. The elastic constants, Young's modulus and Poisson's ratios, for the ligament and substrate are E_f, ν_f and E_m, ν_m, respectively. Initially, the free ligament length, ℓ_f, is zero and it is bonded to the upper substrate along $x_1 = [0, -L/2]$, $x_2 = 0$ and the lower substrate along $x_1 = [0, L/2]$, $x_2 = -H$.

The solution is obtained by incremental displacements $\dot{U}_n$ and $\dot{U}_t$ of the outer edge at $x_2 = h$. The lower boundary of the unit cell, $x_2 = -h - H$, is clamped. The vertical ends, $x_1 = \pm L/2$, of the substrates are traction free.

The tangential force, P_t, and the normal forces, P_n, from a single ligament are found as the sum of the nodal forces along $x_2 = h$. The force-displacement response from the ligament is cast into the form of a composite cohesive law by assuming that a spacing ℓ exists in-between the ligaments and that they

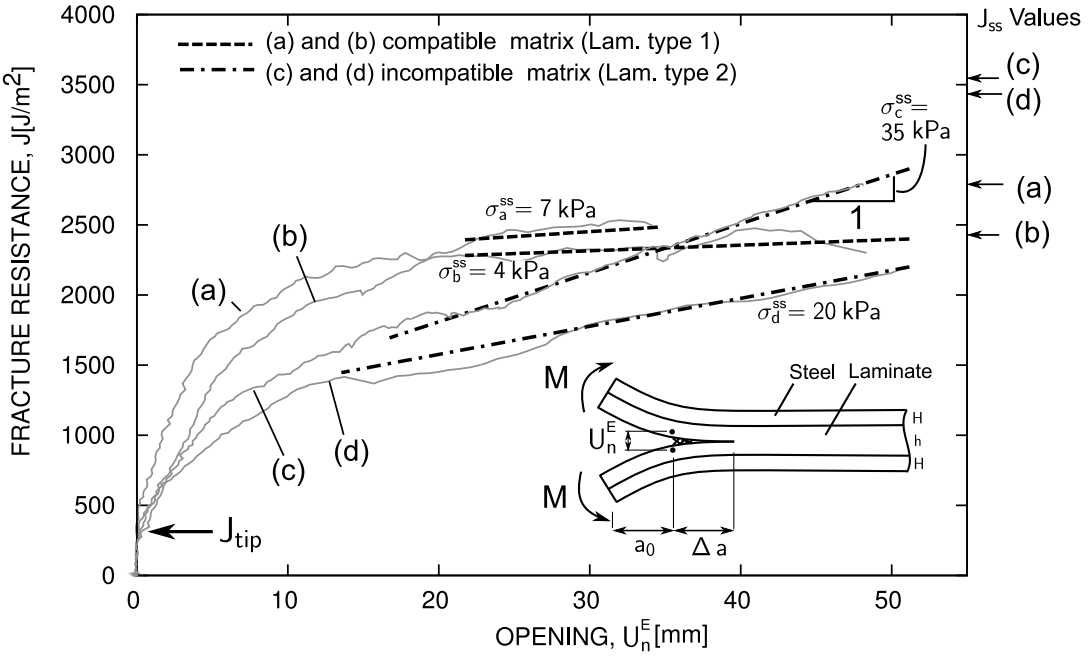

Figure 33: Resistance curves for laminates

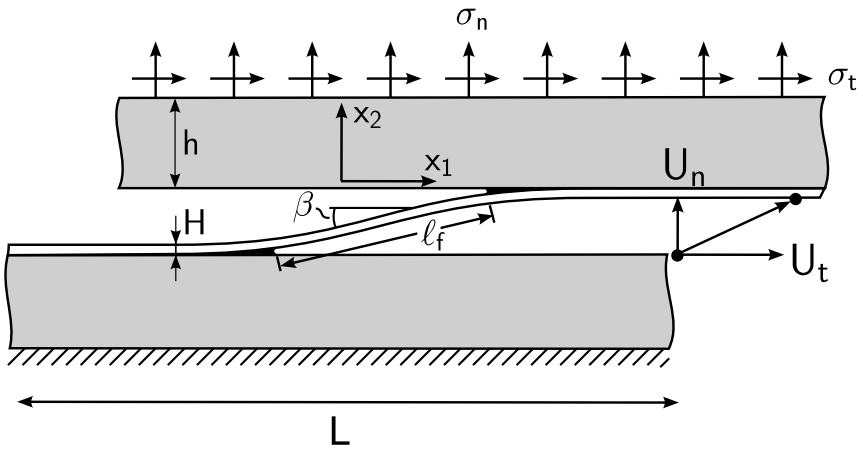

Figure 34: Model consists of an elastic ligament bridging two elastic substrated; here it is shown in a deformed stage. In the undeformed configuation $U_n = U_t = \ell_f = 0$.

all behave identically:

$$\frac{\sigma_n(U_n/H)\ell}{E_f H} = \frac{P_n}{E_f H} \quad \text{and} \quad \frac{\sigma_t(U_t/H)\ell}{E_f H} = \frac{P_t}{E_f H}.$$

Fiber / matrix fracture is modeled by a cohesive zone. The used cohesive law is a slightly modified version of the cohesive law presented in section 3.3. Here, the stresses are instead given as

$$\sigma_n^I = \frac{u_n}{u_n^*}\frac{\sigma(\lambda)}{\lambda} \text{ and } \sigma_t^I = \alpha\frac{u_t}{u_t^*}\frac{\sigma(\lambda)}{\lambda}, \tag{52}$$

where, $\alpha = \Gamma_t/\Gamma_n$ is a shielding parameter that relates the interface toughness in pure normal-opening, Γ_n, and the interface toughness in pure tangential sliding Γ_t (Tvergaard, 1990). Γ_n is given by equation 32.

We select a material combination that mimic a typical glass/epoxy fiber composite: The elastic properties of the problem are specified by $E_f/E_m = 20$ and $\nu_f = \nu_m = 0.3$ i.e. the ligament has properties as a glass fiber and the substrate has properties as a polymer resin. However, an initial study has indicated that the influences of H/h and E_f/E_m are generally small. Doubling the parameters one at the time only change the bridging stress predictions in the order 10%.

The cohesive law is specified with the critical openings $u_n^* = \frac{H}{20}$ and $u_t^* = \sqrt{\alpha}\frac{H}{20}$. Unless otherwise mentioned, the results presented are obtained with $\alpha = 1$ and the fracture toughness of the interface in pure normal separation taken as $\frac{\Gamma_n}{HE_f} = 5 \times 10^{-5}$. Furthermore, the shape parameters are taken as $\lambda_1 = 0.1$ and $\lambda_2 = 0.5$.

We model bridging ligaments that during the process attain lengths exceeding $\ell = 150H$. Obtaining such results in one continuous computation would be computationally very costly because the mesh must be very refined along the crack path. Therefore, the solution for the full bridging response is instead obtained by a special scheme where solutions for different initial bridging lengths are interconnected: First, a solution is obtained in which the free ligament length grows from $\ell_f = 0$ to $\ell_f \approx 25$. Then, a solution for a longer free ligament is obtained from a new independent computation using a different mesh. This mesh has a finite initial bridging length that is accommodated by extending the ligament by a number of coarser elements, see figure 35. Each curve presented in this study, typically consists of results from 10 individual computations. From the computations with initial crack lengths only the results obtained when the fracture process zone is fully developed are included. The results are interconnected to form a single continuous curve.

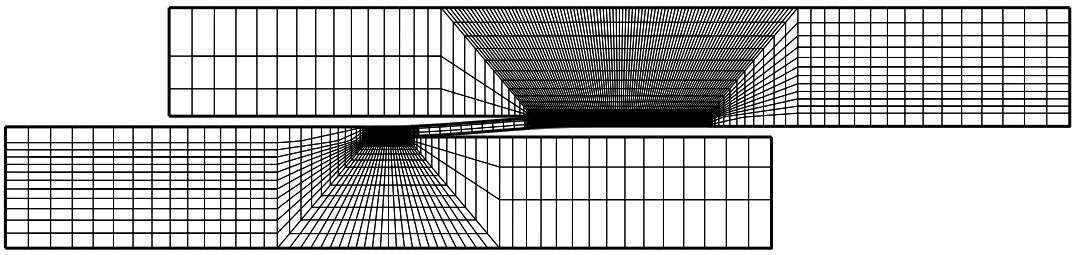

Figure 35: Deformed mesh with an initial fiber length.

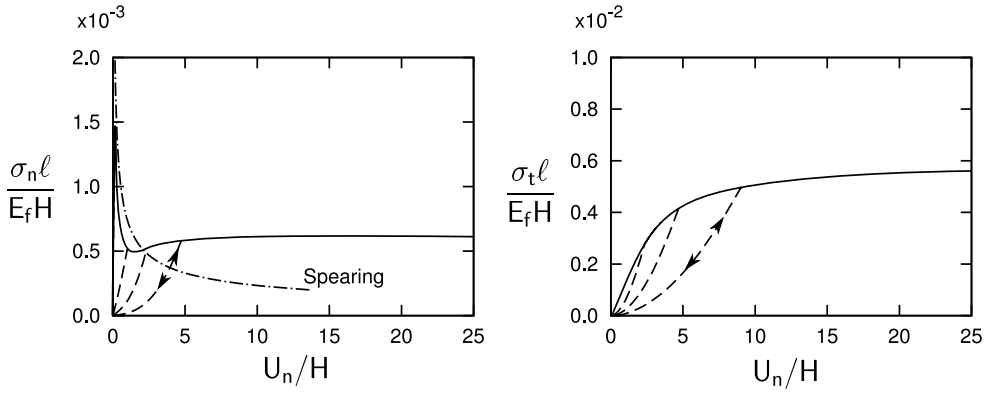

Figure 36: The normalized bridging tangential stress and normal stress (solid lines) from a pure normal opening case. The dash-dot line is a prediction from an analytical model by Spearing and Evans (1992). The dashed lines represent unloading curves.

The finite element program used is a large strain implementation with 8 noded isoparametric solid elements and 6 noded cohesive elements. For the solution the Rayleigh-Ritz finite element method described section 3.4 are used.

4.4.4 Results for pure normal opening

Figure 36 shows the response of a bridging ligament in terms of normalized bridging stress ($\sigma_n \ell / HE_f$ and $\sigma_t \ell / HE_f$) against normalized opening, U_n/H. In the initial stage, the bridging normal stresses rises linearly with opening. Upon a peak normal stress ($\sigma_n \ell / E_f H = 1.5 \cdot 10^{-3}$) is reached, the bridging normal stress decreases until the crack is opened approximately $2H$. Next, a small increase in bridging normal stress follows and, finally, a plateau level is attained. Concerning the bridging tangential stress versus normal-opening, the initial behavior is also linear. Then, the stress continues to increase to

a plateau level in a non-linear, monotonic manner. This plateau level is an order of magnitude higher than the plateau normal stress. However, under pure normal opening ($U_t \equiv 0$) the tangential force does not contribute, see equation 51.

If the loading is reversed, after the ligament length ℓ_f is increased, the crack faces close but the compliance of the system is changed. In figure 36 the unloading paths for initial lengths of $\ell_f/H = 10$, $\ell_f/H = 20$ and $\ell_f/H = 40$ are shown (dashed lines). Upon reloading, the dashed curves are followed until interface cracking takes place again.

The dash-dot line in figure 36 represents the bridging stress from a simple analytical model proposed by Spearing and Evans (1992). In that model, the bridging ligament is fixed on a rigid substrate and is modeled with Timoshenko beam theory and LEFM. In the initial stage, the predictions show the same trends. However, when the opening is $U_n/H \approx 2$ the predictions starts to diverge. The bridging stress from the analytical model continues to decrease towards zero whereas the prediction from the present model attains a steady state value. This difference in the predictions is attributed to axial stretching of the ligament that the present finite element model captures. The existence of a steady state bridging stress implies that the ligament will continue to contribute to the fracture toughness of the composite as long as it does not break.

Influence of fiber/matrix interface properties

Here, the influence of fiber/matrix adhesion is investigated by varying $\Gamma/E_f H$. Predictions of bridging stress for different values of $\Gamma/E_f H$ are shown in figure 37. The results show a significant dependence of the interface toughness value; the bridging stress increases as the toughness is increased.

Figure 38 shows a contour plot of the principal stress in the ligament. During the detachment, the stresses are concentrated around the crack tip. In the plot, the opening is approrimately $2/3H$ and the maximum principal stress is about $\sigma^{max}/E_f = 0.025$. Figure 39 shows the maximum principal stress in the ligament against the opening for a range of toughness values; the principal stress in the ligament increases the larger the interface toughness is. It is noted that the stresses in the ligament are lowest initially when the bridging stress is largest.

A simple criterion is applied to predict ligament failure. The ligament is assumed to break when maximum principal stress exceeds the material strength that we assume to be a constant. Typical values for the strength of glass fibers are $\sigma^{uts}/E_f \approx 0.03$ and for carbon fibers $\sigma^{uts}/E_f \approx 0.015$ (Karbaek and Lilholt, 1993). In figure 39, two horizontal lines indicate these

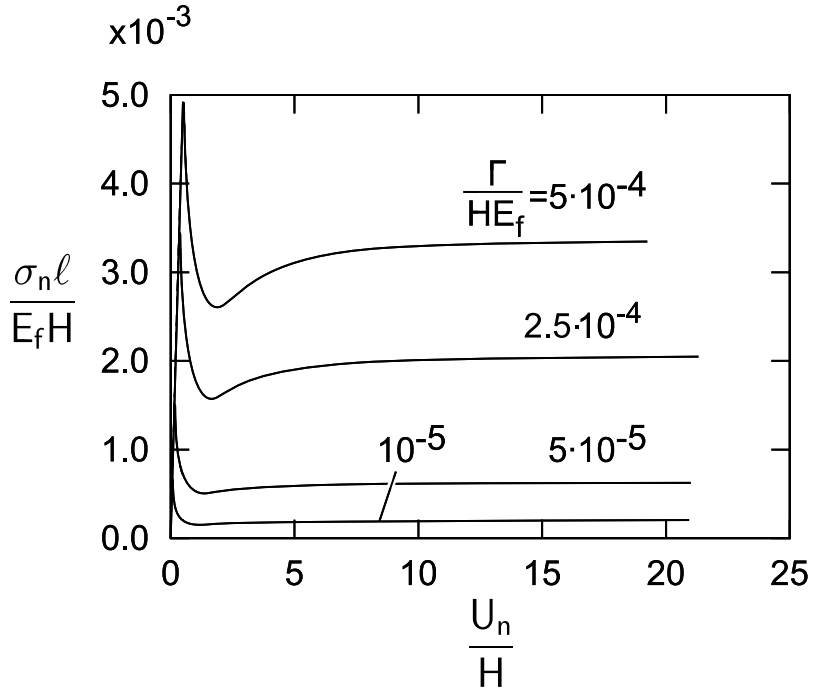

Figure 37: The bridging stress for various values of $\Gamma/E_f H$.

values. From experimental data on silica-glass bonded to epoxy (Nakamura et al., 2007), it is calculated that the non-dimensional interface toughness, $\Gamma/E_f H$, for a single fiber bonded to epoxy is $\approx 5 \cdot 10^{-5}$. Since the curve for $5 \cdot 10^{-5}$ does not cross the line for the glass fiber strength, the ligament will stay intact. For a single carbon fiber / epoxy interface $\Gamma/HE_f \approx 10^{-4}$ (Drews et al., 2007) and, therefore, fiber fracture is predicted in the very early stage of the bridging process. It is emphasized that the fracture criterion is rather inaccurate since strengths of glass and carbon fibers scale with the size of the stressed volume. A more accurate prediction could be obtained by incorporating Weibull statistics in the analysis. Nevertheless, the predictions from figure 39 that carbon/epoxy should only experience limited fiber bridging whereas glass/epoxy should possess more fiber bridging are consistent with experimental findings, see Table 1. It would be desirable to measure fiber/matrix interface adhesion experimentally. If this can be done, the effects of different fiber-surface treatments could be measured directly instead of getting an indirect indication through the resulting composite fracture behavior.

The ligament inclination β comprises a measurable characteristic of the bridging process, see figure 31. However the question is how strong β is influ-

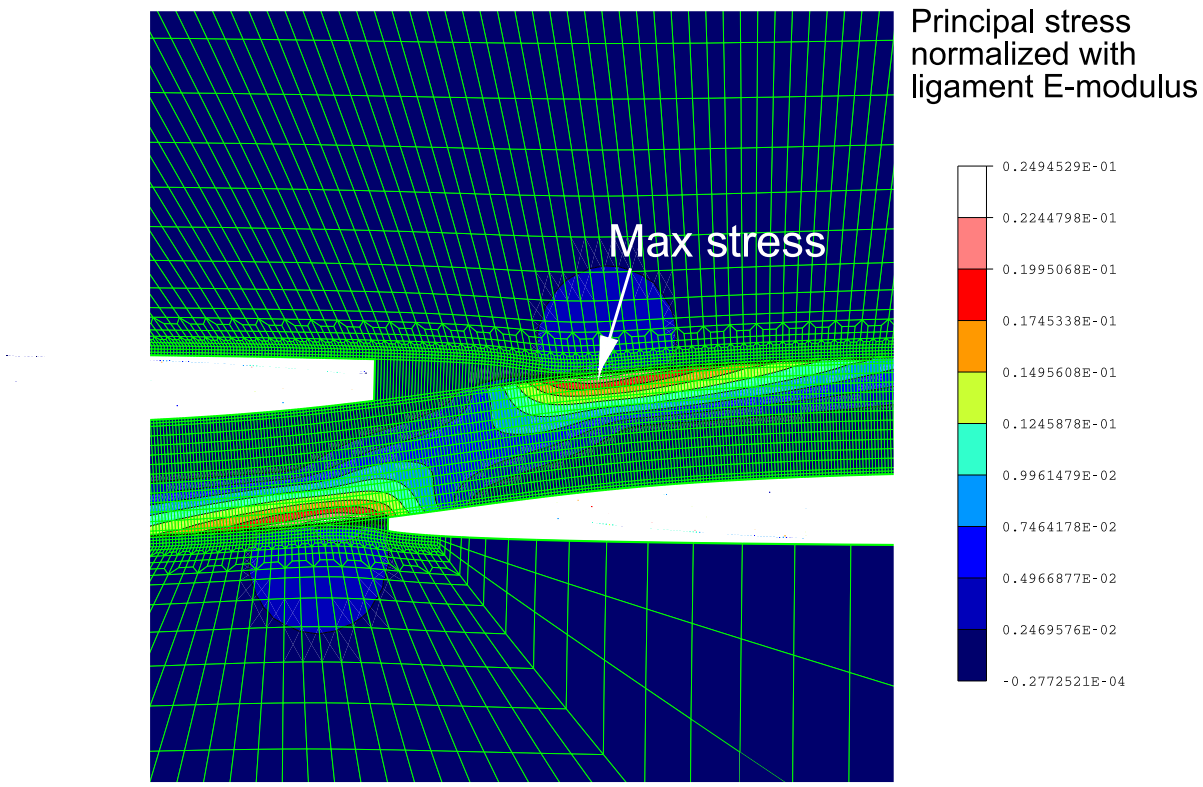

Figure 38: Contour plot of the principal stress in the fiber. The maximum stress is located at the crack tips.

enced by the interface properties. Here, we compute the ligament inclination versus crack opening to investigate if this could be used as a measure to estimate the fiber/matrix adhesion.

Figure 40 shows the ligament inclination as function of the crack opening for different values of Γ/HE_f. The curves have approximately identical shapes; they start at an elevated value that decreases to a plateau value. Unfortunately, the inclination has only a weak dependence on the toughness. Doubling Γ only changes β $1-2^\circ$. This suggests that measurements of β may not be an accurate way of determining Γ. For instance, for the

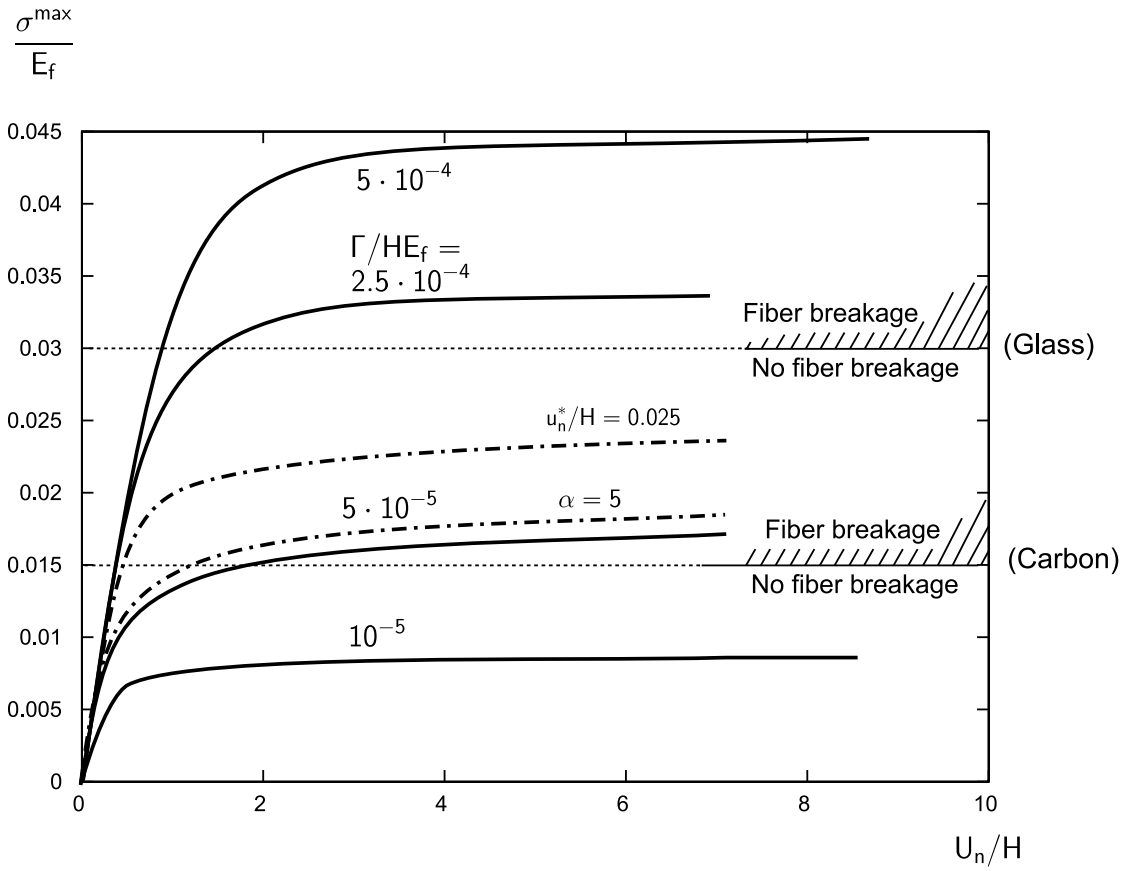

Figure 39: Maximum stress in the fiber for different interface toughness values.

carbon composite in figure 31 the fiber and ligament the inclination is approximately $\beta \approx 7°$. From the results, this imply that $\Gamma \approx 5 \cdot 10^{-5} \cdot HE_f = 5 \cdot 10^{-5} \cdot 7\mu m \cdot 300GPa = 105J/m^2$. For the ligament we assume that the effective modulus is $E = E_{carbon}V_f = 300GPa \cdot 60\% = 180GPa$. Calculating the fracture toughness using $H = 60\mu m$ it is found that $\Gamma = 540J/m^2$. It seems reasonable that the fiber/matrix fracture toughness Γ should be the same, irrespective of the ligament thickness. Therefore, the example clearly shows that the large sensitivity to Γ/HE_f makes the proposed method useless for accurate determinations of the fracture toughness.

Experimental measurements of fracture toughness of interfaces have shown that some interfaces exhibit asymmetric shielding i.e. measured interface toughness is a function of the mode of opening of the crack. Liechti and Chai (1992) measured that the interface of glass bonded to epoxy is significantly tougher when the cracking takes place under a tangential crack-

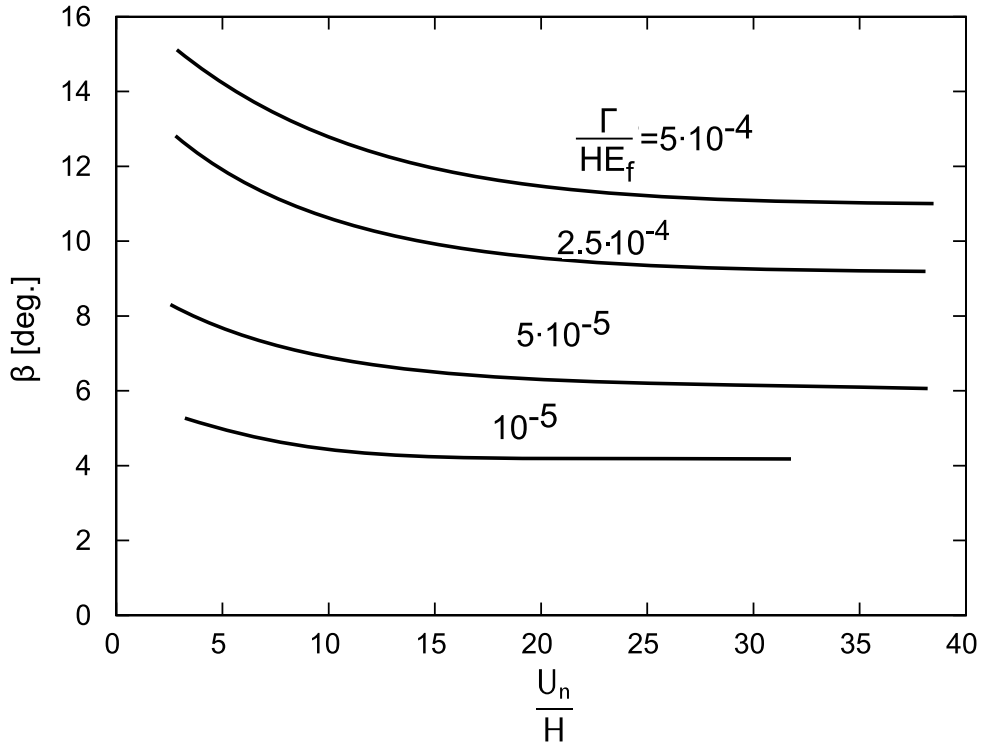

Figure 40: Fiber orientation during mode I opening for different interface toughness values.

opening mode than under normal-crack opening. Tvergaard and Hutchinson (1993) predicted that this effect results from increased plastic deformation zone under mode II dominated loading.

In the present work, we model asymmetric shielding by a cohesive law that has a factor α higher toughness for tangential crack-opening than for normal crack opening. Figure 41 shows the mode I response of the ligament for different values of α ranging from 1 to 10. The initial part of the process is unaffected by α but after the maximum load is reached the solutions start to diverge markedly. However, the difference between $\alpha = 5$ and $\alpha = 10$ is small.

The observed behavior results from a change of the mode of cracking at the fiber/matrix interface crack tip. Initially, the crack is normal opening dominated but in the later stage the amount of tangential-sliding is increased.

The cohesive zone model of the fracture process has an incorporated length scale in terms of the critical separations u_n^* and u_t^*. In this section we use $u_t^* = u_n^* = u^*$. For a fixed Γ/HE_f, the peak stress, $\hat{\sigma}$, and the critical separation, u^*, have large influence on the extend of the fracture process zone

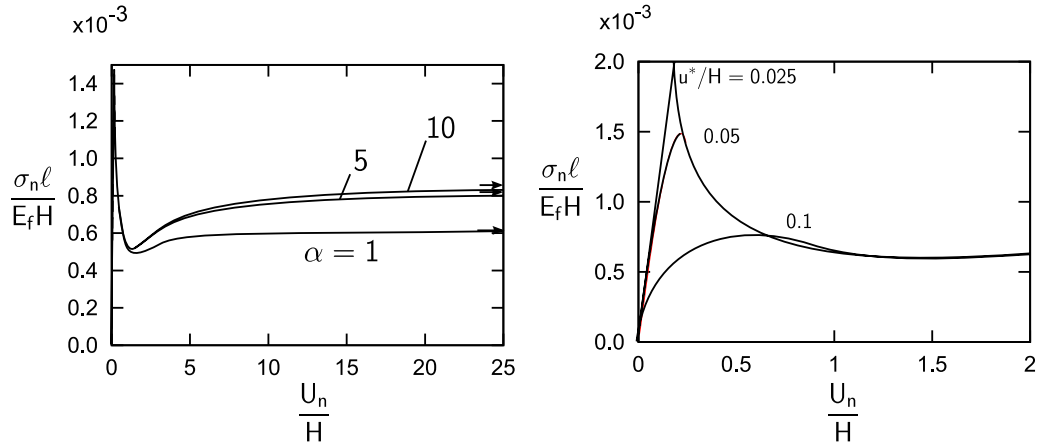

Figure 41: (a) Fiber bridging response for different degrees of assymetric shielding. (b) influence of critical opening to fiber thickness.

(FPZ), i.e. interface area where $\lambda_1 < \lambda < 1$. For small critical separation and high peak stress, the extend of the FPZ is small. In contrast, if the critical separation is large and the peak stress low the extend of the FPZ is large.

In figure 41b the work of separation for the cohesive law $\Gamma/E_f H$ is kept constant while u^*/H and $\hat{\sigma}/E_f$ are varied. The results show that the choice of critical separation and peak stress influence mainly the initial stage ($U_n/H < 1$). The results show that the maximum bridging stress increases as u^*/H is decreased.

4.4.5 Mixed mode loading

The present section comprises initial results for cross-over fiber bridging under mixed mode loading conditions. Mixed mode loadings are interesting to study since for many cracked structures mixed mode loading conditions are governing. The mode of the loading is defined as $\varphi = \tan^{-1} U_t/U_n$.

The bridging normal stresses for $\varphi = 0°$, $\pm 15°$, $\pm 30°$ and $\pm 60°$ are shown in figure 42. For the discussion of the curves they are divided into different groups.

The curves for $\varphi \geq 0$ represent ligaments that becomes loaded in tension during loading: Initially the curves increase linearly to a peak stress that is only weakly influenced by the mode of loading. Next, they decrease and reach a plateau level. The larger φ is the lower this plateau level is. The highest plateau bridging stresses are attained for $\varphi = 0$.

The curves $\varphi = -30°$ and $-60°$ are fundamentally different. Initially, the normal stress increases to a peak stress value. Then it decreases to a negative

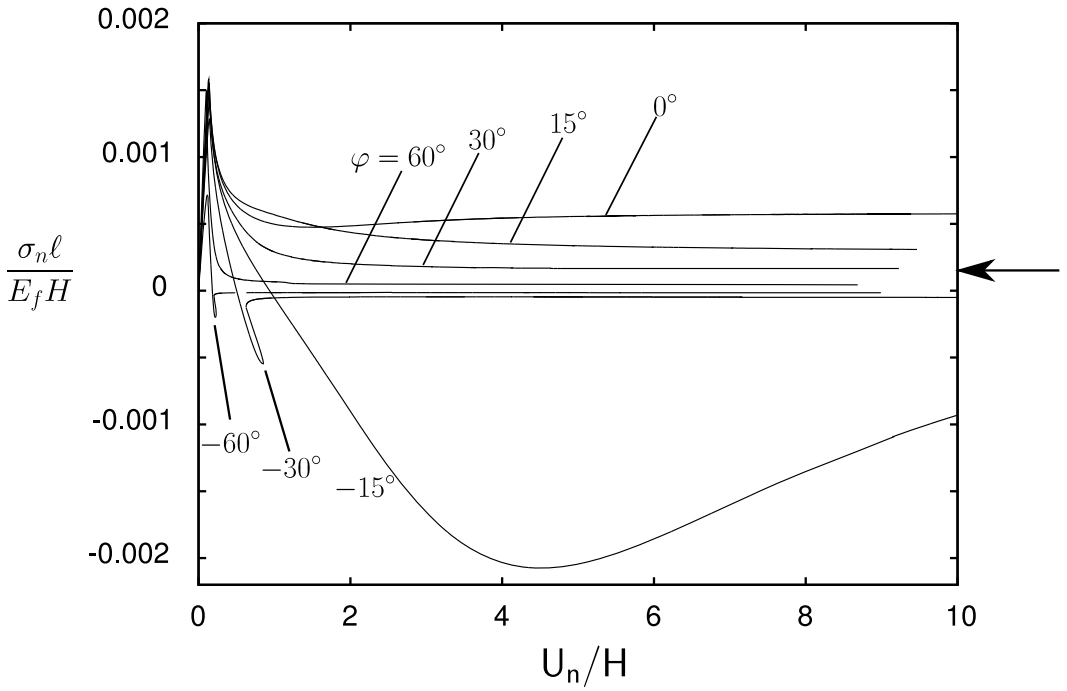

Figure 42: Bridging normal stress for different modes of opening

value. At a critical value, a snap-back appears and the stress approaches zero. This curve is a result of a complex buckling and debonding process. The negative bridging stresses values develop because the partly debonded ligament acts as a stiff strut that is squeezed between the crack faces. As the loading is continued, the strut eventually looses its stability. At the same time the interface fractures which results in the snap-back behavior.

Compared to $\varphi = -30$ and $-60°$, the curve for $\varphi = -15°$ does not exhibit the snap back. This is because the strut-effect forces the interface crack to be closed in the normal direction so fiber/matrix fracture becomes difficult. Consequently, significant negative bridging stresses develop; this will tend to open the crack faces instead of holding them together.

Concerning the tangential stresses the curves for $\varphi = 15°$, $30°$ and $60°$ are fairly alike and the plateau levels that they reach are very close i.e. $\sigma_t \ell / E_f H = 0.01$. Concerning $\varphi < 0°$ the curves reflect the behavior accounted for above. For $\varphi = -30°$ and $-60°$, $\sigma_t \ell / E_f H = 0.01$ is reached and rapidly followed by a snap-back caused by buckling of the ligament. For $\varphi = -15°$ the ligament does not buckle and therefore the fiber contributes to the composite fracture toughness.

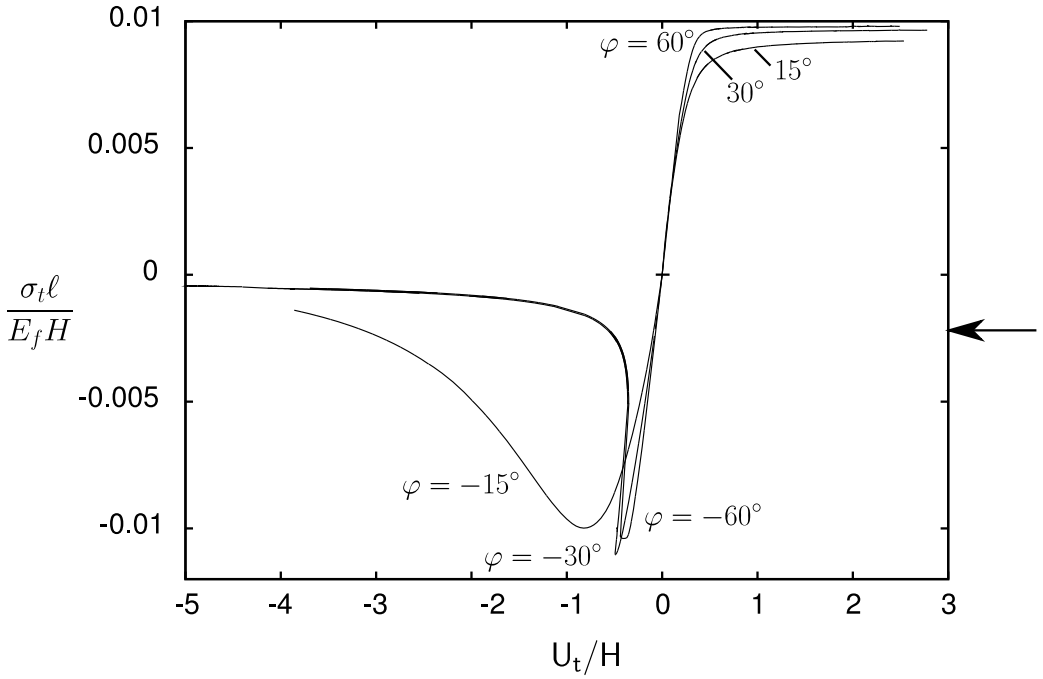

Figure 43: Bridging tangential stress for different modes of opening

4.4.6 Perspectives of the micromechanical model results

The numerical results obtained in this study show that tougher composites can be manufactured by the counter-intuitive process of using incompatible fiber and resin together. The numerical results support this conclusion since the model predicts that an optimum bonding strength exists. A paradox exists in the comparison between the numerical results and the experimental results. The numerical results predict that in the cases where the ligament breaks this happens rather early in the process i.e. $U_n < 20H$. Therefore, the model predicts steady state at that opening. However, for lam. type 1 steady state was attained around $U_n = 20mm$ (approximately 50 times larger opening). This discrepancy between the model and the experiments may be explained by the assumption that the material strength is a constant. In reality, the strength of a glass fiber loaded in tension decreases with the length of the fiber. Therefore the line in figure 39 should curve downwards towards the right side of the figure. In that case, the fiber would be able to survive the initial stage of the process and then break because its strength is reduced with the its length ℓ_f.

In order to link the above predictions to true composite behavior, more knowledge about the fracture process must be obtained. How many thick

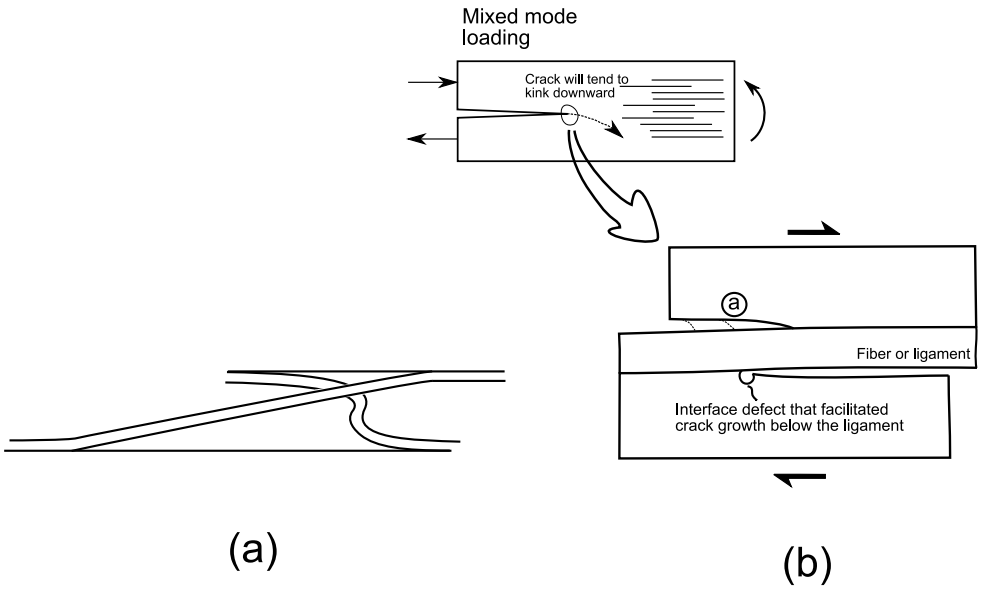

Figure 44: (a) Equal amount of fibers in compression and tension. (b) Mixed mode crack growth promotes the formation of fibers in tension.

ligaments exist, how many thin and what is the spacing between them? Furthermore, the ligaments bridge in two ways with $\beta < 0$ or with $\beta > 0$, see figure 32b. For a mode I crack, symmetry requires that an equal number of fibers tend to cross each way. This will out balance the large tangential forces that arised during a mode I opening.

Under mixed mode conditions the way the ligament bridge is not irrelevant, see figure 44a: The one fiber becomes loaded in tension and the other in compression. The number of ligaments in compression and tension may very well be different, which will influence the effective cohesive law strongly. How many fibers will become loaded in tension and how many in compression is difficult to predict. However, a simple model can help to elucidate the question: Consider the mixed mode specimen in figure 44 where the upper crack has come in from the left. For the imposed loading, the crack will tend to kink downward. The crack tip is not free to kink so it will initially follow the weak upper fiber/matrix interfaces until it passes a point (a) where it becomes preferable for it to switch growth plane. This forms a ligament. The formed ligament will be in tension owing to the global displacement field. The occurrence of a crack that kinks upwards (so it comes in compression) will be unlikely and therefore only few ligaments can be expected in compression. In order to get a more complete understanding of the fiber bridging mechanism under mixed mode conditions, experimental observations would

be helpful. For instance, we must know the distribution ligament thicknesses, their spacing and the orientation (tension or compression).

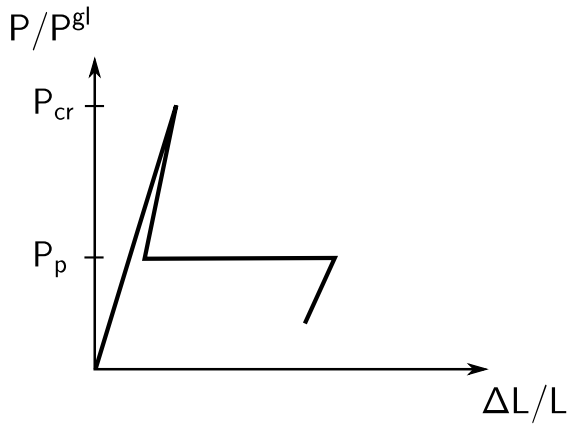

Figure 45: Principal sketch of the collapse behavior of sandwich columns containing debond.

5 Discussion

The present thesis has studied aspects of fracture mechanics in relation to composite structures and materials. In the forthcoming discussion, the main results are interrelated and put into a scientific and practical perspective.

Unstable collapse of sandwich structures

Van Der Neut (1968) has shown that imperfection sensitive and unstable collapses can be expected for elastic thin-walled compression members where local and global buckling can occur near the same external load. This is because the buckling modes interact. In [P3], similar behavior has been observed for a sandwich structure with a debond that can *not* grow (infinite fracture toughness). In this case, buckling of the debonded face sheet interacts with global column buckling. The load-displacement curves show a decrease of the strength after onset of buckling, and therefore, under prescribed load, the structure will become unstable. On the other hand, if the loading is displacement-controlled the response will be stable.

In a more realistic situation, also modeled in [P3], the face sheet/core interface has a finite strength and the debond can grow. The results show that debonds within a critical length interval can cause the sandwich structure to collapse in a highly unstable manner governed by a snap-back mechanism. In practice, such behavior can be very dangerous since after initiation the collapse cannot be stopped irrespective of the type of loading (prescribed force or prescribed displacement). Therefore, this kind of failure must be avoided by any means in high-safety structures.

Reviewing a recent text book on sandwich construction (Zenkert, 1995) it is seen that the proposed design approaches are based entirely on strengths of intact sandwich structures. Together with the present results, this substantiates the concerns raised by Herrmann et al. (2006) that the existing approaches for predicting strength must be improved before sandwich structures should be integrated in high-safety structures such as aircraft primary structures.

A proper design methodology of high-safety structures should include a damage-tolerance analysis. The paper [P3] comprises an important damage-tolerance analysis for sandwich structures since debonds can easily arise. The sketch in figure 45 resembles typical load curves predicted in [P3]. The curve has a maximum value P_{cr} that through a snap-back is reduced to a plateau-load P_p. The study has shown that the maximum strength, P_{cr}, is strongly dependent on geometrical imperfections and the debond length. Therefore, P_{cr} does not represent a reliable strength for the sandwich structure. The plateau-load P_p on the other hand comprises a reliable strength since this will only depend weakly on imperfections and debond length.

Designing more damage tolerant structures

As concluded above, the plateau load, P_p, comprises a reliable strength. Consequently, for a sandwich column optimized for load-bearing capacity, the plateau strength, P_p, should be as high as possible. The study in [P3] has shown that the plateau strength will increase with increasing non-dimensional interface toughness, Γ/HE_f. This was concluded through a parameter study where Γ was varied by increasing the area under the cohesive law (cf. figure 28). The structure parameters: face sheet/core thickness ratio, the slendernes ratio and the elasticity mismatch (see equation 1 in [P3]) were not varied. Therefore, the conclusions of the parameter study are strictly only valid for varying the interface properties while keeping the other parameters constant. We may be able to improve the strength of the sandwich structure by decreasing the face sheet thickness.

In the manufacture process of sandwich structures, an interlayer is normally located between the core and the face sheet. The interlayer is typically strong compared to the core so that debonding will take place in the core which has low fracture toughness. This was for instance the case for the structures tested in [P2]; under mode I dominated loadings they failed in the core. If the interlayer has a lower cohesive law peak stress than the core, $\hat{\sigma}_i < \hat{\sigma}_{core}$, debonding will instead tend to grow in the interlayer, see figure 46.

The interlayer should be tailored so its fracture is characterized by a low

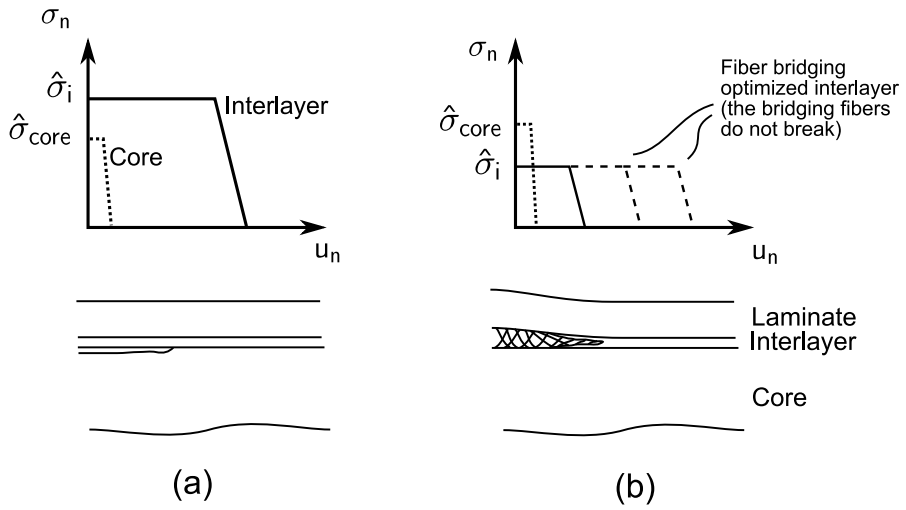

Figure 46: (a) If the cohesive law of the interlayer possesses a higher peak stress $\hat{\sigma}_i$ than the core peak stress $\hat{\sigma}_{core}$ cracking will take place in the core. (b) If $\hat{\sigma}_i < \hat{\sigma}_{core}$ cracking will take place in the interlayer. Furthermore, if the interlayer is designed for failure by fiber bridging substantial toughness increased of the sandwich interface can be seen.

peak stress $\hat{\sigma}_i$ but a large toughness. Here, the main result from the study on fiber bridging becomes useful. The results show that fiber composite laminates can possess very large fracture toughness if they fail by a fiber bridging mechanism. Under normal loading, a bridging fiber will exert bridging forces that attain a steady state level that is retains until fiber fracture. Acting as an interlayer in a sandwich structure, the laminate must have sufficiently weak bondings between fibers and matrix. This will cause the laminate to have a low cohesive peak stress $\hat{\sigma}_i$ and at the same time it will promote extensive fiber bridging where the fibers do not break. The cohesive law for the interlayer shown in 46b is a simple model of the fiber bridging mechanism that only accounts for the plateau stress.

Mixed mode fracture of composites

It is well-known for interfaces of elasto-plastic materials that the fracture toughness can depend significantly on the mode of the loading. Therefore, determination of mode mixity has traditionally taken a central role in detailed specimen analysis. Mixed mode fracture tests of fiber composites also show that the mode of loading has a substantial influence on the fracture resistance curves. The reason for this is currently unresolved. However, I think that the variation of the fracture toughness with mode mixity results mainly from the

fiber bridging mechanism. In section 4.4.5 an initial study on fiber bridging under mixed mode loading conditions was conducted. The study has shown that the behavior of individual fibers has a strong dependence on the mode of the loading. Under mixed mode loadings, fibers that become loaded in tension rapidly exert large tangential bridging stresses whereas fibers loaded in compression rapidly looses their stability and stops contributing to the fracture resistance. A brief analysis of the results shows that under tangential deformation modes the energy dissipation (the area under the cohesive laws) is significant larger than for normal opening of the crack faces.

In future experimental studies useful information could be obtained on composition of the fracture process zone in terms of fiber spacing, ligament (fiber bundles) spacings and thicknesses etc. With this information results like those in figures 42 and 43 could be compiled into average cohesive laws realistic for real composites.

Influence of the mode mixity on face sheet/core debonding of specific sandwich structures was also shown in this thesis. For the sandwich structures tested in [P3] the fracture toughness increased when the crack tip was loaded in dominated mode II. The mechanism behind this change was that the crack growth shifted from propagating in the core to the interlayer which was failing by a tough fiber bridging mechanism.

Mode mixity has a significant influence on several fracture mechanisms. Therefore, a detailed analysis of a mixed mode fracture specimen was carried out. A few findings are briefly discussed in the following.

In [P1], LEFM was applied and the mode mixity for the sandwich specimen was cast in a form where it could be determined analytically apart from a single load-independent phase angle. This phase angle was determined by a numerical method for a wide range of sandwich configurations. Using these results, experimentalists can construct a suiting test setup involving any combination of end normal-forces and end moments and calculate the mode mixity analytically. This is a significant improvement of existing experimental methods where the mode mixity must be calculated (numerically) for each specific test configuration (specimen dimensions, elastic parameters, load combinations) e.g. (Prasad and Carlsson, 1994).

Some essential findings regarding the stress field were discovered: The crack-tip stress field becomes persistent and stretches far away from its source when the face sheet/core stiffness mismatch is large (e.g. $\Sigma < 0.01$). This is probably also why the mode mixity parameter becomes highly dependent on the face sheet/core thickness ratio ($\eta = h/H$); for a certain external loading type ($M = 0$) the mode mixity changes more than 50° by changing η ($= h/H$) from 0.2 to 10, see figure 14 at $\Sigma \approx 0.01$. The crack-tip stress field

also stretches in the length-direction of the sandwich structure. Therefore, if the sandwich length is too short, non-uniform stresses will exists along the specimen ends. A consequence of this is that the analytical J integral calculations used in this thesis become invalid since they are derived for uniform stress distributions along the specimen ends.

The analysis in [P1] is only valid for sandwich structures loaded by moments and normal forces. The moment should not be created by a transverse force since this has not been accounted for in the model. This restriction puts limitations on the practical applicability of the results since for most practical problems loadings will include transverse forces.

Linear elastic fracture mechanics versus cohesive zone modeling

The thesis comprises studies that apply linear elastic fracture mechanics (LEFM) and cohesive zone modeling (CZM) for modeling fracture of composite materials and structures. In the introductory sections both theories were discussed and their theoretical framework was setup. Both LEFM and CZM are well-established theories for fracture and they have been applied in numerous articles. LEFM is based on the premise that the extent of the fracture process zone must be small compared to the specimen proportions. In the introduction, this aspect was thoroughly reviewed based on two examples. These showed that when fiber bridging is an active mechanism, LEFM is only valid for unrealistic large specimens. From a practical point of view, using LEFM for structures that fail by large scale bridging mechanisms can be disastrous since LEFM predictions will be non-conservative.

6 Conclusion

The present thesis has treated various aspects of interface fracture in composite materials and structures. The studies include both experimental, theoretical and numerical results.

A comprehensive analysis of a sandwich specimen end normal-forces and end moments was conducted within the frames of linear elastic fracture mechanics (LEFM). Using the obtained results, mode mixity for many sandwich configurations can be calculated. The results show that for typical sandwich structures the local crack tip stress field is highly dependent of specimen geometry. Fracture toughness of two types of sandwich structures was measured experimentally and was found to be in the range $270\,J/m^2$ to $2000\,J/m^2$ depending on the actual material combinations and the mode of loading. The highest fracture toughness was obtained under dominated shear loading of

the crack tip which resulted in formation of fiber bridging.

Numerical modeling of the collapse of partially debonded sandwich columns predicted pronounced imperfection sensitivity. It was concluded that design approaches for sandwich constructions should include a damage-tolerance-analysis against debonds. Fiber bridging response in the form of composite cohesive laws was predicted and the results show that composites with arbitrary fracture toughness can potentially be manufactured. However, this relies heavily on survival of the fibers in the fiber bridging zone.

References

H.G. Allen. *Analysis and design of structural sandwich panels.* Pergamon, Oxford, 1969.

G. Bao and Z. Suo. Remarks on crack-bridging concepts. *Applied Mechanical Review*, 45(8):355–366, 1992b.

G. Bao, S. Ho, Z. Suo, and B. Fan. The role of material orthortopy in fracture specimens for composites. *International Journal of solids and structures*, 29(9):1105–1116, 1992.

G.I. Barenblatt. The formation of equilibrium cracks during brittle fracture. general ideas and hypotheses. axially-symmetric cracks. *Journal of Applied Mathematics and Mechanics*, 23(3):622–636, 1959.

J.L. Beuth. Separation of crack extension modes in orthotropic delamination modes. *International journal of fracture*, 77:305–321, 1996.

B.A. Bilby, A.H. Cottrell, and K.H. Swinden. Spread of plastic yield from notch. *Royal Society – Proceedings Series A*, 272(1350):304–314, 1963.

D.B. Bogy. Two edge-bonded elastic wedges of different materials and wedge angles under surface tractions. *Journal of applied mechanics*, 38(2):377–386, 1971.

D. Broek. *Elementary engineering fracture mechanics.* Martinus Nijhoff Publishers, 1986.

P. Brøndsted, H. Lilholt, and A. Lystrup. Composite materials for wind turbine blades. *Annual review of materials research*, 35:505–538, 2005.

D.O. Brush and B.O. Almroth. *Buckling of bars, plates, and shells.* McGraw-Hill Book Company, New York, 1975.

B. Budiansky, A.G. Evans, and J.W. Hutchinson. Fiber-matrix debonding effects oncracking in aligned fiber ceramic composites. *International Journal of Solids and Structures*, 32(3-4):315–328, 1995.

H.C. Cao and A.G. Evans. An experimental study of the fracture resistance of bimaterial interfaces. *Mechanics of Materials*, 7(4):295–304, 1989.

L.A. Carlsson, R.C. Matteson, F. Aviles, and D.C. Loup. Crack path in foam cored dcb sandwich fracture specimens. *Composites Science and Technology*, 65(15-16):2612–2621, 2005.

P.G. Charalambides and W. Zhang. An energy method for calculating the stress intensities in orthotropic bimaterial fracture. *International journal of fracture*, 76:97–120, 1996.

B.N. Cox and D.B. Marshall. Concepts for bridged cracks in fracture and fatigue. *Acta Metallurgica et Materialia*, 42(2):341–363, 1994.

J. Drews, S. Goutianos, P. Kingshott, S. Hvilsted, N. Rozlosnik, K. Almdal, and B. F. Sørensen. Plasma polymerized thin films of maleic anhydride and 1,2- methylenedioxybenzene for improving adhesion to carbon surfaces. *Journal of Vacuum Science and Technology A: Vacuum, Surfaces and Films*, 25(4):1108–1117, 2007.

D.S. Dugdale. Yielding of steel sheets containing slits. *Journal of the Mechanics and Physics of Solids*, 8(2):100–104, 1960.

J. Dundurs. Edge-bonded dissimilar orthogonal elastic wedges under normal and shear loading. *Journal of applied mechanics*, 36:650–652, 1969.

S. Feih, J. Wei, P. Kingshott, and B.F. Sorensen. The influence of fibre sizing on the strength and fracture toughness of glass fibre composites. *Composites Part A: Applied Science and Manufacturing (Incorporating Composites and Composites Manufacturing)*, 36(2):245–255, 2005.

R. Ferguson. Full scale composite testing at auk. In *Composites testing and model identification*. University of Bristol, 2004.

N.A. Fleck and I. Sridhar. End compression of sandwich columns. *Composites Part A: Applied Science and Manufacturing (Incorporating Composites and Composites Manufacturing)*, 33(3):353–359, 2002.

R.M.L. Foote, Y.W. Mai, and B. Cotterell. Crack growth resistance curves in strain-softening materials. *Journal of the Mechanics and Physics of Solids*, 34(6):593–607, 1986.

Y. Frostig. Buckling of sandwich panels with a flexible core-high-order theory. *International Journal of Solids and Structures*, 35(3-4):183–204, 1998.

S.L. Gao and E. Mader. Characterisation of interphase nanoscale property variations in glass fibre reinforced polypropylene and epoxy resin composites. *Composites Part A: Applied Science and Manufacturing (Incorporating Composites and Composites Manufacturing)*, 33(4):559–576, 2002.

A.A. Griffith. The phenomena of rupture and flow in solids. *Royal Society of London – Philosophical Transactions*, 221:163–198, 1920.

S. Hashemi, A.J. Kinloch, and J.G. Williams. The analysis of interlaminar fracture in uniaxial fibre-polymer composites. *Proceedings of the Royal Society of London, Series A (Mathematical and Physical Sciences)*, 427 (1872):173–199, 1990.

M.Y. He and J.W. Hutchinson. Kinking of a crack out of an interface. *Journal of Applied Mechanics, Transactions ASME*, 56(2):270–278, 1989.

A.S. Herrmann, C.Z. Zahlen, and I. Zuardy. Sandwich structures technology in commcial aviation - present applications and future trend. In *Sandwich structures 7: Advancing with sandwich structures and materials*, pages 13–26. Aalborg University, 2006.

G.W. Hunt, L.S. Da Silva, and G.M.E. Manzocchi. Interactive buckling in sandwich structures. *Proceedings of The Royal Society of London, Series A: Mathematical and Physical Sciences*, 417(1852):155–177, 1988.

J.W. Hutchinson. Kinking of a crack out of an interface. *Transactions of the ASME. Journal of Applied Mechanics*, 56(2):270–8, 1989.

J.W. Hutchinson and H.M. Jensen. Models of fiber debonding and pullout in brittle composites with friction. *Mechanics of Materials*, 9(2):139–163, 1990.

J.W. Hutchinson and Z. Suo. Mixed-mode cracking in layered materials. *Advances in Applied Mechanics*, 19:63–191, 1992.

C.E. Inglis. Stresses in a plate due to the presence of cracks and sharp corners. *Transactions of the institute of naval architects*, 55:219–241, 1913.

G.R. Irwin and J.A. Kies. Fracturing and fracture dynamics. *Welding Journal*, 31(2):95s–100s, 1952.

T.K. Jacobsen and B.F. Sørensen. Mode i intra-laminar crack growth in composites - modelling of r-curves from measured bridging laws. *Composites Part A: Applied Science and Manufacturing (Incorporating Composites and Composites Manufacturing)*, 32(1):1–11, 2001.

S. Jeelani, L. Carlsson, M. Saha, S. Islam, and H. Mahfuz. Buckling of sandwich composites; effects of coreskin debonding and core density. *Applied Composite Materials*, 12(2):73–91, 2005.

R.M. Jones. *Mechanics of composite materials.* McGraw-Hill, New York, 1975.

K. Karbaek and H. Lilholt. *Materialekendskab - Plast of fibre.* Sekreteriatet for efteruddannelse i Materialeteknologi, Dansk teknologisk institut, Taastrup, 1993.

D.A.W. Kaute, H.R. Shercliff, and M.F. Ashby. Delamination, fibre bridging and toughness of ceramic matrix composites. *Acta Metallurgica Et Materialia*, 41(7):1959–1970, 1993.

S. Kim and S. Sridharan. Analytical study of bifurcation and nonlinear behavior of sandwich columns. *Journal of Engineering Mechanics*, 131 (12):1313–1321, 2005.

Y.W. Kwon and S.H. Yoon. Compressive failure of carbon-foam sandwich composites with holes and/or partial delamination. *Composite Structures*, 38(1-4):573–580, 1997.

S.G. Lekhnitskii. *Theory of elasticity of anisotropic elastic body.* Mir Publisher, Moscow, 1981.

S. Li, J. Wang, and M.D. Thouless. The effects of shear on delamination in layered materials. *Journal of the Mechanics and Physics of Solids*, 52(1): 193–214, 2004.

S. Li, M.D. Thouless, A.M. Waas, J.A. Schroeder, and P.D. Zavattieri. Use of a cohesive-zone model to analyze the fracture of a fiber-reinforced polymer-matrix composite. *Composites Science and Technology*, 65(3-4):537–549, 2005.

K.M. Liechti and Y.S. Chai. Asymmetric shielding in interfacial fracture under in-plane shear. *Transactions of the ASME. Journal of Applied Mechanics*, 59(2):295–304, 1992.

B.M. Malyshev and R.L. Salganik. Strength of adhesive joints using theory of cracks. *International Journal of Fracture Mechanics*, 1(2):114–128, 1965.

D.B. Marshall, B.N. Cox, and A.G. Evans. The mechanics of matrix cracking in brittle-matrix fiber composites. *Acta Metallurgica*, 33(11):2013–2021, 1985.

P.P.L. Matos, R.M. McMeeking, P.G. Charalamambides, and M.D. Drory. A method for calculating stress intensities in bimaterial fracture. *International Journal of Fracture*, 40:945–970, 1989.

S. Nakamura, E. Pavlovic, and E.J. Kramer. Fracture energy of epoxy interfaces with layers of different silane coupling agents. *Journal of Adhesion*, 83(4):351–365, 2007.

M.O. Nandy, N. Tohyama, B.N. Kim, M. Enoki, S. Schmauder, and T. Kishi. Finite element method simulation of transverse bridging in fiber reinforced composites. *Journal of the Ceramic Society of Japan*, 106(10):968–973, 1998.

A. Needleman. Continuum model for void nucleation by inclusion debonding. *American Society of Mechanical Engineers (Paper)*, 1987.

E. Orowan. Fracture and strength of solids. *Reports on Progress in Physics*, 12, 1948.

S. Prasad and L.A. Carlsson. Debonding and crack kinking in foam core sandwich beams. i. analysis of fracture specimens. *Engineering Fracture Mechanics*, 47(6):813–824, 1994.

J. Ratcliffe and W.J. Cantwell. Center notch flexure sandwich geometry for characterizing skin-core adhesion in thin-skinned sandwich structures. *Journal of Reinforced Plastics and Composites*, 20(11):945–970, 2001.

J. J. C. Remmers, R. de Borst, and A. Needleman. A cohesive segments method for the simulation of crack growth. *Computational Mechanics*, 31 (1-2):69–77, 2003.

J.R. Rice. Path independent integral and approximate analysis of strain concentration by notches and cracks. *American Society of Mechanical Engineers, Papers*, 1968.

J.R. Rice. Elastic fracture mechanics concepts for interfacial cracks. *Transactions of the ASME. Journal of Applied Mechanics*, 55(1):98–103, 1988.

J.R. Rice, Z. Suo, and J.S. Wang. Mechanics and thermodynamics of brittle interfacial failure in bimaterial systems. *"Metal-Ceramics Interfaces", Acta-Scripta Metallurgica Proceedings Series, Pergamon press*, 4:169–194, 1990.

E.F. Rybicki and M.F. Kanninen. A finite element calculation of stress intensity factors by a modifyed crack closure integral. *Engineering fracture mechanics*, 9:931–938, 1977.

G.C. Sih, P.C. Paris, and F. Erdogan. Crack-tip, stress-intensity factors for plane extension and plate bending problems. *American Society of Mechanical Engineers – Papers*, 1961.

B.F. Sørensen and T.K. Jacobsen. Crack growth in composites. applicability of r-curves and bridging laws. *Plastics, Rubber and Composites*, 29(3): 119–133, 2000.

B.F. Sørensen and T.K. Jacobsen. Determination of cohesive laws by the j integral approach. *Engineering Fracture Mechanics*, 70(14):1841–58, 2003.

B.F. Sørensen and Torben K Jacobsen. Large-scale bridging in composites: R-curves and bridging laws. *Composites - Part A - Applied Science and Manufacturing*, 29(11):1443, 1998.

B.F. Sørensen and P. Kirkegaard. Determination of mixed mode cohesive laws. *Engineering Fracture Mechanics*, 73(17):2642–2661, 2006.

B.F. Sørensen, K. Jørgensen, T.K. Jacobsen, and R.C. Østergaard. Dcb-specimen loaded with uneven bending moments. *International Journal of Fracture*, 141(1):163–176, 2006.

B.F. Sørensen, K. Gamstedt, S. Goutianos, and R.C. Østergaard. *Mech. of matr., Submitted*, 2007.

S.M. Spearing and A.G. Evans. The role of fiber bridging in the delamination resistance of fiber-reinforced composites. *Acta Metallurgica Et Materialia*, 40(9):2191–2199, 1992.

Z. Suo. Singularities, interfaces and cracks in dissimilar anisotropic media. *Proceedings of the Royal Society of London, Series A (Mathematical and Physical Sciences)*, 427(1873):331–358, 1989.

Z. Suo and J.W. Hutchinson. Sandwich test specimens for measuring interface crack toughness. *Materials Science amp; Engineering A: Structural*

Materials: Properties, Microstructure and Processing, A107(1):135–143, 1989.

Z Suo and JW Hutchinson. Interface crack between two elastic layers. *International Journal of Fracture*, 43(1):1–18, 1990.

Z. Suo, G. Bao, B. Fan, and Wang T.C. Orthotropy rescaling and implication for fracture in composites. *International Journal of solids and structures*, 28(2):235–248, 1991.

Paris P.C. Irwin G.C. Tada, H. *The stress analysis of cracks handbook*. Paris Productions Inc, St Louis, Miss., 1985.

O. T. Thomsen. Polymer composites materials for wind power turbines. In *Proceedings of the 27th Risø International Symposium on Materials Science*, pages 97–114. Risø, Danish National Laboratory, 2006.

H. Toftegaard and S. Goutianos. Composite skin elastic constants from monolithic in-plane specimens and bonded out-of-plane specimens. *Journal of sandwich structures and materials*, 9:239–259, 2007.

V. Tvergaard. Effect of thickness inhomogeneities in internally pressurized elastic-plastic spherical shells. *Journal of the Mechanics and Physics of Solids*, 24(5):291–304, 1976.

V. Tvergaard. Effect of fibre debonding in a whisker-reinforced metal. *Materials Science and Engineering: A*, 125(2):203–213, 1990.

V. Tvergaard and J.W. Hutchinson. The relation between crack growth resistance and fracture process parameters in elastic-plastic solids. *Journal of the Mechanics and Physics of Solids*, 40(6):1377–1397, 1992.

V. Tvergaard and J.W. Hutchinson. The influence of plasticity on mixed mode interface toughness. *Journal of the Mechanics and Physics of Solids*, 41(6):1119–1135, 1993.

V. Tvergaard and J.W. Hutchinson. Effect of strain dependent cohesive zone model on predictions of interface crack growth. *Journal De Physique. IV : JP*, 6(6), 1996.

V. Vadakke and L.A. Carlsson. Experimental investigation of compression failure of sandwich specimens with face/core debond. *Composites Part B: Engineering*, 35(6-8):583–590, 2004.

A. Van Der Neut. The interaction of local buckling and column failure of thin-walled compression members. *In proceeding of the 12th International Congress on Applied Mechanics*, 1968.

M.A.M. Wadee. Localized buckling in sandwich struts with pre-existing delaminations and geometrical imperfections. *Journal of the Mechanics and Physics of Solids*, 50(8):1767–1787, 2002.

J.S. Wang and Z. Suo. Experimental determination of interfacial toughness curves using brazil-nut-sandwiches. *Acta Metall. Mater.*, 38:1279–90, 1990.

J.M. Whitney. Experimental characterization of delamination fracture. *Interlaminar response of composite materials*, pages 161–250, 1989.

M.L. Williams. The stresses around a fault or crack in dissimilar media. *Bulletin of the Seismological Society of America*, 49:199–204, 1959.

Q. Yang and B. Cox. Cohesive models for damage evolution in laminated composites. *International Journal of Fracture*, 133:107–137, 2005.

D. Zenkert. *An introduction to sandwich construction.* Engineering Materials Advisory Services LTD., London, 1995.

D. Zenkert and A. Shipsha. Compression-after-impact strength of sandwich panels with core crushing damage. *Applied Composite Materials*, 12(3-4): 149–164, 2005.

[P1]

International Journal of Fracture, **143**(4), p. 301-316.

Int J Fract (2007) 143:301–316
DOI 10.1007/s10704-007-9059-4

ORIGINAL PAPER

Interface crack in sandwich specimen

Rasmus C. Østergaard · Bent F. Sørensen

Received: 30 August 2006 / Accepted: 13 February 2007 / Published online: 8 May 2007

Abstract Fracture of a sandwich specimen loaded with axial forces and bending moments is analyzed in the context of linear elastic fracture mechanics. A closed form expression for the energy release rate for interface cracking of a sandwich specimen with isotropic face sheets is found from analytical evaluation of the J-integral. An approach is applied, whereby the mode mixity for any combination of the loads can be calculated analytically when a load-independent phase angle has been determined. This load-independent phase angle is determined for a broad range of sandwich configurations of practical interest. The load-independent phase angle is determined using a novel finite element based method called the crack surface displacement extrapolation method.

The expression for the energy release rate is based on the J-integral and certain stress distributions along the ends of the sandwich specimen. When the stresses from the crack tip interacts with the stresses at the ends, the present analytical calculation of the J-integral becomes inaccurate. The results show that for the analytically J-integral to be accurate the crack tip must be a certain distance away from the uncracked end of the specimen. For a sandwich specimen with face sheet/core stiffness ratio of 100, this distance is in the order 10 times the face sheet thickness. For sandwich structures with face sheet/core stiffness ratio of 1,000, the distance is 30 times the face sheet thickness.

Keywords Energy release rate · Mode mixity · Delamination · Adhesive joints

R. C. Østergaard (✉) · B. F. Sørensen
Material Research Department, Risø National Laboratory, Technical University of Denmark, Frederiksborgvej 399, 4000 Roskilde, Denmark
e-mail: rasmus.c.oestergaard@risoe.dk

1 Introduction

Sandwich structures find their applications as structural load bearing components in many areas. Structures such as wind turbine blades, boats and aeronautical structures are examples where sandwich structures are used for load bearing purposes. For these structures, the structural integrity is of major importance and under the presence of imperfections the load bearing capacity can be reduced significantly.

A sandwich structure is a three-layer structure comprising a low density and low modulus core material between two high modulus face sheets. The core mainly acts as a spacer keeping the face sheets spaced apart and has a thickness 2–10 times the face sheet thickness. This arrangement provides a structure with a high bending stiffness (Zenkert 1995). Sandwich structures are not the only type of three-layer structures. Another common type of multilayers consisting of three layers is adhesive joints. Adhesive joints serve as a mean to hold components together and transfer stresses between them. The adhesive is typically a polymer material and the adherents can be any solid that is appropriate for adhesion (Kinloch 1987). In adhesive

joints, the thickness of the adhesive is typically much smaller than the thickness of the adherents. In the present study we study delamination of three-layer specimens. The results are applicable for both sandwich structures and adhesive joints.

For sandwich structures, debonds (areas between the face sheet and core with no adhesion) constitute an important damage type that can lead to debonding crack growth, i.e. crack growth in the interface between face sheets and core. Interface cracking is generally mixed mode cracking, i.e. both normal and shear stresses develop just ahead of the crack tip (Williams 1959; Rice 1988). Experiments have shown that the fracture energy can depend on the mode mixity (Cao and Evans 1989; Wang and Suo 1990; Liechti and Chai 1992). Consequently, a complete analysis requires the determination of both the energy release rate and the mode mixity.

Earlier work on sandwich structure fracture specimens include Carlsson and Prasad (1993) and Prasad and Carlsson (1994) who analyzed sandwich configurations where one face sheet was loaded by a combined axial/transverse edge load and the other face sheet was fixed on a rigid plane. The mode mixity was determined by numerical means for each sandwich and each load situation. Several other sandwich specimens also exist. For instance, the three point bend geometry and the center notch flexure geometry (Ratcliffe and Cantwell 2001; Cantwell et al. 2000), however these specimens does not allow for varying the mode mixity through the loading. Østergaard et al. (2007) carried out experimental measurements of interface fracture toughness of sandwich structures and found that the mode mixity has a significant influence on the fracture mechanism and the fracture toughness. Suo and Hutchinson (1989) analyzed sandwich specimens with core layer thickness much smaller than the face sheet layers. They found that for moderate stiffness mismatch, the difference in the mode mixity of the sandwich and the homogeneous specimen (i.e. without the thin core layer) was relatively small. However, the difference increased as the stiffness ratio between the two layers became large. Fleck et al. (1991) and Akisanya and Fleck (1992) analyzed a sandwich with a small core thickness and showed that under some conditions the crack jumps between the interfaces resulting in a wavy crack path. This phenomenon was also observed in experiments.

The problem that we analyze in the present paper is interfacial cracking of a symmetric sandwich specimen. The specimen geometry is fairly general and can represent a number of problems of great practical importance, such as adhesive joints and sandwich structures. Our analysis is performed within the framework of linear elastic fracture mechanics and comprises calculation of energy release rate and mode mixity. For sufficiently long specimens the energy release rate and the mode mixity attain steady-state values. We calculate these steady-state values as function of loading, the thickness and stiffness parameters. Emphasis will be given to cases where the face sheets are much stiffer than the core, since this is often the case in sandwich structures. An analysis will quantify how long the specimen must be before the mode mixity and energy release rate attain steady-state values.

The present paper is organized as follows. First, we will specify the problem. Next we give a short summary of fracture mechanics for cracks along the interface between two elastic dissimilar materials. Then, we analyze the problem shown in Fig. 1, recasting it as a reduced problem that is solved in terms of energy release rate, G, and mode mixity, ψ. The solution is analytical apart from one load-independent parameter, ω, which is found by numerical means. Hereafter follows an investigation regarding the influence of length of the specimen on the validity of the presented equations. Then follows an application example. Finally, major results are summarized.

First, the problem is defined. We analyze a unit width sandwich specimen of length L with and a crack of length a starting at $x_1 = -a$, $x_2 = 0$ (see Fig. 1). The face sheets have the same thickness, H, and the thickness of the core is denoted h. The sandwich specimen is loaded along its edges by moments pr. unit width M_k, $k = 1, 2, 3$ and by forces pr. unit width P_k, $k = 1, 2, 3$. In the first part of the analysis $a/H \gg 1$ and $L/(2H + h) \gg 1$ so that the crack tip is remote from the ends of the specimen. Under these conditions, the energy release rate and mode mixity attain steady-state values.

2 Mechanics of interface cracks

Each of the materials in the sandwich specimen are taken to be isotropic and linear elastic. Let the elastic

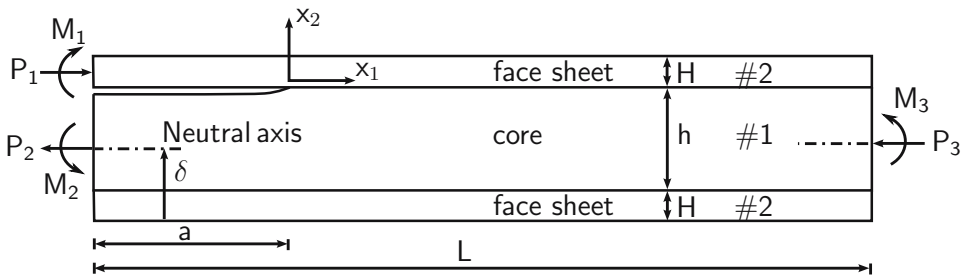

Fig. 1 Interface cracking of a sandwich specimen with equal thickness face sheets is analyzed. Material numbers are shown

properties of the materials be given by the shear modulus μ_m and the Poisson's ratio ν_m, where subscript m takes the value 1 for the core and 2 for the face sheets. As shown by Dundurs (1967, 1969) under certain restrictions the stress field in a two-dimensional bimaterial body depends only on two non-dimensional combinations of the elastic moduli. Defining $\kappa_m = 3 - 4\nu_m$ for plane strain and $\kappa_m = (3 - \nu_m)/(1 + \nu_m)$ for plane stress, the Dundurs parameters can be expressed as

$$\alpha = \frac{\mu_1(\kappa_2 + 1) - \mu_2(\kappa_1 + 1)}{\mu_1(\kappa_2 + 1) + \mu_2(\kappa_1 + 1)} \text{ and}$$

$$\beta = \frac{\mu_1(\kappa_2 - 1) - \mu_2(\kappa_1 - 1)}{\mu_1(\kappa_2 + 1) + \mu_2(\kappa_1 + 1)}. \tag{1}$$

Alternatively, α can also be expressed as

$$\alpha = \frac{\Sigma - 1}{\Sigma + 1}, \tag{2}$$

where Σ is the ratio between the Young's modulus for the core and the face sheets, respectively

$$\Sigma = \bar{E}_1/\bar{E}_2, \tag{3}$$

where $\bar{E}_m = E_m$ for plane stress and $\bar{E}_m = E_m/(1 - \nu_m^2)$ for plane strain. Here, E_m denotes the Young's modulus of material number m. In some of the results in the present work α will be used and in other results Σ will be used.

Just ahead of the crack tip ($\theta = 0°$, see Fig. 2) the stresses are dominated by a singular stress field of the form (Rice 1988):

$$\sigma_{22} + \mathrm{i}\sigma_{12} = \frac{1}{\sqrt{2\pi}} K r^{\mathrm{i}\epsilon - 1/2}, \tag{4}$$

where $K = K_1 + \mathrm{i}K_2$ is the complex stress intensity factor, $\mathrm{i} = \sqrt{-1}$, r is the radial distance along the x_1-axis and ϵ is the oscillatory parameter given as

$$\epsilon = \frac{1}{2\pi} \ln\left(\frac{1 - \beta}{1 + \beta}\right).$$

The crack opening components Δu_n are defined from the displacements u_n of two material points coinciding in the un-deformed state

$$\Delta u_n = u_n(r, \theta = 90°) - u_n(r, \theta = -90°),$$

where n takes the values 1 and 2, that refers to the direction in the coordinate system in Fig. 2. The crack opening components are related to the complex stress intensity factor, K, through

$$\Delta u_2 + \mathrm{i}\Delta u_1 = \frac{c_1 + c_2}{2\sqrt{2\pi}(1 + 2\mathrm{i}\epsilon)\cosh(\pi\epsilon)} K r^{\mathrm{i}\epsilon + 1/2}, \tag{5}$$

where

$$c_m = \frac{\kappa_m + 1}{\mu_m}.$$

Note that (5) predicts interpenetration of crack faces close to the crack tip. However, as discussed elsewhere (Rice 1988), the contact zone is usually small and can be neglected. The energy release rate can be related to the complex stress intensity factor through (Rice 1988):

$$G = \frac{c_1 + c_2}{16\cosh^2(\pi\epsilon)} |K|^2 \tag{6}$$

and here $|K|$ is the modulus of K.

For an interface problem the mode mixity is defined as the phase angle of $K l^{\mathrm{i}\epsilon}$

$$\psi = \tan^{-1}\left[\frac{\Im(K l^{\mathrm{i}\epsilon})}{\Re(K l^{\mathrm{i}\epsilon})}\right], \tag{7}$$

where l is an arbitrary chosen length parameter and $\Im$, $\Re$ denote the imaginary and real parts, respectively. In the forthcoming analysis the parameter l is set equal to the thickness of the core, h.

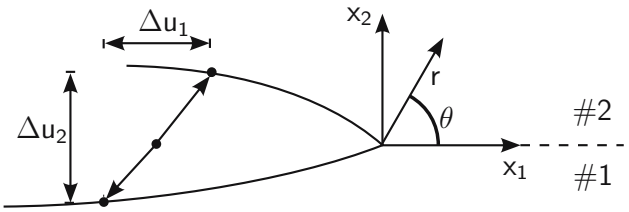

Fig. 2 Definition of crack face opening components

3 Analysis

3.1 The reduced problem

We now turn towards the specific problem outlined in Fig. 1. We wish to determine energy release rate, G, and mode mixity, ψ, as function of the load, geometry and stiffness parameters. The crack-tip is assumed to be remote from the ends, i.e. $L/(2H+h) \gg 1$ and $a/H \gg 1$, whereby we ensure that the stresses at the ends are uniform (independent of x_1). Then, G and ψ are independent of a and L. Later, in Sect. 4.4, we determine specific conditions under which G and ψ are independent of a and L.

Following the procedure by Suo and Hutchinson (1990) we transform the general load situation to a reduced problem. First, by static moment and force equilibrium requirements, it is clear that two of the six loads are static determined. For instance, we can express P_2 and M_2 by P_1, M_1, P_3 and M_3 as follows

$$P_2 = P_1 - P_3$$

and

$$M_2 = P_1\left(\frac{3H}{2} - h - \delta\right) - P_3\left(H + \frac{h}{2} - \delta\right) + M_1 - M_3,$$

where δ is the distance from the bottom of the bilayer beam to the neutral axis.

Next, we recognize that the crack tip stress field of the original problem contains stress singularities in the stress components σ_{22} and σ_{12}. Then, we notice that the stress field of the intact sandwich specimen (Fig. 3b) only contains stress components parallel to the crack (only $\sigma_{11} \neq 0$ under plane stress and only $\sigma_{11} \neq 0$ and $\sigma_{33} \neq 0$ under plane strain). Therefore, we can superimpose the stress field of the intact sandwich specimen (Fig. 3b) to the stress field of the original problem without altering the stress components σ_{22} and σ_{12}. Thus, the stress components σ_{22} and σ_{12} of the reduced problem (Fig. 3c) are identical to that of the original problem (Fig. 3a). It follows that the stress singularity at the crack tip of the original problem depends only on the load parameters P and M of the reduced problem:

$$\begin{aligned} P &= P_1 - \int_0^H \sigma_{11}(x_2)\mathrm{d}x_2 \\ M &= M_1 - \int_0^H \sigma_{11}(x_2)\left(x_2 - \frac{H}{2}\right)\mathrm{d}x_2 \end{aligned} \tag{8}$$

where the stress $\sigma_{11}(x_2)$ is obtained from Hooke's law in material #2 $\sigma_{11} = \bar{E}_2\epsilon_{11,3}$, where $\epsilon_{11,3}$ denotes the ϵ_{11} strain in the uncracked beam end. The strain distribution in the ends of the specimen is given in Appendix A. Calculating the integrals in (8) we get

$$\begin{aligned} P &= -P_1 + C_1 P_3 + C_2 M_3/h \\ M &= -M_1 + C_3 M_3, \end{aligned} \tag{9}$$

where C_1, C_2 and C_3 are dimensionless constants that depend on the stiffness parameter Σ and the thickness ratio

$$\eta = h/H. \tag{10}$$

The C's are given by

$$C_1 = \frac{1}{A_3\eta},\ C_2 = \frac{1}{2I_3}\left(\frac{1}{\eta} + \frac{1}{\eta^2}\right) \text{ and } C_3 = \frac{1}{12I_3\eta^3},$$

where A_3 and I_3 are given in Appendix A.

Equilibrium is obtained with a reacting moment (see Fig. 3c):

$$M^* = P\left(\frac{3H}{2} + h - \delta\right) = Ph\chi + M,$$

where $\chi = \frac{3}{2\eta} + 1 - \Delta$ and

$$\Delta = \delta/h = \frac{1 + 2\Sigma\eta + \Sigma\eta^2}{2\eta(1+\Sigma\eta)}.$$

3.2 Analysis of the reduced problem

The reduced problem is specified in terms of six parameters, P, M, H, η, Σ and β. It is possible, by the use of

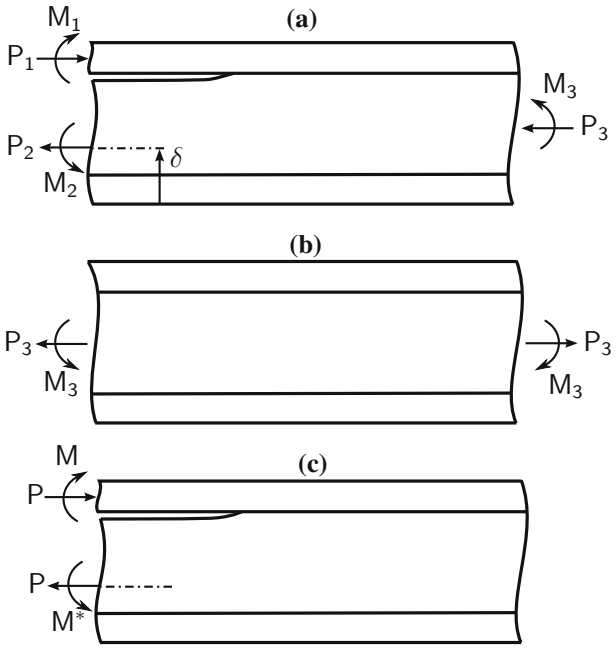

Fig. 3 By superimposing the stress field in (**b**) on the stress field of the original problem (**a**) the stress field of a reduced problem (**c**) is obtained

linearity and dimensionality arguments as those used by Thouless et al. (1987) on a homogeneous specimen, to express the dependency of most parameters analytically. First, we note that, in accordance with (6), the complex stress intensity factor must have the SI units $Pa\,m^{\frac{1}{2}-i\epsilon}$. Furthermore, since the model is made within linear elasticity, the stress intensity factors can be written as a linear combination of P/H and M/H^2,

$$K = K_1 + iK_2 = \left[\frac{P}{H}z_1 + \frac{M}{H^2}z_1\right] H^{1/2-i\epsilon}, \qquad (11)$$

where z_1 and z_2 are (presently unknown) non-dimensional complex numbers that depend on Σ (or α), β and η, but not on P, M and H.

It turns out to be convenient to write z_1 and z_2 in polar form

$$z_1 = \frac{e^{i\omega}}{\sqrt{U}} \quad \text{and} \quad z_2 = \frac{ie^{(\omega+\gamma)}}{\sqrt{V}}, \qquad (12)$$

where ω and γ are phase angles and $1/\sqrt{U}$ and $1/\sqrt{V}$ are the magnitude of z_1 and z_2, respectively. Then, the complex stress intensity factor can be written as

$$K = P\frac{e^{i\omega}}{\sqrt{U}}H^{-1/2-i\epsilon} + M\frac{e^{i(\omega+\gamma)}}{\sqrt{V}}H^{-3/2-i\epsilon}, \qquad (13)$$

where ω, γ, U and V are non-dimensional parameters that depend on Σ, β and η but not on P and M.

Three of the four unknown non-dimensional parameters can be determined analytically by analyzing three different load combinations. First, G is calculated by the J-integral along the external boundaries of the specimen with $P \neq 0$ and $M = 0$ using the strain distributions given in Appendix A. The result is

$$G = \frac{1}{2\bar{E}_2}\frac{P^2}{h}\left\{\frac{1}{A_1} + \frac{1}{A_2} + \frac{\chi^2}{I_2}\right\}, \qquad (14)$$

where A_1, A_2 and I_2 are constants given in Appendix A.

With $P \neq 0$ and $M = 0$, K from (13) becomes

$$K_1 + iK_2 = \frac{P}{H^{1/2}\sqrt{U}}e^{i(\omega-\epsilon\ln H)}, \qquad (15)$$

so that

$$|K|^2 = K\bar{K} = \frac{P^2}{HU}$$

Inserting $|K^2|$ into (6) gives G. Setting this equation for G equal to (14) gives U according to

$$\frac{1}{U} = \frac{1}{A_2} + \frac{1}{A_1} + \frac{\chi^2}{I_2}.$$

Next, following the same procedure for a load combination with $P = 0$ and $M \neq 0$ gives V as

$$\frac{1}{V} = \frac{1}{I_2} + \frac{1}{I_1}.$$

Finally, the energy release rate for any combination of P and M can be written as

$$G = \frac{c_2}{16}\left(\frac{P^2}{hU} + \frac{M^2}{h^3V} + 2\frac{PM}{\sqrt{UV}h^2}\sin\gamma\right), \qquad (16)$$

where

$$\sin\gamma = \frac{\chi}{I_2}\sqrt{UV}.$$

In Eq. (13) the only remaining unknown parameter is the phase angel ω. The load-independent phase angle ω depends on the material parameters (Σ and β) and the geometry (η) but not on the load parameters P and M.

In the general, case ω must be determined by numerical means. In the present work, ω is determined using a novel method called Crack Surface Displacement Extrapolation (CSDE) method. The method calculates mode mixity based on crack opening components found with the Finite Element Method (FEM). The CSDE method, which is described in detail in Appendix B, has also been implemented in a parallel study (Berggren et al. 2007).

Once $\omega(\Sigma, \beta, \eta)$ is determined, the singularity at the crack tip is characterized in terms of K. However, from an experimental point of view, a more practical measure of the singularity is comprised by the energy release rate, G, together with the mode mixity, ψ, that is related to K via (7). Combining (5), (6), (7) and (16), while setting $l = h$, the mode mixity is expressed as

$$\psi = \tan^{-1}\left[\frac{\lambda\,\sin\,\omega - \cos(\omega+\gamma)}{\lambda\,\cos\,\omega + \sin(\omega+\gamma)}\right], \quad \text{for } M \neq 0, \tag{17}$$

$$\psi = \omega, \quad \text{for } M = 0,$$

where λ is a non-dimensional load parameter

$$\lambda = \sqrt{\frac{V}{U}}\frac{Ph}{M}.$$

4 Results

4.1 Checking the CSDE method

The accuracy of the CSDE method is checked against two problems for which mode mixity solutions exist. A problem that has an analytical solution is a homogeneous DCB specimen loaded by moments on the one beam and on the uncracked end of the specimen (Fig. 4a). The actual combination of moments gives the exact mode mixity value $\psi = \tan^{-1}(\sqrt{3/4}) \approx 40.89°$ (Hutchinson and Suo 1992). Applying the CSDE method to a FEM solution, we obtain $\psi = 40.85°$.

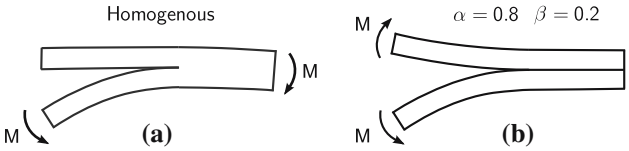

Fig. 4 Two problems with known solutions for the mode mixity, ψ. (**a**) A homogeneous DCB specimen loaded by moments on the one beam and on the uncracked end. (**b**) A bimaterial with an interface crack loaded by moments on both the cracked beams

Another example is a bimaterial structure, which was solved by Suo and Hutchinson (1990) (see Fig. 4b). The materials in the bimaterial structure are specified by $\alpha = 0.8$ and $\beta = 0.2$. The beams have the same thickness. The structure is loaded by equal sized moments on the each of the cracked beams. The solution by Suo and Hutchinson (1990) gives $\psi = 22.77°$. The CSDE method gave $\psi = 22.91°$.

In addition, for all sandwich problems analyzed in the current work a consistency check was made; the energy release rate computed with the CSDE method was compared with the energy release rate calculated analytically with (16). For all the presented solutions the deviation was less than 0.5%.

The load independence of ω was checked for a few cases by analyzing two different load combinations on the same sandwich. For a sandwich specimen with $\eta = 10$, $\Sigma = 0.001$ and $\beta = -0.4$, the difference between ω extracted from a case with $M \neq 0$ and $P = 0$ and a case where $M = 0$ and $P \neq 0$ was less than 0.05°.

4.2 Sandwich specimens with zero thickness core

An important class of three-layered structures for which $H \gg h$ is adhesive joints. Consequently, the analysis of a sandwich specimen with very thin core $\eta = h/H \to 0$ is of special interest. Here, we estimate ω for $\eta = 0$ by linear extrapolation to $\eta = 0$ using values of ω for $\eta = 0.1$ and $\eta = 0.15$. Values of ω determined by this simple method is shown in Table 1 for different values of the mismatch parameters Σ and β.

In order to check the accuracy of this extrapolation method we compare with results from the literature. Suo and Hutchinson (1989) analyzed a sandwich specimens with "zero" thickness core for materials with moderate elastic mismatch ($|\alpha| \leq 0.8$). However, in that study, a shift angle ω^* was defined slightly different than here; the relation between ω used in the present paper and ω^* is $\omega^* = \omega + \gamma - 90°$. In Fig. 5, ω^*, determined with

Table 1 Load-independent phase angle ω (in degrees) calculated for different values of the mismatch parameter Σ and β for $\eta = 0$

β	$\Sigma = 0.1$	$\Sigma = 0.05$	$\Sigma = 0.01$	$\Sigma = 0.005$	$\Sigma = 0.001$
0	34	29	20	17	13
−0.1	31	28	23	21	19
−0.2	27	25	22	21	21
−0.3	21	20	18	17	18
−0.4	14	12	11	10	10

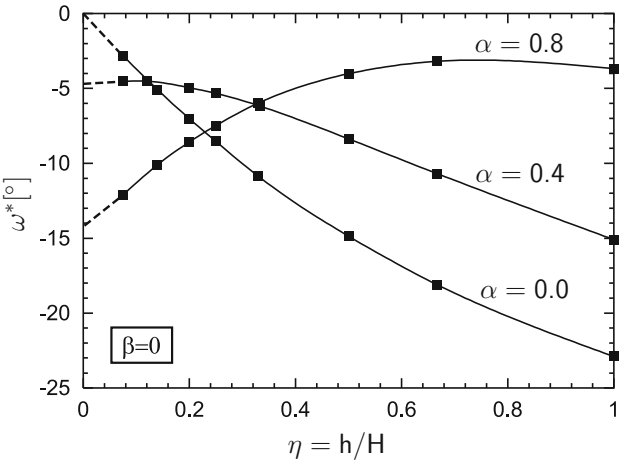

Fig. 5 The shift angle $\omega^* = \omega + \gamma - 90°$ determined for sandwich specimens with thin core. The *dashed line* shows the extrapolation to $\eta = 0$ through the values found at $\eta = 0.1$ and $\eta = 0.15$

Table 2 The phase angle ω (in degrees) computed with different values of the mismatch parameters Σ and β for a specimen with thickness ratio $\eta = 0.2$

β	Σ:	0.5		0.1	0.05	0.01	0.005	0.001
	α:	−1/3	−1/2					
−0.4				27.1	26.1	24.4	23.9	23.0
−0.3		34.6	34.2	31.8	30.5	28.5	27.6	26.4
−0.2		39.7	38.9	35.7	33.9	30.8	29.9	28.4
−0.1		44.2	43.1	38.6	36.1	31.5	30.2	28.0
0.0		48.3	46.7	40.1	36.0	27.7	24.8	19.7

our method, is plotted as function of η for three values of α and with $\beta = 0$. The dashed lines indicate linear extrapolation to $\eta = 0$ using the values found at $\eta = 0.15$ and $\eta = 0.1$. The results from Suo and Hutchinson (1989) are $\omega^*(\alpha = 0) = 0°$, $\omega^*(\alpha = 0.4) = -4.7°$ and $\omega^*(\alpha = 0.8) = -14.3°$. Our results agree with them with an accuracy better than 0.5°.

4.3 The phase angle, ω, calculated for sandwich specimens with finite core thickness

Tables 2–9 present ω for a wide range of material combinations and face sheet/core thickness ratios relevant for engineering purposes.

Some selected results are shown in Fig. 6; ω is shown as function of Σ and η. First, focus on the result for $\beta = 0$ (solid lines). With $\beta = 0$ it follows from (4) and (7) that the real and imaginary parts of the complex stress intensity factor reduce to classical mode I and mode II stress intensity factors. Then, ω can be understood as the phase angle of classical stress intensity factors for a specimen loaded with an axial force, so that $\omega = 0°$ corresponds to pure mode I and $\omega = 90°$ is pure mode II. For Σ close to unity, ω is not very sensitive to η; indeed, for $\Sigma \to 1$ the results for all η appear to converge towards the same value. This value, $\omega = 49.1°$, which is shown by an arrow in Fig. 6, is the value obtained for the symmetric, homogeneous DCB

Table 3 The phase angle ω (in degrees) computed with different values of the mismatch parameters Σ and β for a specimen with thickness ratio $\eta = 0.5$

β	Σ:	0.5		0.1	0.05	0.01	0.005	0.001
	α:	$-1/3$	$-1/2$					
-0.4				36.1	35.7	37.0	35.6	31.4
-0.3		38.9	39.6	39.9	39.2	38.5	37.1	33.4
-0.2		43.3	43.7	43.2	41.9	39.0	37.0	34.2
-0.1		47.3	47.4	45.7	43.8	36.7	37.0	33.2
0.0		51.0	50.7	47.4	44.4	33.1	33.6	27.1

Table 4 The phase angle ω (in degrees) computed with different values of the mismatch parameters Σ and β for a specimen with thickness ratio $\eta = 1$

β	Σ:	0.5		0.1	0.05	0.01	0.005	0.001
	α:	$-1/3$	$-1/2$					
-0.4				42.7	43.7	42.8	41.7	38.9
-0.3		40.9	42.7	46.3	46.8	45.0	43.6	40.1
-0.2		45.2	46.8	49.5	49.5	46.6	44.7	40.4
-0.1		49.3	50.5	52.3	51.7	47.3	44.9	39.3
0.0		53.1	54.1	54.6	53.2	46.7	43.3	35.1

Table 5 The phase angle ω (in degrees) computed with different values of the mismatch parameters Σ and β for a specimen with thickness ratio $\eta = 2$

β	Σ:	0.5		0.1	0.05	0.01	0.005	0.001
	α:	$-1/3$	$-1/2$					
-0.4				47.3	50.3	52.7	52.0	48.6
-0.3		41.9	44.3	51.0	53.5	54.7	53.5	49.3
-0.2		46.3	48.5	54.4	56.5	56.4	54.7	49.4
-0.1		50.5	52.5	57.7	59.2	57.7	55.4	48.7
0.0		54.6	56.3	60.7	61.6	58.4	55.3	46.5

Table 6 The phase angle ω (in degrees) computed with different values of the mismatch parameters Σ and β for a specimen with thickness ratio $\eta = 4$

β	Σ:	0.5		0.1	0.05	0.01	0.005	0.001
	α:	$-1/3$	$-1/2$					
-0.4				49.3	53.8	60.7	61.8	60.1
-0.3		42.3	45.0	53.2	57.3	62.9	63.4	60.6
-0.2		46.8	49.3	56.9	60.5	64.9	64.8	60.8
-0.1		51.1	53.4	60.4	63.6	66.8	66.1	60.6
0.0		55.3	57.4	63.9	68.4	68.4	67.1	59.8

specimen ($\Sigma = 1$, $\eta = 0$). With ω close to 45°, the mode II and mode I stress intensity factor are almost of the same magnitude.

With decreasing Σ, the values of ω become sensitive to η. For large η values, ω increase with decreasing Σ. For instance, for $\eta = 10$, $\omega \approx 75°$ for $\Sigma = 0.001$. Thus, for large η, the decreasing Σ results in the crack-tip stress field becoming more mode II. For $\eta \to 0$, the opposite trend is found. Here, ω decreases with decreasing Σ, corresponding to a more mode I dominant crack-tip stress field.

Figure 6 also includes a few results for $\beta = -0.3$. Those results differ from those obtained for $\beta = 0$, suggesting that the dependence of ω on β is signifi-

Table 7 The phase angle ω (in degrees) computed with different values of the mismatch parameters Σ and β for a specimen with thickness ratio $\eta = 6$

β	Σ:	0.5		0.1	0.05	0.01	0.005	0.001
	α:	$-1/3$	$-1/2$					
-0.4				49.7	54.7	63.5	65.7	66.6
-0.3		42.4	45.1	53.7	58.3	65.8	67.4	67.0
-0.2		46.9	49.5	57.5	61.6	68.0	69.1	67.4
-0.1		51.2	53.7	61.2	64.9	70.1	70.6	67.6
0.0		55.5	57.7	64.7	68.1	72.2	72.1	67.4

Table 8 The phase angle ω (in degrees) computed with different values of the mismatch parameters Σ and β for a specimen with thickness ratio $\eta = 8$

β	Σ:	0.5		0.1	0.05	0.01	0.005	0.001
	α:	$-1/3$	$-1/2$					
-0.4				49.9	55.1	64.7	67.5	70.3
-0.3		42.4	45.2	53.9	58.7	67.1	69.4	70.8
-0.2		47.0	49.5	57.8	62.1	69.5	71.2	71.3
-0.1		51.3	53.8	61.5	65.4	71.7	72.9	71.7
0		55.6	57.9	65.1	68.7	73.9	74.5	71.9

Table 9 The phase angle ω (in degrees) computed with different values of the mismatch parameters Σ and β for a specimen with thickness ratio $\eta = 10$

β	Σ:	0.5		0.1	0.05	0.01	0.005	0.001
	α:	$-1/3$	$-1/2$					
-0.4				50.0	55.3	65.4	68.5	72.6
-0.3		42.4	45.2	54.0	58.9	67.9	70.5	73.2
-0.2		47.0	49.6	57.9	62.4	70.3	72.3	73.8
-0.1		51.3	53.8	61.6	65.7	72.6	74.2	74.3
0		55.6	57.9	65.3	69.0	74.8	75.9	74.8

cant, except for small Σ. However, for large Σ, the effect of β on ω is complex, see Tables 2–9.

4.4 Lengths of sandwich specimens

As mentioned, the analytical expression for the energy release rate (16) is derived by evaluating the J-integral along the exterior boundaries of the specimen using the stress field corresponding to loading by moments and axial forces. However, this distribution of the stresses is only true when the stress field from the crack tip is far from the ends of the specimen. For short specimens, the crack tip stress field reaches the boundaries along which the J-integral is evaluated. Since this is not taken into account in the analytical result (16), the analytical G will deviate from the true J-integral value. For material combinations with small elastic mismatch this problem is not very pronounced since the stress field at the crack tip is confined to a small region around the crack tip. For materials with larger elastic mismatch, the extension of this zone is significantly larger. Figure 7 shows how the material mismatch parameter Σ affects the stress field. From the figure it is clear that the stress field elongates, in particular towards the uncracked end of the specimen, as the elastic mismatch between core and face sheet becomes larger.

Consequently, when choosing the dimensions for a test specimen, it is crucial that the specimen is sufficiently long, so that the stresses along the ends of the sandwich are unaffected by the stresses from the crack tip, so that the results in Sects. 3 and 4 apply. For this purpose we have established a novel method that estimates the maximum deviation between the analytical energy release rate (16) (here denoted G_{ana}) and the true energy release rate G_{true}. We calculate G_{true}

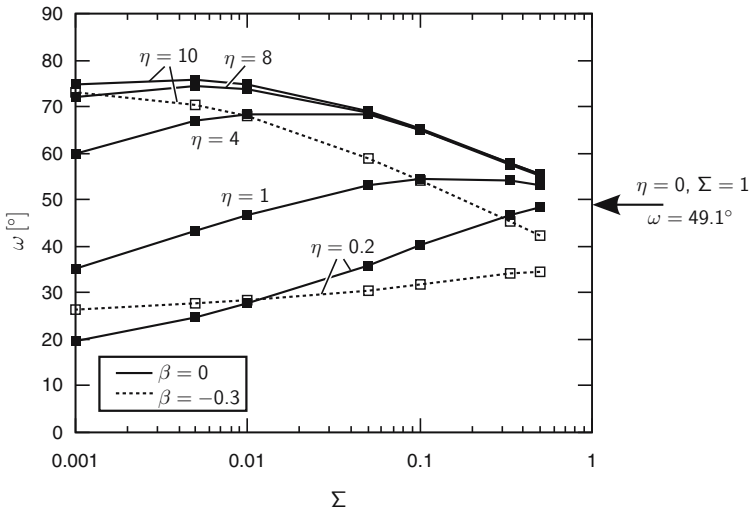

Fig. 6 The load-independent phase angle ω as function of the elastic mismatch parameter Σ for a number of different thickness ratios. The *arrow* indicate the value corresponding to a symmetric, homogeneous DCB specimen loaded by an axial force

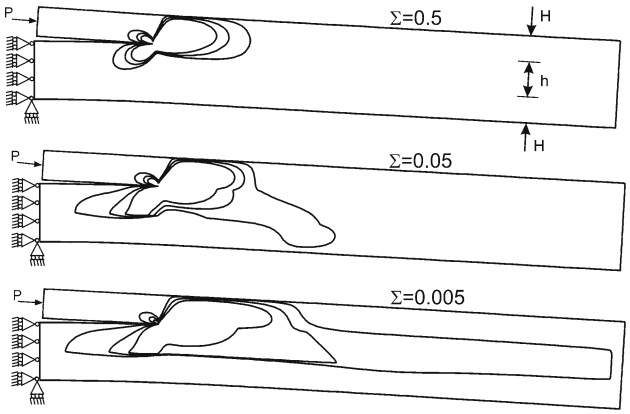

Fig. 7 The shear stress contours $\sigma_{12}H/P = 0.1,\ 0.05,\ 0.01$ for a sandwich specimen with $\eta = 1$, $\beta = -0.2$ and $\Sigma = 0.5, 0, 05$ and 0.005, respectively

from a FEM solution with the CSDE method. First, the method determines the load combination that results in the largest deviation between G_{ana} and G_{true} and then it calculates an relative error $\xi = \left|\frac{G_{\text{ana}} - G_{\text{true}}}{G_{\text{true}}}\right|$ for this combination of the loads. Details on the procedure is found in Appendix C. Figure 8a–d shows curves for the intact length of the specimen, $(L-a)/H$, that gives an error $\xi = 0.05$.

The curves show that for $\Sigma > 0.01$, the length of the intact part of the sandwich specimen must be larger than $10H$ to ensure that the error, ξ, stays below 5%. This holds for all analyzed values of $\eta \leq 8$. For an elastic mismatch $\Sigma = 0.001$, $(L-a)$ must be larger to ensure low errors on G. For instance, a sandwich specified by $\eta = 1$, $\Sigma = 0.001$ and $\beta = 0$ an error $\xi = 5\%$ is found for $(L-a)/H = 27$.

It was found that the error, ξ, is strongly dependent on $(L-a)/H$ and a small change of $(L-a)$ changes ξ significantly. Increasing $(L-a)$ with $2H$, typically results in an error that is practically zero; vice versa, reducing the length with $2H$ results in large deviations on G.

As seen in Fig. 7 the stress field also elongates slightly towards the cracked end of the specimen ($x_1 = -a$). However, an investigation showed that errors above 1% does not appear for $a/H > 4$.

5 Example: a method for measuring interfacial fracture toughness of sandwich specimens under mixed mode loadings

It is well known from experiments and modeling works that the fracture toughness of weak interfaces can depend on the mode mixity (Cao and Evans 1989; Wang and Suo 1990; Liechti and Chai 1992;

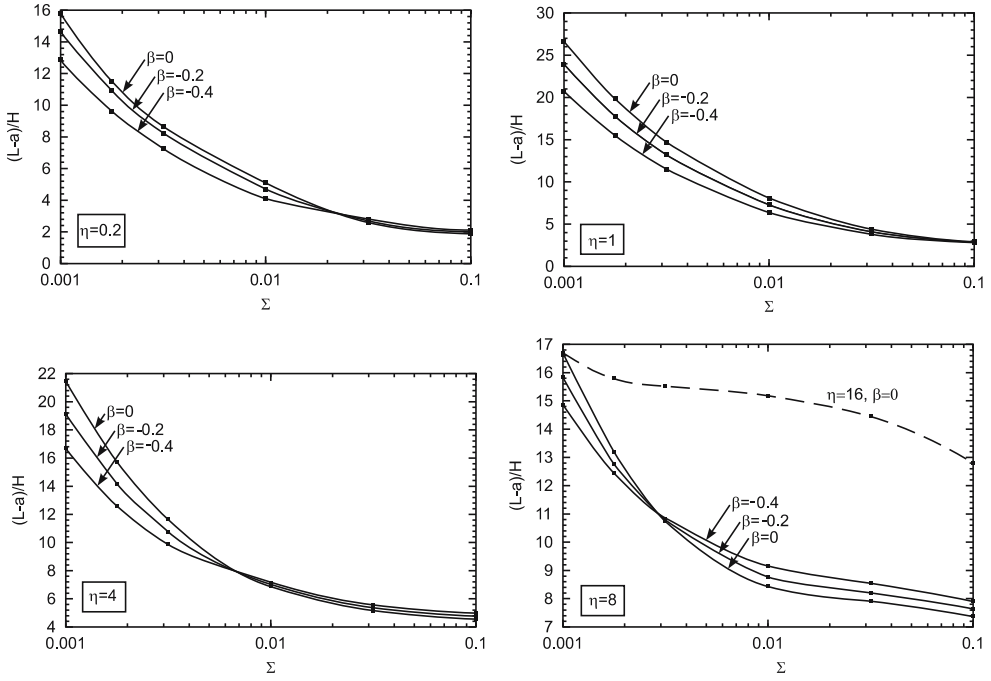

Fig. 8 The curves show normalized lengths of the intact part of the sandwich specimen that gives 5% error in the energy release rate calculated by (16)

Tvergaard and Hutchinson 1993). A detailed fracture mechanical characterization of the interface would thus include measuring interfaces under various mode mixities.

Inspired by Sørensen et al. (2006), we propose a test set-up for measuring the interfacial fracture toughness for face sheet/core debonding under mixed mode loading conditions. The test is based on a double cantilever beam sandwich specimen loaded with uneven bending moments (DCB-UBM). The moments are applied by a wire/roller system at the cracked ends of the specimen. The uncracked end is supported by rollers maintaining static equilibrium. Figure 9 shows a sketch of the test set-up. The force in the wire is assumed to be the same everywhere and the applied moments are then determined solely from the wire force, F, and the moment arms, ℓ_1 and ℓ_2. The ratio between the applied moments are $\frac{\ell_1}{\ell_2}$ and this ratio is altered by changing the distance between the rollers on each arm.

The imposed loading consists of the moments M_1, M_2 and $M_3 = M_1 - M_2$ and is a special case of the load situation analyzed above ($P_1 = P_2 = P_3 = 0$). For this load combination the energy release rate is

$$G = \frac{c_2}{16h^3}\left(\frac{M_1^2}{I_1} + \frac{M_2^2}{I_2} - \frac{(M_1 - M_2)^2}{I_3}\right).$$

The mode mixity is obtained from (17) where now λ becomes

$$\lambda = \sqrt{\frac{V}{U}}\frac{\frac{M_1}{M_2}C_2 - C_2}{\frac{M_1}{M_2}(C_3 - 1) - C_3}. \tag{18}$$

As an example, consider an adhesive joint consisting of aluminum adherents having the elastic constants $E_2 = 70GPa$, $\nu_2 = 0.3$ and epoxy adhesive with the the elastic constants $E_1 = 7$ GPa and $\nu_1 = 0.3$. Assume that $\eta = h/H = 0.1$. Assuming plane strain conditions, (2) and (1) give $\Sigma \approx 0.1$ and $\beta = -0.28 \approx -0.3$, respectively. From Table 1 we find $\omega(\Sigma = 0.1,\ \beta = -0.3,\ \eta = 0) = 21°$ and from Table 2 we obtain $\omega(0.1, -0.3, 0.2) = 32°$. By linear interpolation between these two values we find an estimate of the phase angle $\omega(0.1, -0.3, 0.1) \approx 26.5°$.

Having determined ω, we obtain the load ratio parameter λ from (18). Then, we can determine ψ for any combination using (17). The mode mixity is shown as function of the ratio between the moments in Fig. 10.

As a second example, consider a sandwich specimen with a polymer foam core ($E_1 = 200$ MPa, $\nu_1 = 0.3$) and glass fiber face sheets ($E_2 = 40$ GPa, $\nu_2 = 0.3$). Assuming plane strain conditions, (2) and (1) gives $\Sigma \approx 0.005$ and $\beta = -0.28 \approx -0.3$. Here we assume $\eta = 5$.

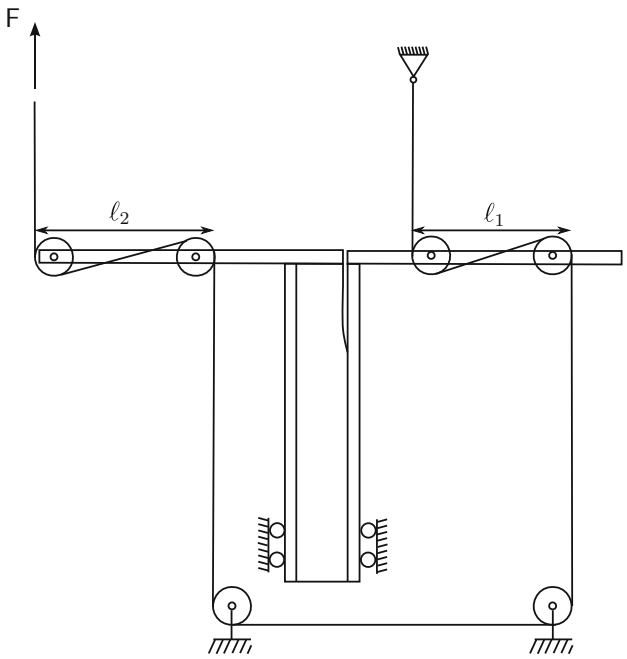

Fig. 9 Test setup for measuring fracture toughness of sandwich structures under face sheet core debonding; uneven bending moments are applied to a sandwich structure

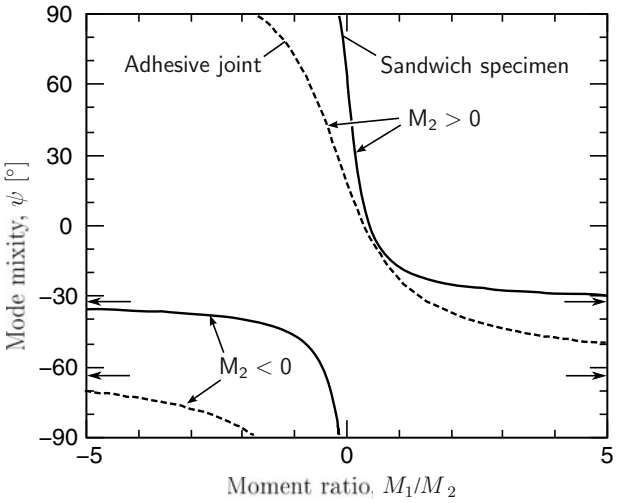

Fig. 10 The mode mixity as function of the ratio M_1/M_2 for an adhesive joint (*dashed line*) and a sandwich specimen (*solid line*). The adhesive joint is characterized by $\eta = 0.1$, $\Sigma = 0.1$ and $\beta = -0.3$. For the sandwich specimen these constants are $\eta = 5$, $\Sigma = 0.01$ and $\beta = -0.3$. *Arrows* indicates asymptotic values for $|M_1/M_2| \to \infty$

From Table 6 we find $\omega(0.005, -0.3, 4) = 63.4°$ and from Table 7 we find $\omega(0.005, -0.3, 6) = 67.4°$, respectively. Now by interpolating we find for $\eta = 5$ that $\omega(0.005, -0.3, 5) = 65.4°$.

It is seen in Fig. 10 that the entire mode mixity range $-90° \leq \psi \leq 90°$ can be obtained for the DCB-UBM sandwich specimen simply by changing the moment ratio, M_1/M_2. For both examples, most of the variation in ψ occurs for $|M_1/M_2| < 1$. The curves for the sandwich specimen and the adhesive joint differ considerably. For $\psi < -25°$ and $\psi > 60°$ there is a relative large difference in the required moment ratio of the two examples. A plot like Fig. 10 is useful if we wish to select the moment ratio, M_1/M_2, for a desired ψ.

6 Discussion

The problem analyzed in the present paper covers any load situation consisting of moments and normal forces applied to the ends of the sandwich structure. Nevertheless, the analysis does not include effects of trans-

verse forces that are also of major importance in many practical applications. This has the implication that the moment applied to the sandwich must be pure moments and cannot be introduced by a transverse force. In the presence of a transverse shear force, the analysis becomes more comprehensive. Then, the energy release rate is dependent on β, the crack length and numerical calculation of corrections for the energy release rate must be determined Li et al. (2004). Furthermore, another phase angle must be calculated for the transverse force. An extension of the present analysis to include the effect of transverse forces would be of great interest and would complete the analysis of fracture of the sandwich specimen.

7 Summary and conclusions

In the present work, some aspects of debonding of sandwich structures have been analyzed within the framework of linear elastic fracture mechanics.

The problem of a delaminated sandwich structure loaded with end-loads and moments was recast into an equivalent, reduced problem consisting of only two independent load parameters. The energy release rate was evaluated and presented in closed-analytical form by evaluation of the J-integral. Furthermore, a load-independent phase angle was introduced so the mode mixity could be determined for any combination of the loads. This phase angle was computed for a number of relevant sandwich configurations using a novel CSDE method.

The analytical results were based on classical beam theory. This is an exact solution for long specimens. However, for short specimens, the stresses at the ends of the sandwich specimen are affected by the crack tip stress field. Then, the present analysis is not strictly applicable. An analysis was made to determine minimum specimen length for which the analytical solution for the energy release rate and mode mixity are accurate. For sandwich specimens with moderate elastic mismatch between face sheets and core the results are fairly accurate unless the uncracked part of the sandwich becomes shorter than $10H$. For materials with very large elastic mismatch, the uncracked part of the sandwich specimen must be significantly longer.

Appendix

A The stress along the edges of a sandwich containing an interface crack

In order to evaluate the J-integral, the stresses along the beam end-sections must be known. Three end-sections, denoted $k = 1$, 2 and 3, respectively, are considered: at $x_1 = -a$ and $x_2 > 0$ ($k = 1$), $x_1 = -a$ and $x_2 < 0$ ($k = 2$), $x_1 = L - a$ ($k = 3$). The sandwich specimen is loaded by moments M_k and normal forces P_k ($k = 1, 2, 3$). The strain, $\epsilon_{11,k}$, along the beam end-section, k, where M_k and P_k act, can be found from classic beam theory which is an exact solution when no shear stresses are present

$$\epsilon_{11,k}(y_k) = \frac{P_k}{\int_{y_k} E\,\mathrm{d}y_k} + \frac{M_k}{\int_{y_k} y_k^2\,\mathrm{d}y_k} y_k = \frac{P_k}{\bar{E}_2 h A_k} + \frac{M_k}{\bar{E}_2 h^3 I_k} y_k,$$

where y_k is the distance from the neutral axis of section number k. That is $y_1 = x_2 - H/2$, $y_2 = x_2 + H + h - \delta$ and $y_3 = x_2 + h/2$, see Fig. A.1. M_k and P_k are positive as defined in Figs. 1 and A.1. The stresses are found according to Hooke's law $\sigma_{11}(y_k) = \bar{E}(y_k)\epsilon_{11}(y_k)$, where the appropriate $\bar{E}$ must be used ($\bar{E}_1$ for $-h \le x_2 \le 0$ and $\bar{E}_2$ otherwise).

For $k = 1$ the constants involved in the strain expression are

$$A_1 = \frac{1}{\eta} \text{ and } I_1 = \frac{1}{12\eta^3}.$$

For $k = 2$ the strains are calculated using Suo and Hutchinson (1990):

$$A_2 = \frac{1}{\eta} + \Sigma$$

$$I_2 = \frac{1}{3\eta^3} + \frac{\Delta}{\eta}\left(\Delta - \frac{1}{\eta}\right) + \Sigma\left[\left(\frac{1}{\eta} - \Delta\right)^2 + \left(\frac{1}{\eta} - \Delta\right) + \frac{1}{3}\right].$$

For $k = 3$ we find

$$A_3 = \frac{2}{\eta} + \Sigma \text{ and } I_3 = \frac{2}{\eta^3} + \frac{3}{2\eta} + \frac{3}{\eta^2} + \frac{\Sigma}{4}.$$

B Extracting the mode mixity and energy release rate from a finite element model

The complex stress intensity factor is related to the crack displacement components via (Fig. 2). Rewriting

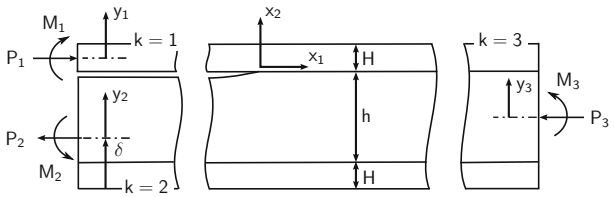

Fig. A.1 Definition of coordinate axis y_1, y_2 and y_3 for sections $k = 1$, $k = 2$ and $k = 3$, respectively

(Fig. 2) to modulus-argument form we get

$$\begin{aligned}\Delta u_1 + \mathrm{i}\Delta u_2 = & \ |\Delta u| e^{\mathrm{i}\phi} \\ = & \ \frac{c_1 + c_2}{2\sqrt{2\pi}\sqrt{1+4\epsilon^2}\cosh \pi\epsilon} K r^{\mathrm{i}\epsilon+1/2} e^{-\mathrm{i}\varphi},\end{aligned} \tag{B.1}$$

where $\varphi = \tan^{-1} 2\epsilon$, $|\Delta u| = \sqrt{\Delta u_1^2 + \Delta u_2^2}$ and ϕ is the phase angle of the openings given by

$$\phi = \arctan \frac{\Delta u_1}{\Delta u_2}.$$

Now, by combining (B.1) with (7) we get the mode mixity

$$\psi = \phi - \epsilon \ln r/l + \arctan 2\epsilon.$$

Furthermore, by combining (B.1) with (6) we can find the energy release rate from the crack face displacements via

$$G = \frac{\Delta u_2^2 + \Delta u_1^2}{r} \frac{(1+4\epsilon^2)\pi}{2(c_1 + c_2)}. \tag{B.2}$$

The crack surface displacement components (Δu_1 and Δu_2) are found with the finite element method. However, when calculating G and ψ it turns out that these are not invariants of r. This is because the near-tip stress and displacement fields given by (4) and (5) are only the first (but singular) term in a Taylor series (Rice 1988). The singular stress and displacement fields become more and more dominant as approaching the crack tip. Consequently, for $r \to 0$ the singularity dominate. Based on this reasoning we suggest a CSDE method where the quantities $G(r)$ and $\psi(r)$ are extrapolated to $r \to 0$.

The FE analysis was carried out using the Ansys 6.0 FE package. Figure B.1 shows a typical mesh used in the calculations. The elements were 8 noded isoparametric linear elastic elements. Typically, the quadratic fine mesh around the crack tip had a width of $H/4$ and contained 40 rings with decreasing spacing towards the crack tip. The distance between the inner rings was 1/100 of the distance between the outer rings. The size of the inner elements was $H/500$. The elements outside the fine region had a rectangular shape and were slightly elongating towards the ends of the mesh.

It is well known that in a linear elastic analysis of a sharp interface crack, the elements closest to the crack tip cannot resolve the displacement accurately. Therefore, a few nodes closest to the crack should not be used for the extrapolation. In our calculations, the 10 inner node pairs were typically omitted from the calculations. The present results were typically obtained by using nodes in the range $1/25 < r/H < 1/10$.

The accuracy of the method was evaluated by checking the deviation between the exact G calculated from (16) and the G calculated with the CSDE method. For all the computations the deviation was less that 0.5%.

C Estimating the error on the analytical determined energy release rate for short specimens

In Sect. 4.4, curves are given that represent the uncracked length of the sandwich that result in an error of 5% on the analytical G. Here, equations are given for determining the combination of the loads P and M that result in the greatest error on G and calculate the error for a sandwich specimen.

For any sandwich length L and crack length a, linearity dictates that the complex stress intensity factor can be written as

$$\begin{aligned}K &= K_1(P, M) + \mathrm{i}K_2(P, M) \\ &= (k_1 H P + k_2 M) + \mathrm{i}(k_3 H P + k_4 M),\end{aligned} \tag{C.1}$$

where k_1, k_2, k_3 and k_4 are real constants that depend on α, β, η, $(L-a)/H$ and a/H. These k's can generally not be determined by analytical means. Therefore, a numerical method e.g the finite element method must be employed. In order to determine the four k's by the finite element method, two different load situations must be solved for each set of α, β, η, $(L-a)/H$ and a/H. First, using the load situation in Fig. 3c with $P = 1/H$, $M = 0$, k_1 and k_3 are given directly as the real part and the imaginary of the complex stress

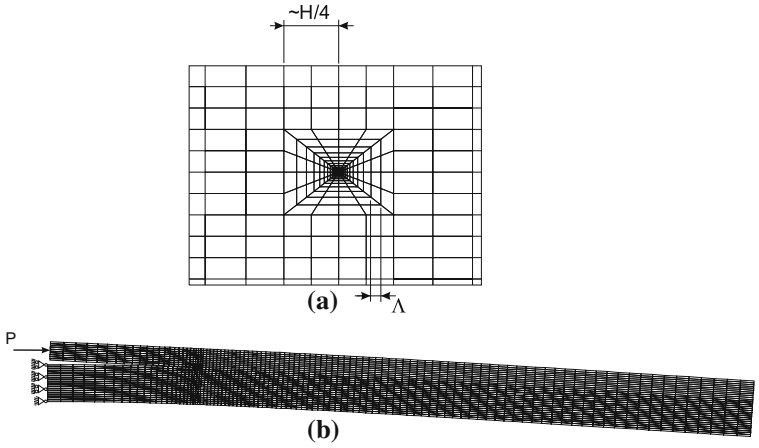

Fig. B.1 Mesh used in the analysis

intensity factor, respectively. Analogously, k_2 and k_4 are determined with $P = 0$ and $M = 1$.

The imaginary and the real parts of K are

$$\Im(K) = \left(G\frac{16\,\cosh^2\pi\epsilon}{c_1+c_2}\right)^{1/2}\sin\left(\psi - \epsilon\,\ln\,H\right)$$

and

$$\Re(K) = \left(G\frac{16\,\cosh^2\pi\epsilon}{c_1+c_2}\right)^{1/2}\cos\left(\psi - \epsilon\,\ln\,H\right),$$

respectively. G and ψ are determined by the CSDE method described in Appendix B.

In order to characterize the deviation on the energy release rate between a long sandwich specimen where the homogeneous strain state is present and one with a more complex strain field (e.g. caused by a too short uncracked beam length), the following error measure is introduced

$$\xi = \left|\frac{|K|^2_{\text{num}} - |K|^2_{\text{ana}}}{|K|^2_{\text{num}}}\right|. \tag{C.2}$$

Here $|K|_{\text{num}}$ is the modulus of K determined numerically by the CSDE method and $|K|_{\text{ana}}$ is the modulus of K determined analytically according to the results in Sect. 3.

Having determined the k's numerically and introducing $\bar{\lambda} = \frac{PH}{M}$, it is found that

$$K_{\text{num}} = \left\{(k_1\bar{\lambda} + k_2) + \mathrm{i}(k_3\bar{\lambda} + k_4)\right\}M$$

and the modulus of K_{num} squared can then be written as

$$|K|^2_{\text{num}} = \left\{(k_1\bar{\lambda} + k_2)^2 + (k_3\bar{\lambda} + k_4)^2\right\}M^2, \tag{C.3}$$

which we will rewrite in the form

$$|K|^2_{\text{num}} = B\bar{\lambda}^2 + C\bar{\lambda} + D, \tag{C.4}$$

where

$$B = k_3^2 + k_1^2$$

$$C = 2(k_3k_4 + k_1k_2)$$

$$D = k_4^2 + k_2^2.$$

Using (16) and (6), an analytical expression based on the strain fields given in Appendix A for the modulus of the complex stress intensity factor is found

$$|K|^2_{\text{ana}} = (b\bar{\lambda}^2 + c\bar{\lambda} + d)M^2 \tag{C.5}$$

$$b = q\,\frac{1}{H^3}\,\frac{\eta}{U}$$

$$c = q\,\frac{1}{H^3}\,\frac{2\,\sin\,\gamma}{\sqrt{UV}\eta^2}$$

$$d = q\,\frac{1}{H^3}\,\frac{1}{\eta^3 V},$$

where $q = \frac{c_2\cosh^2(\pi\epsilon)}{c_1+c_2}$.

For fixed α, β, η and a/H the error, ξ, depends on $(L-a)$ and $\bar{\lambda}$. In order to determine the error for a certain length, the worst case load combination, $\bar{\lambda}_c$, is determined. $\bar{\lambda}_c$ is found by differentiating (C.2) and setting $\frac{\partial\xi}{\partial\bar{\lambda}} = 0$. The derivative of (C.2) is

$$\frac{\partial\xi}{\partial\bar{\lambda}} = -\frac{(dB - bD)\,\bar{\lambda}^2 + (2\,cB - 2\,bC)\,\bar{\lambda} + cD - dC}{\left(B\bar{\lambda}^2 + C + D\bar{\lambda}\right)^2}$$

Equating this to zero gives two values of $\bar{\lambda}_c$

$$\bar{\lambda}_c = \frac{bC - cB \pm 2\sqrt{b^2C^2 - 2\,bCcB + c^2B^2 - dBcD + d^2BC + bD^2c - bDdC}}{dB - bD}.$$

Inserting $\bar{\lambda}_c$ into (C.4) and (C.5) gives $|K|^2_{\text{num}}$ and $|K|^2_{\text{ana}}$, respectively. Inserting those values into (C.2) gives ξ.

References

Akisanya AR, Fleck NA (1992) Analysis of a wavy crack in sandwich specimens. Int J Fract 55(1):29–45

Berggren C, Simonsen BC, Borum KK (2007) Experimental and Numerical study of interface crack propagation in foam-cored sandwich beams. J Compos Mater 41(4):493–520

Cantwell WJ, Compston P, Reyes G (2000) Fracture properties of novel aluminum foam sandwich structures. J Mater Sci Lett 19(24):2205–2208

Cao HC, Evans AG (1989) An experimental study of the fracture resistance of bimaterial interfaces. Mech Mater 7(4):295–304

Carlsson LA, Prasad S (1993) Interfacial fracture of sandwich beams. Eng Fract Mech 44(4):581–590

Dundurs J (1967) Effect of elastic constants on stress in composite under plane deformation. J Compos Mater 1(3):310–322

Dundurs J (1969) Discussion: edge-bonded dissimilar orthogonal elastic wedges under normal and shear loading. Trans ASME J Appl Mech 650–652

Fleck NA, Hutchinson JW, Suo Z (1991) Crack path selection in a brittle adhesive layer. Int J Solids Struct 27(13):1683–1703

Hutchinson JW, Suo Z (1992) Mixed mode cracking in layered materials. Adv Appl Mech 29(11):63–191

Kinloch AJ (1987) Adhesion and adhesives. Chapman & Hall, London

Li S, Wang J, Thouless MD (2004) The effects of shear on delamination in layered materials. J Mech Phys Solids 52(1):193–214

Liechti KM, Chai YS (1992) Asymmetric shielding in interfacial fracture under in-plane shear. Trans ASME J Appl Mech 59(2):295–304

Østergaard RC, Sørensen BF, Brøndsted P (2007) Measurement of interface fracture toughness of sandwich structures under mixed mode loadings. J Sandwich Struct Mater (in press)

Prasad S, Carlsson LA (1994) Debonding and crack kinking in foam core sandwich beams. ii. Experimental investigation. Eng Fract Mech 47(6):825–841

Ratcliffe J, Cantwell WJ (2001) Center notch flexure sandwich geometry for characterizing skin–core adhesion in thin-skinned sandwich structures. J Reinforced Plast Compos 20(11):945–970

Rice JR (1988) Elastic fracture mechanics concepts for interfacial cracks. J Appl Mech Trans ASME 55(1):98–103

Sørensen BF, Jakobsen TK, Jørgensen K, Østergaard RC (2006) DCB-specimen loaded with uneven bending moments. Int J Fract 141(1-2):163–176

Suo Z, Hutchinson JW (1989) Sandwich test specimens for measuring interface crack toughness. Mater Sci Eng A: Struct Mater: Properties Microstr Process A107(1):135–143

Suo Z, Hutchinson JW (1990) Interface crack between two elastic layers. Int J Fract 43(1):1–18

Thouless MD, Evans AG, Ashby MF, Hutchinson JW (1987) Edge cracking and spalling of brittle plates. Acta Metall 35(6):1333–1341

Tvergaard V, Hutchinson JW (1993) The influence of plasticity on mixed mode interface toughness. J Mech Phys Solids 41(6):1119–1135

Wang JS, Suo Z (1990) Experimental determination of interfacial toughness curves using brazil-nut-sandwiches. Acta Metall Mater 38:1279–1290

Williams ML (1959) The stress around a fault or crack in dissimilar media. Bull Seismo Soc Am 49:199–204

Zenkert D (1995) An introduction to sandwich construction. Engineering Materials Advisory Services Ltd., London

[P2]

Journal of Sandwich Structures and Materials, **9**(5), p. 445-466.

Measurement of Interface Fracture Toughness of Sandwich Structures under Mixed Mode Loadings

RASMUS C. ØSTERGAARD,* BENT F. SØRENSEN AND POVL BRØNDSTED

Material Research Department, Risø National Laboratory
Frederiksborgvej 399, 4000 Roskilde, Denmark

ABSTRACT: Fracture of sandwich structures loaded with axial forces and bending moments is analyzed in the context of linear elastic fracture mechanics. A closed form expression for the energy release rate of interface cracking of a sandwich specimen is found by analytical evaluation of the *J*-integral. A method for determining the mode mixity is described and applied. Expressions are presented whereby the mode mixity can be calculated analytically for any load combination when the mode mixity is known for just one load case.

The theory presented is applied to a new test method based on double cantilever beam sandwich specimens loaded with uneven bending moments. The interface fracture toughness of two sandwich types are measured as function of the mode mixity. The sandwich structures that are tested consist of glass fiber reinforced polyester skins and PCV core. The tests show that the interface fracture toughness depends strongly on the mode mixity. Under dominated normal crack opening, the crack grows just below the interface in the core at a constant fracture toughness. Under dominated tangential crack deformation, the crack grows into the laminate resulting in extensive fiber bridging and an increase in fracture toughness. As a result of the development of a large process zone due to fiber bridging, the analysis by linear elastic fracture mechanics becomes invalid and modeling with cohesive zones is proposed.

KEY WORDS: fracture toughness, fiber bridging, energy release rate, mode mixity, LEFM.

INTRODUCTION

FRACTURE OF BRITTLE solids is often analyzed within the framework of linear elastic fracture mechanics (LEFM) which is also the most

*Author to whom correspondence should be addressed. E-mail: rasmus.c.oestergaard@risoe.dk
Figure 5 appears in color online: http://jsm.sagepub.com

1099-6362/07/05 0445–22 $10.00/0 DOI: 10.1177/1099636207070578

Los Angeles, London, New Delhi and Singapore

widespread approach for the analysis of sandwich structures. The LEFM is a convenient tool for analyzing fracture in materials and structures because analytical expressions can be derived for a wide range of practical problems. In the present work, sandwich structures with polymeric foam core and glass fiber-reinforced polymer (GFRP) skins have our primary interest. The fracture mechanisms associated with skin to core debonding will be investigated and the fracture resistance will be measured. Despite the focus on the aforementioned material combinations, the mechanics deployed in the present article are of a general character and can be used analyzing skin core debonding for sandwich structures with other material combinations.

LEFM was applied by Zenkert [1] for the analysis of skin to core debonding in sandwich structures. Carlsson and Prasad [2] conducted a study of mixed mode fracture in a specimen with isotropic material constituents where the mode mixity for different combinations of a transverse and a normal loading on the debonded sandwich skin was computed numerically. Furthermore, a comprehensive study of skin to core debonding of various types of sandwich structures was carried out by Ratcliffe and Cantwell [3], and it was found that the fracture toughness for interface debonding is in the range 170–2750 J/m^2. In the present study, LEFM for anisotropic bi-material structures [4] is used and a somewhat more general analysis is brought into context.

For cracks in interfaces between elastically dissimilar materials, the stress singularity at the crack tip is uniquely defined by the energy release rate, G and the mode mixity, ψ. A fracture criterion often applied is based on the energy release rate to be equal to a critical material value, denoted as the fracture toughness, G_c. For a crack located in an interface between two dissimilar materials, the fracture toughness can depend on the mode mixity. Liechti and Chai [5] measured the effect of the mode mixity on the fracture toughness for a crack located in a weak interface between glass and epoxy and a rise of a factor of 10 was seen for $|\psi| \to 90^\circ$ in comparison with $G_c(\psi \approx 0)$.

In the following, an analysis is carried out where the J-integral is used for calculating the energy release rate for a fairly general load situation. The load type analyzed here is rather versatile and can be applied for various practical problems. A method is then presented whereby the mode mixity can be extracted from a finite element solution of the problem. Afterwards, the mode mixity can be determined for any combination of the loads analyzed. Finally, the theory is applied to a test setup that can impose mixed mode loading to a sandwich specimen. Two types of commercially manufactured sandwich structures were tested and fracture toughness was determined as a function of mode mixity for the two. Both types had plain weave glass fiber-reinforced polyester skins. In the interface between skin

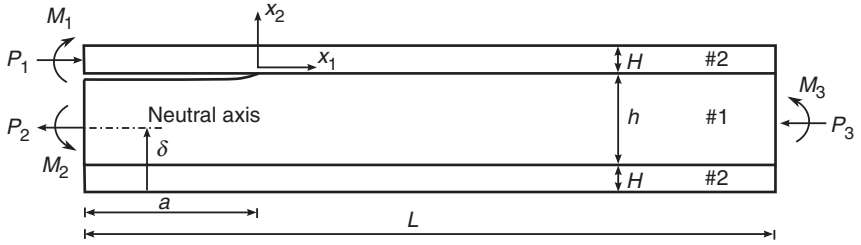

Figure 1. *Interface cracking of a sandwich with equal thickness skins is analyzed.*

and core was a layer of randomly oriented fibres (CSM). The elastic properties of the skin material were measured experimentally elsewhere [6]: $E_{11} = 14.9\,\text{GPa}$, $E_{22} = 7.53\,\text{GPa}$, $E_{33} = 16.5\,\text{GPa}$, $\nu_{13} = 0.2$, $\nu_{12} = 0.199$, $\nu_{32} = 0.16$ and $G_{12} = 2.2\,\text{GPa}$. Here, E, ν, and G are the Young's modulus, the Poisson's ratio, and the shear modulus, respectively; the subscript 1 refers to the principal material direction that is aligned with the sandwich specimen length direction (see coordinate system in Figure 1), subscript 2 denotes the out-of-plane direction and subscript 3 indicates the material axis perpendicular to 2 and 3. The fibers in the laminate plane were slightly unevenly distributed between the two principal material directions explaining the minor difference between E_{11} and E_{33}. The thickness of the sandwich skins was approximately 6 mm.

The tested sandwich structures had PVC foam core (Divinycel H80 and H130). The elastic properties of the core materials taken from [7] were used. For the H80 PVC foam, $E = 85\,\text{MPa}$, $\nu = 0.3$ and for H130, $E = 175\,\text{MPa}$, $\nu = 0.3$. The thickness of the core was approximately 40.0 mm.

In the present work we measure the fracture toughness as a function of the mode mixity. In that respect, our approach is different from the earlier studies where the fracture toughness was typically measured for only one or two mode mixities. Our approach is more information-rich and gives fracture toughness-mode mixity data that can be used as input for advanced numerical models that can account for mode mixity dependence on the fracture toughness [8].

Now, let us define a problem that is of general character and has a clear practical interest. Let the sandwich have the length L, skins of thickness H, and a core with thickness h. To keep the analysis general, the materials are considered homogeneous and orthotropic. With this choice many types of sandwich structures can be analyzed e.g., aluminium/polyvinylchloride (PVC) foam, GFRP/balsa wood, GFRP/PVC foam, etc. The isotropic behavior of some of these constituents are covered by the orthotropic description that reduces to isotropy if the elastic properties are invariant with direction. A crack with length a is located at the interface between the

core and the skin starting from the left side of the sandwich ($x_1 = -a$). The sandwich is loaded at the edges by forces per unit width, P_n, and moments per unit width, M_n, $n = 1 \ldots 3$. The problem is sketched in Figure 1.

MECHANICS OF AN INTERFACE CRACK BETWEEN TWO ELASTICALLY DISSIMILAR ORTHOTROPIC LAYERS

Material Constitutive Laws

First, let us describe the materials behavior. Both the materials are assumed to exhibit a linear elastic deformation behavior when small deformations are considered, which is reasonable for the constituents typically used in sandwich structures. The elastic deformations in the materials are described by the following relation between the stress vector, σ_i, and the strain vector, ϵ_i

$$\epsilon_i = \sum_{j=1}^{6} s'_{ij}\sigma_j, \quad i = 1 \text{ to } 6, \tag{1}$$

where

$$\epsilon_i = \epsilon_{11}, \epsilon_{22}, \epsilon_{33}, 2\epsilon_{23}, 2\epsilon_{13}, 2\epsilon_{12},$$
$$\sigma_i = \sigma_{11}, \sigma_{22}, \sigma_{33}, \sigma_{23}, \sigma_{13}, \sigma_{12},$$

and the compliance matrix s'_{ij} is given by

$$s'_{ij} = \begin{cases} s_{ij} & \text{for plane stress} \\ s_{ij} - s_{i3}s_{j3}/s_{33} & \text{for plane strain.} \end{cases}$$

The relation between the engineering constants and the compliance matrix s_{ij} can be found in appendix A.

The Singular Stress Field

Near the crack tip a singular stress field becomes dominant. The stress field in terms of the shear stress, σ_{12}, and the normal stress, σ_{22}, is given by [4]

$$\sqrt{\frac{H_{22}}{H_{11}}}\sigma_{22} + i\sigma_{12} = \frac{1}{\sqrt{2\pi}} K r^{i\epsilon - 1/2}. \tag{2}$$

Here $K = K_1 + iK_2$ is the complex stress intensity factor, $i = \sqrt{-1}$, r is the radial distance along the x_1-axis, and ϵ is the oscillatory index

$$\epsilon = \frac{1}{\sqrt{2\pi}} \ln\left(\frac{1-\beta}{1+\beta}\right),$$

where β is a generalization of the Dundurs parameter

$$\beta = \frac{\left[(s'_{11}s'_{22})^{1/2} + s'_{12}\right]_{\#1} - \left[(s'_{11}s'_{22})^{1/2} + s'_{12}\right]_{\#2}}{\sqrt{H_{11}H_{22}}}, \tag{3}$$

the parameters H_{11} and H_{22} are given in appendix B.

The crack opening components, Δu_n, are defined from the displacement u_n of two material points coinciding in the un-deformed state

$$\Delta u_n = u_n(r, \theta = \pi) - u_n(r, \theta = -\pi),$$

where the subscript n takes the values 1 and 2, that refers to the coordinate direction x_n in Figure 2. The crack opening components are related to the complex stress intensity factor, K, through

$$\sqrt{\frac{H_{11}}{H_{22}}}\Delta u_2 + i\Delta u_1 = \frac{2H_{11}}{\sqrt{2\pi}} \frac{K_r^{i\epsilon+1/2}}{(1+2i\epsilon)\cosh(\pi\epsilon)}, \tag{4}$$

and the energy release rate can be related to the complex stress intensity factor through

$$G = \frac{H_{11}}{4\cosh^2(\pi\epsilon)} |K|^2. \tag{5}$$

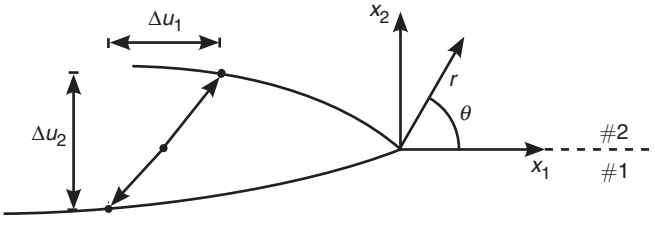

Figure 2. *Definition of crack face opening components.*

The mode mixity is defined as

$$\psi = \tan^{-1} \frac{\Im(K l^{i\epsilon})}{\Re(K l^{i\epsilon})}, \tag{6}$$

where l is a characteristic length parameter, and $\Im$ and $\Re$ are the imaginary and the real part of the complex number. The use of $l^{i\epsilon}$ in the definition of ψ is a mathematical necessity and a discussion on choosing the parameter l is elsewhere [9]. In the present work, l is set equal to the height of the core h, whereby the equations are cast in a neat form. It has been argued that l should be set equal to some characteristic length scale in the materials, e.g., the average cell diameter of the core material. One could argue that the choice of a length related to the microstructure would be more obvious in the present case, since the skin height is different from structure to structure but the microstructure of, e.g., the foam is the same [9]. On the other hand, the choice has no great importance since mode mixity calculated with $l = l_1$ can easily be recalculated to $l = l_2$ [10]. It is important to note that one implication of choosing h as the length scale is that the skin thickness of the specimen should be reported with the test results for a specific sandwich configuration.

ANALYSIS OF SANDWICH

The sandwich analyzed here is defined by the dimensions L, a, H, and h. For the subsequent derivations we ensure that the ends of the specimen, where the loads are applied, are governed by a stress field that is unaffected by stress effects from the crack tip. This can be ensured by making $(L - a)$ and a suitably long, so only the stress fields introduced by the loads M_n, P_n, $n = 1 \ldots 3$ are present at the ends of the sandwich. A finite element analysis has shown that for sandwich materials with extreme elastic mismatch $(L - a)/H > 30$ and $a/h > 1$ ensures that the stress effects from the crack do not reach the ends [11]. For the material combinations used here $(L - a)/H > 10$ and $a/h > 1$ are sufficient.

Reduced Problem

From static equilibrium it is realized that two of the six loads P_n, M_n, $n = 1 \ldots 3$ are statically determined and only four loads characterize the loading.

Since, only the stress components, σ_{12} and σ_{22}, are singular near the crack tip, the singularity is not altered if superimposing stresses in the x_1-direction.

By superimposing a stress field corresponding to an intact sandwich loaded by the moment $-M_3$ and the force $-P_3$ we arrive at a reduced problem where the singular stress components at the crack tip are as in the original problem. The superposition is illustrated in Figure 3. The relations between the reduced load parameters M and P and the original loads, P_n, M_n, $n = 1 \ldots 3$ are

$$\begin{aligned} P &= -P_1 + C_1 P_3 + \frac{C_2 M_3}{h} \\ M &= -M_1 + C_3 M_3, \end{aligned} \tag{7}$$

where C_1, C_2, and C_3 are constants only dependent on elasticity and geometry. The constants are to be found in closed form in appendix C. This result is important since we now only have to determine the singularity in terms of G and ψ for all combinations of P and M instead of all combinations of P_n, M_n, $n = 1 \ldots 3$.

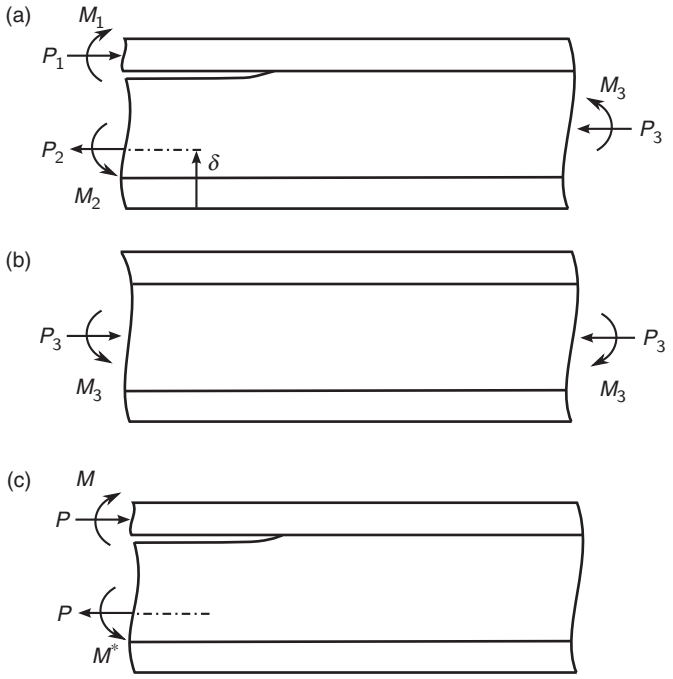

Figure 3. *By super imposing the stress field in (b) on the stress field in (a) the situation in (c) is found, where $M^* = Ph\xi + M$ and ξ is given in the appendix.*

Energy Release Rate

The energy release rate is determined by evaluating the J-integral [11] along the external boundary of the specimen. The linear elastic fracture mechanics is assumed valid and therefore $J = G$. The stresses along the boundary are needed for calculating J and they are accurately modeled by simple beam theory. Note that since the sandwich specimen is loaded only by pure moments and axial forces, there are no shear stresses in the beams and the beam slenderness condition is eliminated.

The energy release rate of the reduced problem (Figure 7c) is determined in closed form

$$G = \frac{(s'_{11})_{\#2}}{2B^2}\left(\frac{P^2}{hU} + \frac{M^2}{h^3 V} + \frac{PM}{\sqrt{UV}h^2}\sin\gamma\right), \tag{8}$$

where U, V, are γ are dimensionless constants dependent only on stiffness and geometry. They are given in appendix A. $(s'_{11})_{\#2}$ is the compliance parameter s'_{11} for material #2, the skin material, see Equation (1). B is the width of the specimen.

The energy release rate resulting from the loadings analyzed here is independent of the crack length for a fixed load. This is the case because the specimen is a steady-state specimen, i.e., as the crack advances in a self similar fashion, the crack tip stress field merely translates along the specimen. However, this is not the case if we imagine a moment introduced by a transverse force T. Then, the moment just ahead of the crack tip would be $M = aT$ and G would be increasing for a fixed load since G would contain a factor a^2.

Mode Mixity

By combining (4), (5), (6), and (8), while setting $l = h$ the mode mixity is, upon some manipulation, expressed as

$$\tan\psi = \frac{\lambda\sin\omega - \cos(\omega+\gamma)}{\lambda\cos\omega - \sin(\omega+\gamma)}, \quad \lambda = \sqrt{\frac{V}{U}}\frac{Ph}{M}, \tag{9}$$

which is valid for $M \neq 0$. For the special case where $M = 0$ we get $\psi = \omega$. ω is a load-independent phase angle that must be determined by numerical means. ω only depends on the geometry and the compliance parameters.

However, once ω is known for one load combination, the mode mixity for any load combination can be calculated by first calculating the reduced loads according to (7) and inserting these in (9).

EXTRACTING THE MODE MIXITY FROM A FINITE ELEMENT SOLUTION

The Crack Surface Displacement Extrapolation Method

The mode mixity can only be calculated fully analytically for very simple load cases and geometries. In the general case, the mode mixity for a sandwich cannot be found analytically. Therefore, a numerical method must be deployed. In the literature several methods have been proposed for calculating the mode mixity. Suo and Hutchinson [13] were among the first to determine the mode mixity by a numerical method, however, later on more straightforward methods have been proposed [14,15]. We use a simple and yet accurate method whereby the mode mixity can be found from a finite element solution of the problem. The method is general and not restricted to the load cases introduced in Figure 1. The method we use is a crack surface displacement extrapolation (CSDE) method [8,11]. In [11], results obtained by the method were compared with results from [13] and the deviations were insignificant in the context of experimental work.

The CSDE method calculates the mode mixity, ψ, from nodal displacements along the crack faces and extrapolates the found values to the crack tip ($r \to 0$). By combining (4) and (6), it is found that ψ in radians is related to the crack surface displacements via

$$\psi = \left|_{r\to 0} \tan^{-1}\frac{\Delta u_1}{\Delta u_2} + \tan^{-1} 2\epsilon + \epsilon \ln\left(\frac{r}{l}\right), \right. \tag{10}$$

where $r \to 0$ means the value found when extrapolating to $r = 0$.

The extrapolation is performed linearly using a number of nodes in the vicinity of the crack tip. In the present work, we used nodes located in the range $H/100 < r < H/10$.

As a check of the model, G calculated from nodal displacements was compared with the G-value calculated by Equation (8), which is an exact result. By combining (4) and (5), it is found that G is related to the nodal displacements through

$$G = \left|_{r\to 0} \frac{\frac{\pi}{4}(1/2+\epsilon^2)}{rH_{11}}\left(\left(\frac{H_{11}}{H_{22}}\Delta u_2\right)^2 + \Delta u_1^2\right). \right. \tag{11}$$

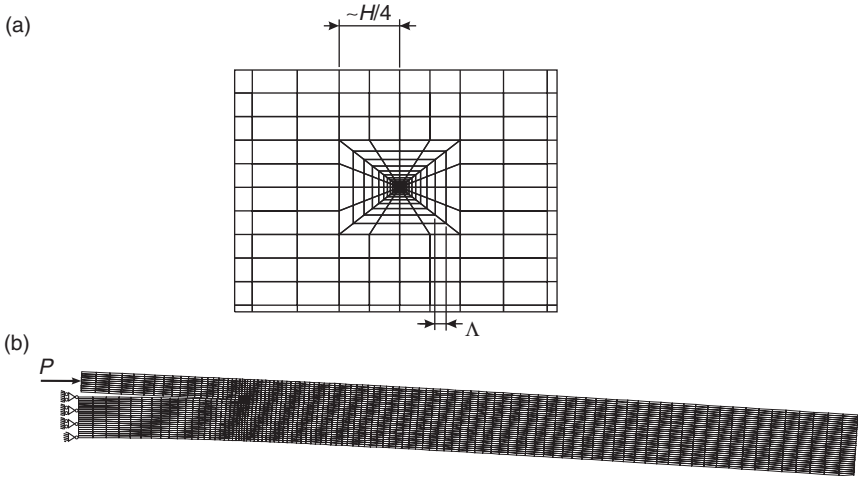

Figure 4. *Loading and mesh used for extracting the mode mixity.*

In all cases the relative deviation between numerical and analytical values was less than 0.005. Furthermore, by comparing the results with results found with meshes having significantly more elements ψ and G calculated by (10) and (11), respectively, were shown to be mesh-independent. Figure 4 shows a typical mesh used for the calculation. In order to resolve the stress and displacement field at the crack tip, the mesh was refined near the crack tip [8,11].

Extracting the Load-independent Phase Angle ω from a Load Case

As described in the section 'Mode mixity', the load-independent phase angle ω should be determined for a single load case for each sandwich structure. Using Equation (10), the mode mixity can be extracted from a finite element solution of the sandwich loaded with any combination of the loads M_n, P_n, $n = 1 \ldots 3$. A convenient choice is to take $P \neq 0$ and $M = 0$ (Figure 4). Then according (9) to $\omega = \psi$.

The following results are found from the finite element calculations with $l = h = 40.0\,\text{mm}$.

Configuration	ω
GFRP/H80	60.2°
GFRP/H130	66.0°

Now, with ω determined we can analytically determine the mode mixity for any combinations of the loads M_n, P_n, $n = 1 \ldots 3$ as follows: First, the force and moment, P and M, of the reduced problem are calculated from (7). Then, by (9), λ and ψ are calculated.

Having completed the stress analysis, we now proceed to the experimental work.

APPLYING THE THEORY TO A TEST SETUP

The theory is now applied to an experimental test setup by which the fracture toughness of sandwich structures can be measured for different mode mixities. Various test setups have been suggested for testing the fracture toughness of sandwich structures, but we think the one used here has a number of advantages that makes it preferable: (i) only one type of specimen is needed to test the whole mode mixity range; (ii) the energy release rate is determined in analytical from (8); (iii) the mode mixity can be determined analytically via (9) when the load-independent phase angle ω is determined; (iv) under fixed/constant loads the energy release rate is independent of the crack length making the measurement of G easy. The only parameters to be measured are the applied moments; it is not necessary to record the crack length to calculate G. The fact that G is independent of crack length also facilitates stable crack growth, since under 'fixed grips' the specimen unloads itself during crack propagation so that G decreases during crack growth.

The double cantilever beam sandwich specimen is loaded by uneven moments via two arms. The test setup is shown in Figure 5. The arms are loaded through a wire/roller system that is loaded by a tensile testing machine. The force, F, is the same all along the wire (apart from the neglectable resistance from the rollers), and thus the moments are calculated by $M_1 = (\pm)F\ell_1$ and $M_2 = (\pm)F\ell_2$. The magnitudes of the moments relative to each other are changed by changing the arm lengths ℓ_1 and ℓ_2. The signs of the moments are changed by rearranging the wire as shown in Figure 5(a1) and 5(a2). The un-cracked end of the specimen is supported by a roller system that provides a moment $M_3 = M_1 - M_2$. A more detailed description of the test method can be found in [16].

The length of the specimens, L, was 300 mm and the initial debond was approximately 70 mm. The sandwich specimens were initially loaded by a moment M_1 ($M_2 = 0$) supported by M_3 ($= M_1$) until the crack had grown approximately 15 mm. This procedure was used for all specimens to ensure that they had the pre-crack introduced in the same manner.

The test setup was used measuring the fracture toughness for the two sandwich types. Twelve specimens were tested for each sandwich type.

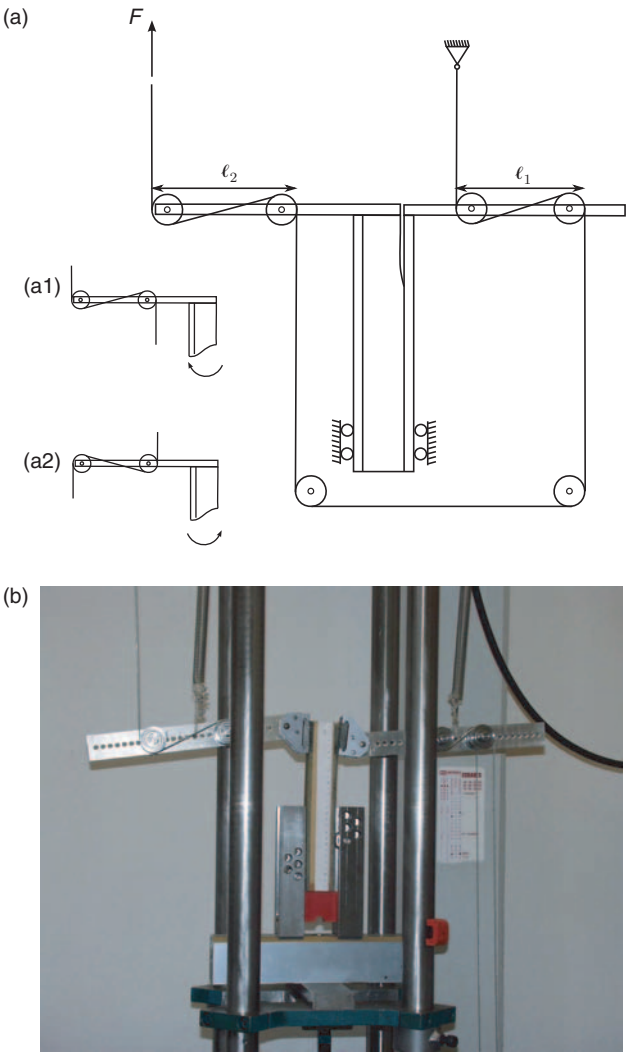

Figure 5. *(a) Sketch of the test setup. (a1) shows the arrangement of the wires that gives $M_2 > 0$ and (a2) shows the arrangement of the wires that gives $M_2 > 0$ (b) Test setup with a specimen mounted.*

The load F was measured by a 5 kN load cell and recorded on a computer with data acquisition. The tests were carried out under low displacement rate so each test had a duration of approximately 2–3 min.

The applied G was computed from the analytical expression (8) with the reduced load parameters P and M calculated from (7). Let us emphasize

that (8) and (7) are derived for a more general load situation where normal forces are applied in combination with moments. In this test method only moments are applied and we simply set the normal forces equal to zero, $P_n = 0$, $n = 1 \ldots 3$ when computing the reduced loads M and P. The mode mixity ψ was calculated by inserting the moments M_1, M_2, and M_3 $(= M_1 - M_2)$ in (7) and (9) (again with the normal forces equal to zero, $P_n = 0$, $n = 1 \ldots 3$).

TEST RESULTS

For mode mixities corresponding to deformation dominated by normal crack opening ($-35^\circ < \psi < -15^\circ$) the fracture behavior was the following: the crack initiated from the pre-crack and shifted hereafter between slow and stable growth and propagation by jumps of 10–20 mm. The crack was either in the core material or, in some cases, in the interface between skin and core. For this loading the crack grew parallel with the skin without deflecting towards the core or the skin. Schematics of the crack deformation and crack path under various load situations are shown in Figure 6.

Representative loading curves for $\psi = -30^\circ$ and -45° are shown in Figure 7. For the specimen loaded under $\psi = -30^\circ$ the load increased almost linearly with time apart from a few minor kinks that was not accompanied by any visual changes of crack length. At some critical load value, a major load drop occurred. This was accompanied by a 10–20 mm unstable crack propagation along the skin/core interface. Hereafter, the load again increased and propagation occurred at almost the same load level. Under this kind of loading the load value at each crack propagation was used as a data point and e.g., the curve for $\psi = -30^\circ$ in Figure 7 gave four data points.

When the deformation was dominated by tangential opening, corresponding to mode mixities below -35°, another behavior was observed. The crack grew into the CSM layer as sketched in Figure 6(a). Initially one to two unstable crack propagations were seen. Thereafter, a higher load level was needed to make the crack propagate. The following crack propagation was slow, stable, and the growth was accompanied by fiber bridging, i.e., fibers that were bridging from one crack face to the other. As shown in Figure 7, the load curve for $\psi = -45^\circ$ indicated a significant increase in fracture resistance (indicated by ΔP_{FB}) after the first onset of growth. Prior to fiber bridging, each point at the onset of crack growth was used as a (triangular) data point. As fiber bridging sets in, only the maximum load achieved was used as a (circular) data point. Figure 7 shows where these data points are taken from on the load curve.

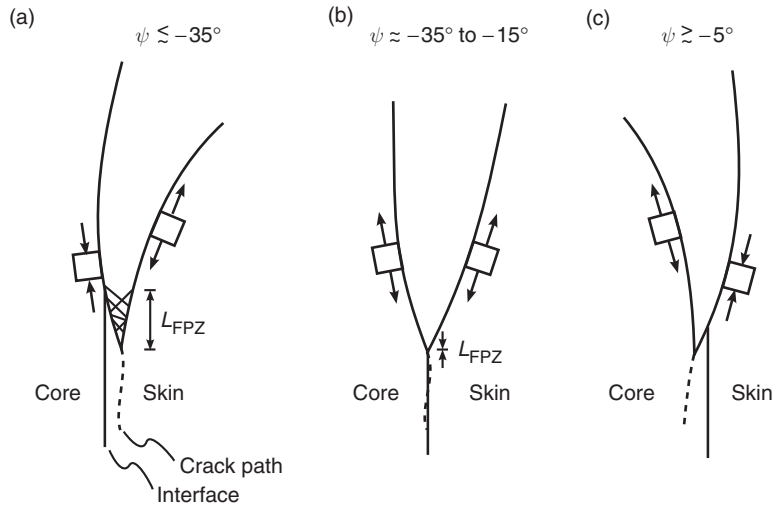

Figure 6. *Schematics of the relationship between mode mixity and crack path selection observed in the tests.*

A few test were also made with mode mixities near $-5°$, but here the crack kinked and grew at a distance into the core where it found a stable path (Figure 6(c)). For even larger mode mixities the crack deflected to the opposite side of the core. Crack kinking and stable crack paths are discussed in detail elsewhere [17], but are beyond the scope of this work.

The fracture resistance measured as a function of the mode mixity is shown in Figure 8(a) and 8(b). The left side of the graphs corresponds to a crack deformation mode where the crack is dominated by tangential displacement with a local elongation of the skin, as illustrated in Figure 6(a). The right side corresponds to a deformation mode where the crack opening is dominated by normal displacement (Figure 6(b)). The data points are segregated into two types. The triangular data points indicate applied energy release rate values at the onset of crack growth or values at crack propagation where no fiber bridging was observed from eye inspection (Figure 7). The fiber bridging mechanism will be discussed in some detail later. The data points indicated by filled circles represent maximum values of the fracture toughness in the cases where an increase in fracture resistance was seen due to e.g., fiber bridging (Figure 7). The thick line in Figure 8(a) is a numerical 'best fit' of a fourth-order polynomium to the initiation results. In Figure 8(b) second order polynomium is used for fitting. The thin lines in both figures are added 'by eye' and they show that the initiation results are spread around a band of approximately constant width.

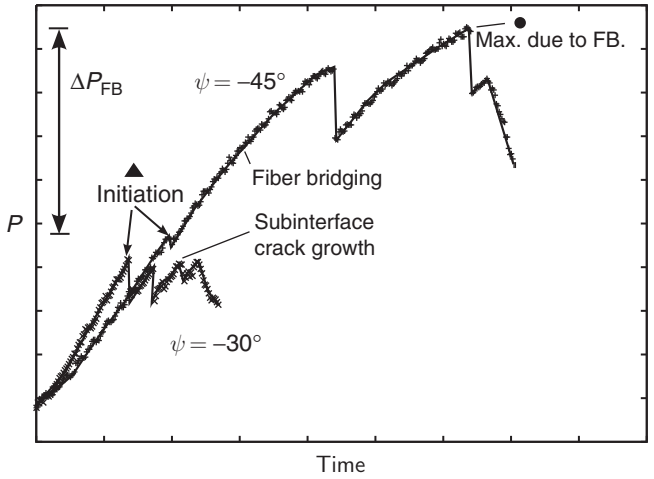

Figure 7. *Two distinctively different loading curves for tests dominated by normal opening ($\psi = -30°$) and tests dominated by tangential opening ($\psi = -45°$), respectively.*

DISCUSSION

From the measurements presented in Figure 8 it is seen that under loadings dominated by tangential crack deformation $\psi \lesssim -35°$ the maximum value of the fracture toughness is significantly higher than the initiation value. For some other loading conditions $\psi \gtrsim -35°$ no increase in fracture toughness is seen at all. To gain insight in the complex fracture behavior of the sandwich materials the subsequent section will discuss the mechanisms taking place under fracture.

When the sandwich specimen is loaded in normal crack opening, the crack grows just below the interface in the core material (Figure 9). The crack growth in the core is not associated with any noticeable increase in toughness as the crack progresses and by eye-inspection the fracture process zone seems to be small, i.e., the fracture process zone is much smaller than the skin thickness. The fact that the fracture process zone is small is important. Then, the application of LEFM is valid, since LEFM is based on the premise that length of the fracture process zone is small compared with all other geometric dimensions of the sandwich (h, H) [18]. For both types of the sandwich tested in the present study, the fracture toughness values are almost constant within the mode mixity range $-10°$ to $-30°$. For the sandwich specimen with H80 core, the applied G at crack initiation (indicated by the curve fit in Figure 8(a)) was also constant when moving further towards tangential crack opening. For the sandwich specimen

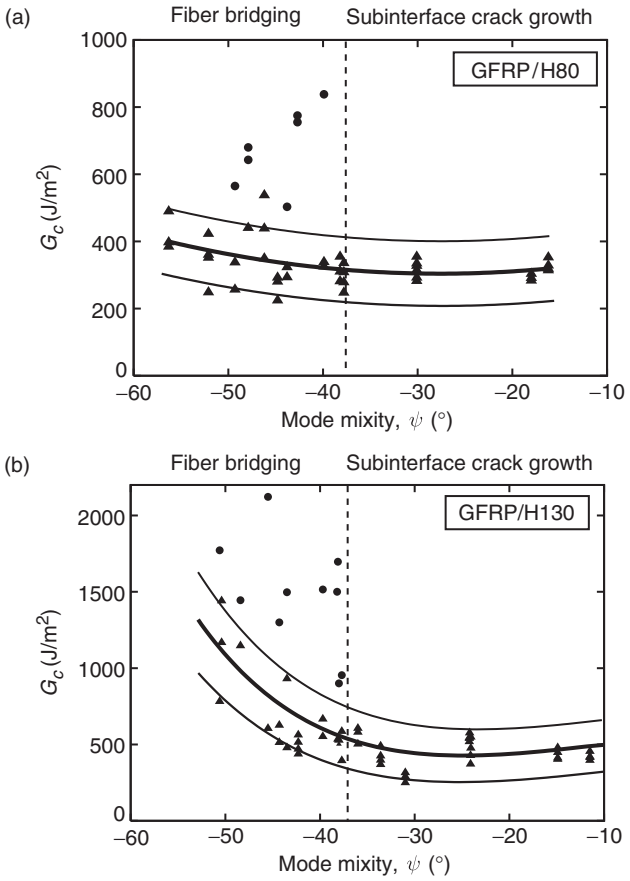

Figure 8. *The measured fracture toughness as function of mode mixity. (a) Shows the fracture toughness as function of mode mixity for the sandwich configuration with GFRP skin H80 core and (b) GFRP/H80.*

with H130, an increasing trend was apparent as applying a larger negative mode mixity. The increasing initiation toughness for H130 is a tendency also seen for other material combinations. Experimental investigations by Liechti and Chai [5] showed that for a glass/epoxy interface the toughness could increase by a factor of 10. The phenomenon has been extensively studied and Tvergaard and Hutchinson [19] showed that in an interface between elastic plastic solids the energy uptake in the plastic zone increased significantly for tangential crack deformation. Other sources for the increasing toughness is friction by asperity contact and locking near the crack tip [5,20]. The formation of the crack branches might also

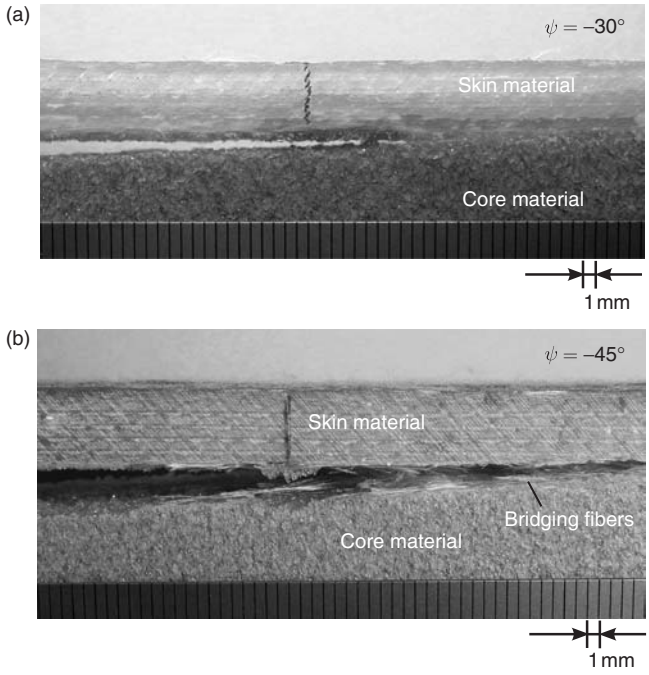

Figure 9. *(a) When the specimen has been loaded with normal crack opening, the crack grows just below the interface in the core material and (b) when the tangential crack deformation is the loading, extensive fiber bridging develops in the interface.*

explain an increased toughness. However, a detailed study to reveal which mechanisms account for the increase in toughness is beyond the scope of this work.

The observation that the crack is growing towards the skin layer for loadings giving tangential crack deformation (Figure 6(a)) can be understood from an analysis of the stresses in front of the crack tip. Under dominated normal crack opening the largest principal stress is approximately perpendicular to the interface and the crack prefers to grow just below the interface. It is well known [21] that in a homogenous material, a crack selects a mode I path, i.e., it propagates in the direction perpendicular to the largest principal stress. As the mode mixity becomes more negative, higher shear stresses arise at the crack tip. At some point the shear stresses reaches a level where crack growth in the interface becomes preferable. With a further decrease in ψ, the crack turns away from the interface and propagates into the skin laminate. The growth in the outer layer of the skin laminate leads to extensive fiber bridging and results in an increasing toughness. From Figure 9 it is clear that the length of the fracture

process zone is increasing to a length several times the skin height whereby a large scale fracture process zone is present. As mentioned, the simple LEFM is not valid for this kind of problem [18] and the results must be interpreted with caution. Fortunately, the right-hand side of (8) was derived using the *J*-integral which is also valid for large-scale bridging problems [18]. Consequently, the circular data points in Figure 8 can be interpreted as the total amount of energy dissipated per unit area in the failure process zone. However, the mode mixity loses its validity as the fracture process zone becomes longer than the zone where the singular stress field dominates. Furthermore, the fibers bridging exert forces on the crack faces and change the mode mixity.

Based on the observations here, it is clear that advanced modeling of crack growth in sandwich structures calls for more advanced modeling approaches that do not have the limitations of the LEFM e.g., cohesive zone modeling [22–24] or modeling using bridging laws and retaining a crack tip singularity [25].

The results in Figure 8(a) and 8(b) exhibit a significant spread. For initiation values the spread was in the order $200\,\mathrm{J/m^2}$. For the data points where fiber bridging was present the spread was much larger. These fracture property variations could be explained by spatial material property variation.

The literature contains many results where interfacial fracture toughness has been measured for different structures. However, the fracture toughness appears to be very sensitive to the exact choice of materials. Ratcliffe and Cantwell [3] measured the fracture toughness of a number of different configurations and found values ranging from 170 to $2750\,\mathrm{J/m^2}$. For a sandwich specimen with a H80 core, various test methods gave an average fracture toughness of approximately $270\,\mathrm{J/m^2}$. In the present study the fracture toughness values for loading under dominated normal crack opening were approximately $300\,\mathrm{J/m^2}$. The discrepancies between our results and those of Ratcliffe and Cantwell [3] are reasonably small and can be attributed to the dissimilarity in manufacture process and differences in the skin lay-up.

CONCLUSION

The test carried out in this work on sandwich double cantilever beam specimens loaded with uneven bending moments showed that the fracture toughness of sandwich structures are strongly dependent on the mode mixity. For $\psi < -35^\circ$ extensive fiber bridging results in rising fracture toughness. For the sandwich specimens tested here fiber bridges formed but a large spread in maximum toughness was seen.

For future work it is suggested that the mechanism of fiber bridging is investigated so the ability to fail by fiber bridging formation is designed into the sandwich structures since this will result in a more fracture-resistant structure.

ACKNOWLEDGEMENTS

Part of this work was part of the SaNDI (THALES JP3.23) project with participants from Norway, Denmark, Sweden, Finland, and the United Kingdom. The support of the five participating nations is gratefully acknowledged. BFS was supported by the Danish Energy Authority under the Ministry of Economics and Business Affairs through a EFP2005-fund (journal no. 33031-0078).

APPENDIX A

Relation between Compliance Matrix and Engineering Constants

Relation between engineering constants and the compliance matrices for a orthotropic and a isotropic material, respectively [26]:

$$s_{ij} = \begin{bmatrix} \frac{1}{E_{11}} & -\frac{\nu_{21}}{E_{22}} & -\frac{\nu_{31}}{E_{33}} & 0 & 0 & 0 \\ -\frac{\nu_{12}}{E_{11}} & \frac{1}{E_{22}} & -\frac{\nu_{32}}{E_{33}} & 0 & 0 & 0 \\ -\frac{\nu_{13}}{E_{11}} & -\frac{\nu_{23}}{E_{22}} & \frac{1}{E_{33}} & 0 & 0 & 0 \\ 0 & 0 & 0 & \frac{1}{G_{23}} & 0 & 0 \\ 0 & 0 & 0 & 0 & \frac{1}{G_{31}} & 0 \\ 0 & 0 & 0 & 0 & 0 & \frac{1}{G_{12}} \end{bmatrix} \tag{A1}$$

$$s_{ij} = \frac{1}{E} \begin{bmatrix} 1 & -\nu & -\nu & 0 & 0 & 0 \\ -\nu & 1 & -\nu & 0 & 0 & 0 \\ -\nu & -\nu & 1 & 0 & 0 & 0 \\ 0 & 0 & 0 & 2(1+\nu) & 0 & 0 \\ 0 & 0 & 0 & 0 & 2(1+\nu) & 0 \\ 0 & 0 & 0 & 0 & 0 & 2(1+\nu) \end{bmatrix} \tag{A2}$$

APPENDIX B

Constants for Fracture Mechanical Equations

The orthotropic materials constants $H_{11}$and H_{22} are given by

$$H_{11} = \left[2m\widehat{\lambda}^{1/4}s'_{11}s'_{22}\right]_{\#1} + \left[2m\widehat{\lambda}^{1/4}s'_{11}s'_{22}\right]_{\#2} \tag{A3}$$

and

$$H_{22} = \left[2m\widehat{\lambda}^{-1/4}s'_{11}s'_{22}\right]_{\#1} + \left[2m\widehat{\lambda}^{-1/4}s'_{11}s'_{22}\right]_{\#2}, \tag{A4}$$

where $m = \sqrt{(1+\rho)/2}$,

$$\widehat{\lambda} = \frac{s'_{11}}{s'_{22}} \tag{A5}$$

and

$$\rho = \frac{2s'_{12} + s'_{66}}{2\sqrt{s'_{11}s'_{22}}}. \tag{A6}$$

APPENDIX C

Stiffness-geometry Constants

The parameters that are used in the construction of the reduced problem are

$$\Sigma = \frac{(s'_{11})^{\#2}}{(s'_{11})^{\#1}}, \qquad \eta = \frac{h}{H}. \tag{A7}$$

Note that all the following constants only depend on these two parameters.

$$C_1 = \frac{1}{A_3\eta}, \qquad C_2 = \frac{1}{2I_3}\left(\frac{1}{\eta} + \frac{1}{\eta^2}\right), \qquad C_3 = \frac{1}{12I_3\eta^3},$$

where

$$\xi = 1 + \frac{3}{2\eta} - \Delta$$

and

$$A_1 = \frac{1}{\eta}, \qquad I_1 = \frac{1}{12\eta^3},$$

$$A_2 = \frac{1}{\eta + \Sigma}, \qquad I_2 = \frac{1}{3\eta^3} + \frac{\Delta}{\eta}\left(\Delta - \frac{1}{\eta}\right) + \Sigma\left[\left(\frac{1}{\eta} - \Delta\right)^2 + \left(\frac{1}{\eta} - \Delta\right) + \frac{1}{3}\right],$$

where

$$\Delta \equiv \frac{\delta}{h} = \frac{1 + 2\Sigma\eta + \Sigma\eta^2}{2\eta(1 + \Sigma\eta)}$$

$$A_3 = \frac{2}{\eta} + \Sigma, \qquad I_3 = \frac{2}{3\eta^3} + \frac{1}{\eta^2} + \frac{1}{2\eta} + \frac{\Sigma}{12}.$$

The parameters given in the *J*-integral solution are

$$\frac{1}{U} = \frac{1}{A_2} + \frac{1}{A_1} + \frac{\xi^2}{I_2}, \qquad \frac{1}{V} = \frac{1}{I_2} + \frac{1}{I_1}, \qquad \frac{\sin\gamma}{\sqrt{UV}} = \frac{\xi}{I_2}.$$

REFERENCES

1. Zenkert, D. (1991). Strength of Sandwich Beams with Interface Debondings, *Composite Structures*, **17**: 331–350.
2. Carlsson, L.A. and Prasad, S. (1993). Interfacial Fracture of Sandwich Beams, *Engineering Fracture Mechanics*, **44**(4): 581–590.
3. Ratcliffe, J. and Cantwell, W.J. (2001). Center Notch Flexure Sandwich Geometry for Characterizing Skin-core Adhesion in Thin-skinned Sandwich Structures, *Journal of Reinforced Plastics & Composites*, **20**(11): 945–970.
4. Suo, Z. (1989). Singularities, Interfaces and Cracks in Dissimilar Anisotropic Media, *Proc. R. Soc. Lond. A*, **427**: 331–358.
5. Liechti, K.M. and Chai, Y.S. (1992). Asymmetric Shielding in Interfacial Fracture under In-plane Shear, *Journal of Applied Mechanics*, **59**: 295–304.
6. Toftegaard, H. and Goutianos, S. (2006). Composite Skin Elastic Constants from Monolithic In-plane Specimens and Bonded Out-of-plane Specimens, *Journal of Sandwich Structures and Materials* (in press).

7. Zenkert, D. (1997). *The Handbook of Sandwich Constructions*, Engineering Materials Advisory Services Ltd., UK.
8. Berggren, C., Simonsen, B.C. and Borum, K.K. (2006). Numerical and Experimental Study of Interface Crack Propagation in Foam Cored Sandwich Beams, *Journal of Composite Materials* (in press).
9. Hutchinson, J. and Suo, Z. (1992). Mixed Mode Cracking in Layered Materials, *Advances in Applied Mechanics*, **29**: 63–191.
10. Rice, J.R. (1988). Elastic Fracture Mechanics Concepts for Interfacial Cracks, *Journal of Applied Mechanics*, **55**: 98–103.
11. Østergaard, R.C. and Sørensen, B.F. (2006). Interface Crack in Sandwich Specimens, submitted, *International Journal of Fracture*.
12. Rice, J.R. (1968). A Path-independent Integral and the Approximate Analysis of Strain Concentration by Notches and Cracks, *Journal of Applied Mechanics*, **35**: 376–386.
13. Suo, Z. and Hutchinson, J. (1990). Interface Crack between Two Elastic Layers, *International Journal of Fracture*, **43**: 1–18
14. Beuth, J. (1996). Separation of Crack Extension Modes in Orthotropic Delamination Models, *International Journal of Fracture*, **77**: 305–321.
15. Matos, P.P.L., McMeeking, R.M., Charalambides, P.G. and Drory, M.D. (1989). A Method for Calculating Stress Intensities in Bimaterial Fracture, *International Journal of Fracture*, **40**: 235–254.
16. Sørensen, B.F., Jørgensen, K., Jacobsen, T.K. and Østergaard, R.C. (2006). DCB-specimen Loaded with Uneven Bending Moments, *International Journal of Fracture*, **141**: 163–176.
17. Matteson, R.C., Carlsson, L.A., Aviles, A.V. and Loup, D.C. (2005). On Crack Extension in Foam Cored Sandwich Fracture Specimens, In: *Proceedings of the 7th International Conference on Sandwich Structures*, Aalborg University, Denmark, Springer, Dordrecht, The Netherlands.
18. Suo, Z., Bao, G. and Fan B. (1992). Delamination R-curve Phenomena due to Damage, *J. Mech. Phys. Solids*, **40**(1): 1–16.
19. Tvergaard, V. and Hutchinson, J.W. (1993). The Influence of Plasticity on Mixed Mode Interface Toughness, *J. Mech. Phys. Solids*, **41**: 1119–1135.
20. Evans, A.G. and Hutchinson, J.W. (1989). Effects of Non-planarity on the Mixed Mode Fracture Resistance of Bimaterial Interfaces, *Acta. Metall.*, **37**(3): 909–916.
21. Thouless, M.D. and Evans, A.G. (1990). Comment on the Spalling and Edge-cracking of Plates. *Scripta Metallurgica et Materialia*, **24**(8): 1507–1510.
22. Hutchinson, J.W. and Evans, A.G. (2000). Mechanics of Materials: Top Down Approaches to Fracture, *Acta Materialia*, **48**: 125–135.
23. Tvergaard, V. (1990). Effect of Fibre Debonding in a Whiskers Reinforced Metal, *Mater. Sci. Engng. A*, **125**: 203–213.
24. Jin, Z.H. and Sun, C.T. (2005). Cohesive Zone Modeling of Interface Fracture in Elastic Bi-materials, *Engineering Fracture Mechanics*, **72**(12): 1805–1817.
25. Jacobsen, T.K. and Sørensen, B.F. (2001). Mode I Intra-laminar Crack Growth in Composites – Modelling of R-curves from Measured Bridging Laws, *Composites Part A: Applied Science and Manufacturing*, **32**(1): 1–11.
26. Jones, R.M. (1975). *Mechanics of Composite Materials*, McGraw-Hill, Washington, D.C.

[P3]

International Journal of Solids and Structures **45**, 1264-1282.

Available online at www.sciencedirect.com
ScienceDirect
International Journal of Solids and Structures 45 (2008) 1264–1282
INTERNATIONAL JOURNAL OF SOLIDS AND STRUCTURES
www.elsevier.com/locate/ijsolstr

Buckling driven debonding in sandwich columns

Rasmus C. Østergaard *

Material Research Department, Risø National Laboratory, Frederiksborgvej 399, 4000 Roskilde, Denmark

Received 18 July 2007; received in revised form 31 August 2007
Available online 14 September 2007

Abstract

A compression loaded sandwich column that contains a debond is analyzed using a geometrically non-linear finite element model. The model includes a cohesive zone along one face sheet/core interface whereby the debond can extend by interface crack growth. Two geometrical imperfections are introduced; a global imperfection of the sandwich column axis and a local imperfection of the debonded face sheet axis. The model predicts the sandwich column to be very sensitive to the initial debond length and the local face sheet imperfection. The study shows that the sensitivity to the face sheet imperfection results from two mechanisms: (a) interaction of local debond buckling and global buckling and (b) the development of a damaged zone at the debond crack tip. Based on the pronounced imperfection sensitivity, the author predicts that an experimental measurement of the strength of sandwich structures may exhibit a large scatter caused by geometrical variations between test specimens.

Keywords: Cohesive zone modeling; Fracture; Interface crack; Delamination

1. Introduction

Sandwich structures comprising a low density core and stiff face sheets have become widely used in various engineering areas where low weight is of importance. The core primarily serves as a spacer that keeps the face sheets apart, giving the sandwich structure a high bending stiffness to weight ratio. Moreover, sandwich structures possess a high global buckling resistance when subjected to in-plane compressive loads. These properties make sandwich structures a favorable alternative in applications where weight savings are essential. Wind turbine blades (see Fig. 1), ships, aircraft structures and trains are examples where sandwich structures are used as load carrying elements (Zenkert, 1995; Thomsen, 2006; Herrmann et al., 2006).

Despite its geometrical simplicity, predicting the compressive strength of sandwich structures is complicated since many potential failure modes exist. During the last decades many studies have addressed the strength of sandwich structures. Comprehensive reviews are given in the books by Allen (1969) and Zenkert (1995). A comprehensive experimental study of the compressive strength of sandwich structures was recently conducted by Fleck and Sridhar (2002).

* Tel.: +45 29857668.
E-mail address: rasmus.c.oestergaard@risoe.dk

0020-7683/$ - see front matter © 2007 Elsevier Ltd. All rights reserved.
doi:10.1016/j.ijsolstr.2007.09.005

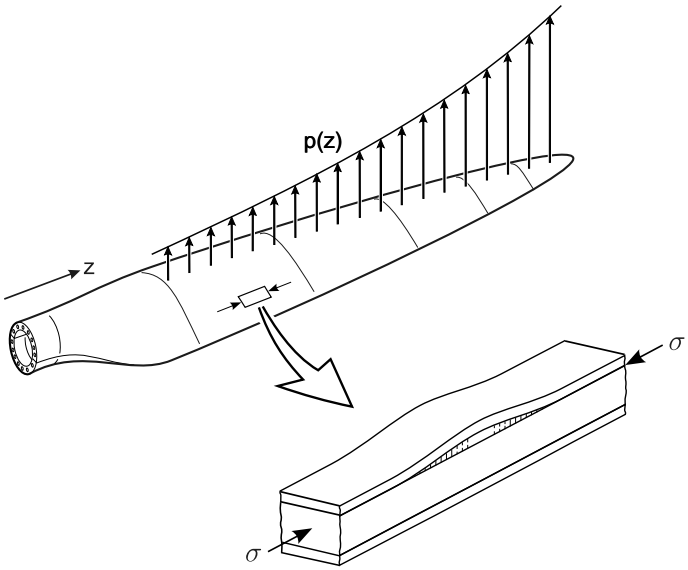

Fig. 1. Application of sandwich structures. In the wind turbine blade sandwich structures are loaded in compression on one side of the blade.

A mechanism that is important to sandwich structures is interaction of buckling modes. For a general engineering structure where more than one buckling mode (e.g., global buckling and a local buckling mode) is critical near the same external load, severe strength reduction may be experienced because the buckling modes can interact with each other. In that case, the structure may also be strongly sensitive to geometrical imperfections; especially imperfections having the same shape as the buckling modes (Van Der Neut, 1973). This is an undesired feature since even very small imperfections can reduce the strength significantly below that of the perfect structure. In sandwich structures different buckling modes can potentially interact with each other and cause a reduction of the compressive strength. Buckling mode interaction in sandwich structures has been modeled by Hunt et al. (1988) using a non-linear, six degree-of-freedom analysis. The results showed that interaction of global buckling with face sheet buckling modes results in an unstable post-buckling behavior that is sensitive to imperfections. Other studies that touch on interaction of buckling modes in sandwich structures include Kim and Sridharan (2005) and Frostig (1998).

Further complexity is added to the problem when the sandwich structure contains a debond (an area between face sheet and core with no bonding) and possible growth of this is considered. In practice, debonded areas in the face sheet/core interface are often encountered. Debonds typically result from errors in the manufacturing process or from impacts on the face sheets during use. In the presence of debonds in the interface, significant reductions of the load bearing capacity can be expected. For debonds above a critical length the strength can be limited by a complex mechanism where the debonded face sheet buckles and triggers an overall collapse. For debonds below a critical length other mechanisms can be limiting (Kwon and Yoon, 1997); for instance, global buckling, face sheet wrinkling, core shear fracture or face sheet fracture. Experimental assessments of the compressive strength of sandwich structures containing debonds are scarce, however a few studies have shown a strong influence of the extent of the debonded region (Jeelani et al., 2005; Zenkert and Shipsha, 2005; Vadakke and Carlsson, 2004). Wadee and Blackmore (2001) and Wadee (2002) extended the Hunt model (Hunt et al., 1988) and studied a sandwich structure with an initial debond that could grow according to a simple fracture mechanics model. Wadee showed that debonding may result in a highly unstable snap-back behavior that has a strong sensitivity to imperfections.

Somers et al. (1992) provides an early analysis of the load bearing capacity of partially debonded sandwich structures. Their model is based on linear elastic fracture mechanics (LEFM) and beam theory. A conclusion from their analysis is that the Euler formula for buckling of a clamped–clamped beam, with a length equal to the debond length, can be used as a first order approximation of the local debond buckling. However, recent

developments in fracture mechanics regarding composite materials have shown that LEFM is unable to describe some important phenomena in composite structures (Bao and Suo, 1992). LEFM assumes that the extent of the energy dissipating zone at the crack tip is small compared to other dimensions (e.g., laminate thickness). Many composites fail under formation of a large fracture process zone. This typically consists of a bridging mechanism such as fiber bridging. In these cases the use of LEFM is inappropriate. A comprehensive discussion of large scale bridging is given by Bao and Suo (1992).

A large scale fracture process zone can be modeled by cohesive zone modeling. Cohesive zone modeling (CZM) reaches back to Barenblatt (1959) and Dugdale (1960) but numerical implementation of the concept was pioneered by Needleman (1987). Since then CZM has become a widespread method for modeling fracture in composite structures (Hutchinson and Evans, 2000; Legarth, 2004b; Li et al., 2005; Blackman et al., 2003). CZM is a more detailed way of considering fracture since it can incorporate microscopic details of the actual fracture process taking place. In the present study, we propose a model of a partially debonded sandwich structure that is based on cohesive zone modeling.

Several experimental studies have determined interfacial fracture toughness and interface fracture mechanisms for sandwich structures (Cantwell et al., 1999; Prasad and Carlsson, 1994; Østergaard et al., 2006). Nevertheless, a full determination of the interface fracture properties in terms of cohesive law has not been done yet. Depending on processing techniques, specimen dimensions, loading and materials the debonding mechanisms change: Some sandwich structures fracture through a brittle fracture process where the crack propagates just below the interface, in the core material. Other sandwich structures fracture at the interface if this constitutes a weak plane. Yet another fracture mechanism is fiber bridging, where the crack tip propagates in an interlayer between the face sheet and core. When the crack propagates in this layer pronounced fiber bridging is seen and a large scale fracture process zone develops (Østergaard et al., 2006). This variation in the type of fracture can be modeled by CZM since both small and large process zones can be represented.

Based on the studies described above, a schematic overview of some potential failure modes relevant to the present study can be provided. Only the initiating failure mode is considered—in practice, other failure mechanisms will cause the ultimate collapse (e.g., face sheet fracture after onset of global buckling). Fig. 2 sketches equilibrium deformation-paths as axial compressive force, P, versus end-displacement, ΔL for:

- (I) A sandwich column that buckles in the global buckling mode (without interaction with any local buckling modes). This structure has a deformation-path similar to an Euler-column, see curve I in Fig. 2. In an experimental context, such a sandwich structure will be stable in load-control (monotonically increasing load) if the load increments are sufficiently small. However, when the slope of the curve becomes horizontal equilibrium cannot be maintained because even a very small load increase will cause large deflections.
- (II) A sandwich column that collapses under buckling-interaction (e.g., interaction between the global buckling mode and face sheet wrinkling). Such a structure may exhibit an unstable behavior (Hunt et al., 1988). A typical load versus end-displacement plot is curve II in Fig. 2; after a maximum load has

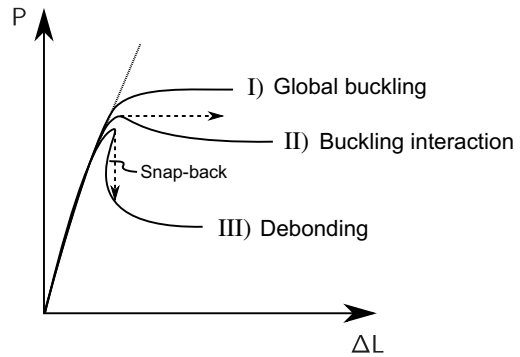

Fig. 2. Equilibrium paths for a compression loaded sandwich structure, illustrating different collapse modes.

been reached, the load decreases. In this case, load-control will result in a dynamic collapse possibly following the dashed line. However, if the loading is displacement-controlled (monotonically increasing end-displacement) the collapse will follow the equilibrium deformation-path in a stable manner.

- (III) A partially debonded sandwich structure where the debond can extend by interface fracture. As shown by Wadee (2002) snap-back can occur. Consequently, unstable collapse can be expected either if the load or the end-displacement is monotonically increasing. In a practical situation where such a sandwich column is displacement-controlled, the deformation-path would follow the dashed line in an unstable manner.

The initial post-buckling path is important since this relates to imperfection sensitivity of the structure: Sandwich structures that possess a stable deformation-path (like path I in Fig. 2) are not sensitive to imperfections. In contrast, for the buckling-interaction and the debonding (path II and path III in Fig. 2) sensitivity to certain imperfections exists.

In the present study we model a compression loaded symmetric sandwich column containing a debond located at the mid-span of the column. Both face sheets and core material are taken to be isotropic. Compared to the model by Wadee (2002), we apply a large strain finite element model and include a cohesive zone to model fracture. The FE method is a very adaptable method and, for later studies, other material models are easily incorporated, e.g., orthotropy of face sheets, plasticity in the core, etc. Furthermore, CZM constitutes a detailed representation of a fracture process. With the CZM we can study details of the fracture process and understand how specific types of fracture mechanisms influence the strength of partially debonded sandwich columns. The present analysis includes the effects of two simple geometrical imperfections of engineering relevance; a column axis imperfection and a local imperfection in the debonded face sheet. This will provide an understanding of how imperfections influence the strength of the sandwich column. We obtain solutions in terms of equilibrium-deformation paths.

The paper is organized as follows: First, we define the sandwich structure and introduce a number of non-dimensional parameters that uniquely specify the problem. Then, we introduce the cohesive zone to model the debonding. For the study, we select a single sandwich structure of engineering relevance. First, results are presented for the imperfection sensitivity of the partly debonded sandwich structure in a case where the interface outside the debonded region is perfectly bonded and cannot fracture. Secondly, we outline some aspects of the collapse mechanism when the debond is allowed to extend by interface crack growth. Next, the influences of interface fracture toughness and cohesive zone parameters on the post-buckling behavior is also addressed. Finally, a discussion of the results and concluding remarks are given.

2. Problem formulation

2.1. The sandwich column

In the present study we analyze a sandwich column of length L, which has face sheets with thickness H and core with thickness h (see Fig. 3). Both the face sheet material and the core material are taken to be isotropic and linearly elastic. The face material is defined by the Young's modulus E_f and the Poisson's ratio ν_f and the core material is defined by E_c and ν_c. In terms of non-dimensional parameters, the sandwich column is specified by

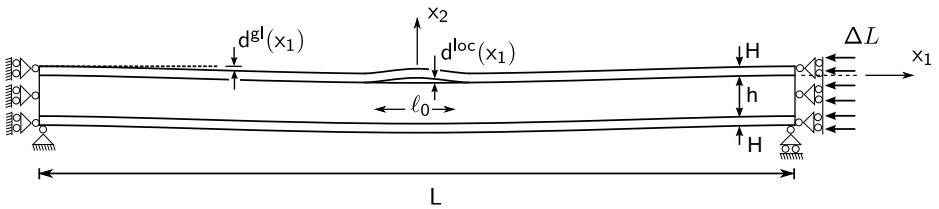

Fig. 3. Specification of the sandwich column.

$$\kappa = \frac{L}{2H+h}, \quad \eta = \frac{h}{H}, \quad \Sigma = \frac{\overline{E}_c}{\overline{E}_f}, \quad \nu_f \quad \text{and} \quad \nu_c, \tag{1}$$

where $\overline{E} = E/(1-\nu^2)$.

The column contains a debonded region of length, ℓ_0, located in the interval $-\frac{1}{2}\ell_0 < x_1 < \frac{1}{2}\ell_0$, $x_2 = 0$ (see Fig. 3). Along one interface ($x_2 = 0$), the interface bonding is represented by a cohesive law. The cohesive law is described in the next section.

The sandwich column has two geometrical imperfections: a global geometrical imperfection, $d^{gl}(x_1)$, of the column axis defined by

$$d^{gl} = d^{gl}_{max} \sin\left(\frac{2\pi x_1}{L} - \pi/2\right), \tag{2}$$

where $d^{gl}_{max} = d^{gl}(x_1 = 0)$ is the imperfection amplitude and a local geometrical imperfection, $d^{loc}(x_1)$ of the debonded face sheet given by

$$d^{loc} = -d^{loc}_{max} \sin\left(\frac{2\pi x_1}{\ell_0} - \pi/2\right), \quad x_1 \in \left[-\frac{\ell_0}{2}, \frac{\ell_0}{2}\right], \ x_2 \geqslant 0, \tag{3}$$

where $d^{loc}_{max} = d^{loc}(x_1 = 0)$ is the local imperfection amplitude.

The perfect beam specified by (1) now has three imperfections specified by the non-dimensional parameters:

$$\alpha = \frac{d^{loc}_{max}}{H}, \quad \beta = \frac{d^{gl}_{max}}{2H+h} \quad \text{and} \quad \xi = \frac{\ell_0}{L}. \tag{4}$$

Owing to symmetry of the problem only one-half of the column, $x_1 \in [0, L/2]$, is modeled; the symmetry line at $x_1 = 0$ is fixed in the x_1-direction. Furthermore, the points $(x_1, x_2) = (L/2, -h-H)$ and $(x_1, x_2) = (0, -h-H)$ are fixed against displacements in the x_2-direction. At $x_1 = L/2$ the sandwich column end is displaced by a uniform, incremental displacement in the x_1-direction. The current end-shortening is denoted $\Delta L = -2v_1(x_1 = L/2, x_2)$.

2.2. Cohesive zone model

The interface between the face sheet and core at $x_2 = 0$ is modeled using a modified version of the Tvergaard–Hutchinson cohesive law (Tvergaard and Hutchinson, 1993), see Fig. 4. The cohesive law specifies the dependence of the tractions σ^I_t and σ^I_n on the displacements u_t and u_n. Here, u_n and u_t are the normal and tangential components of the displacement difference across the interface, while σ^I_n and σ^I_t are the corresponding normal and shear stresses in the interface (see Fig. 4b). Let u^*_n and u^*_t be characteristic values of u_n and u_t and define a non-dimensional damage zone measure as:

$$\lambda = \sqrt{\left(\frac{u_n}{u^*_n}\right)^2 + \left(\frac{u_t}{u^*_t}\right)^2}, \quad u_n \geqslant 0 \tag{5}$$

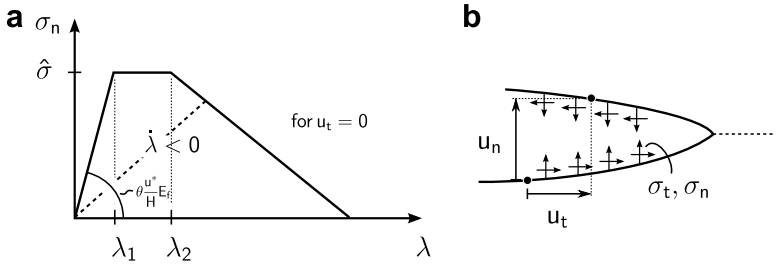

Fig. 4. (a) The normal stress component, σ_n, under pure normal opening. (b) Definitions of the crack face openings.

such that the tractions σ_n and σ_t drop to zero at $\lambda = 1$. Then, as λ is monotonically increasing the tractions in the interface are given by (Tvergaard, 1990):

$$\sigma_n^I = \frac{u_n/u_n^*}{\lambda}\sigma(\lambda) \quad \text{and} \quad \sigma_t^I = \frac{u_t/u_t^*}{\lambda}\frac{u_n^*}{u_t^*}\sigma(\lambda), \tag{6}$$

where $\sigma(\lambda)$ denotes the interface normal stress under pure normal separation ($u_t \equiv 0$). $\sigma(\lambda)$ is given by a trapezoidal shape that starts at $\sigma = 0$ at $\lambda = 0$ and increases linearly to a peak value $\hat{\sigma}$ at $\lambda = \lambda_1$. This stress level is retained until $\lambda = \lambda_2$ where after it decreases linearly to zero. For $0 < \lambda < 1$ this can be written as:

$$\sigma(\lambda) = \begin{cases} \hat{\sigma}\frac{\lambda}{\lambda_1} & \text{for } 0 < \lambda \leqslant \lambda_1 \\ \hat{\sigma} & \text{for } \lambda_1 < \lambda \leqslant \lambda_2\,, \quad \text{for } \dot{\lambda} \geqslant 0 \text{ and } \lambda = \lambda_{\max}, \\ \hat{\sigma}\frac{\lambda-1}{\lambda_2-1} & \text{for } \lambda_2 < \lambda < 1 \end{cases} \tag{7}$$

where $\dot{\lambda} = \frac{\partial\lambda}{\partial u_n}\dot{u}_n + \frac{\partial\lambda}{\partial u_t}\dot{u}_t$ and $\dot{u}_n$ and $\dot{u}_t$ are the increments of u_n and u_t. $\lambda_{\max}$ is the largest λ attained through the loading history. $\lambda = \lambda(x_1)$ constitutes a measure of the state of the interface at x_1: For $\lambda < \lambda_1$ the interface is undamaged. For $\lambda_1 \leqslant \lambda < 1$ the interface is damaged and for $\lambda \geqslant 1$ the interface has fractured.

In order to model non-monotonic opening, a linear unloading (see Fig. 4a) is used to represent the partly damaged interface:

$$\sigma_n^I = \frac{u_n}{u_n^*}\frac{\sigma(\lambda_{\max})}{\lambda_{\max}} \quad \text{and} \quad \sigma_t^I = \frac{u_t}{u_t^*}\frac{u_n^*}{u_t^*}\frac{\sigma(\lambda_{\max})}{\lambda_{\max}}, \qquad \lambda < \lambda_{\max} \text{ or } \dot{\lambda} < 0. \tag{8}$$

To resist face sheet penetration of the core ($u_n < 0$) we use a contact law where the normal stress is calculated according to (6)–(8), but with (6a) and (8a) replaced by

$$\sigma_n^I = k_n u_n, \quad u_n < 0, \tag{9}$$

where k_n is a stiffness constant.

The shear stresses are still given by (6) but with the dimensionless opening parameter defined as

$$\lambda = |u_t/u_t^*|, \quad u_n < 0. \tag{10}$$

In the present study we use:

$$k_n = \frac{\hat{\sigma}_n}{\lambda_1 u_n^*}. \tag{11}$$

The parameters governing the interface law are $\hat{\sigma}$, u_n^*, u_t^* together with the shape factors λ_1 and λ_2. The work of separation per unit area of interface (fracture toughness), Γ, is given by

$$\Gamma = \frac{1}{2}\hat{\sigma}u_n^*[1 - \lambda_1 + \lambda_2]. \tag{12}$$

Equivalently the parameters can be taken as Γ, u_n^*, u_t^*, λ_1 and λ_2. In the present study we use $u_n^* = u_t^* = u^*$. In terms of non-dimensional constants the cohesive law is then specified by

$$\frac{\Gamma}{E_f H}, \quad \frac{u^*}{H}, \quad \lambda_1 \text{ and } \lambda_2. \tag{13}$$

The shape of this cohesive law, (7), was originally suggested to represent the fracture mechanism of ductile metals (Tvergaard and Hutchinson, 1992). Various other cohesive laws exist. For mixed mode interfacial problems (like the present) a variation of the work of separation with opening mode could be included (Chai, 2003; Tvergaard, 1990). However, for simplicity we use a fracture model that has mode mixity independent fracture toughness. This choice is also justified by the fact that the mode mixity for the present problem changes only slightly during the face sheet separation.

2.3. Global buckling of the sandwich column

The global buckling load P^{gl} of a sandwich column is not accurately predicted by the Euler-buckling load. A more accurate solution takes into account shear deformation of the core (Allen, 1969; Fleck and Sridhar, 2002):

$$\frac{1}{P^{gl}} = \frac{1}{P^{E}} + \frac{1}{P^{S}}, \tag{14}$$

where $P^{S} \approx AG$, $A = (h+H)^2/h$, $G = E_c/(1+2\nu_c)$ and P^{E} is the Euler-buckling load

$$P^{E} = \frac{4\pi^2 EI}{L^2}, \tag{15}$$

where $EI = \int_{-h-H}^{H} E(x_2)x_2^2\,dx_2$.

Eq. (14) gives a fairly accurate estimate of the buckling load that is in agreement with numerical results. In-depth discussions concerning global buckling of sandwich structures are found elsewhere (Bazant, 2003; Bazant and Beghini, 2004).

If we recast (14) in a dimensionless framework P^{gl} can be expressed as:

$$\frac{P^{gl}}{HE_f} = \frac{4\pi^2\eta\Sigma}{\eta(\eta+2)^2\kappa^2\Sigma + 4n_c\pi^2 I_0}, \tag{16}$$

where $I_0 = (\eta^3\Sigma + 6\eta^2 + 12\eta + 8)/12$ is a non-dimensional second moment of area and $n_c = 2\nu_c + 1$.

As an approximate measure of the criticality of the two buckling modes we introduce the ratio:

$$R = \frac{\epsilon_{loc}^{cr}}{\epsilon_{gl}^{cr}}, \tag{17}$$

where ϵ_{gl}^{cr} is the average-column-strain, $\Delta L/L$, where global buckling initiates. ϵ_{loc}^{cr} is an estimate of the average-column-strain, $\Delta L/L$, that results in buckling of the debonded face sheet. ϵ_{loc}^{cr} is estimated from the Euler-buckling load of a clamped–clamped column with the same length as the debonded face sheet:

$$\epsilon_{gl}^{cr} = \frac{4\pi^2\Sigma\eta/A_0}{\eta(\eta+2)^2\kappa^2\Sigma + 4n_c\pi^2 I_0}, \tag{18}$$

$$\epsilon_{loc}^{cr} = \frac{\pi^2}{3(\ell_0/L)^2\kappa^2(2+\eta)^2}, \tag{19}$$

where $A_0 = \Sigma\eta + 2$.

According to the conclusions by Somers et al. (1992), $R < 1$ can be used as a rough criterion for predicting in which cases face sheet buckling is observable. We will compare this criterion with the numerical results obtained in this study. Eq. (17) is also used to select sandwich columns for which $R \approx 1$ since those are of primary concern in this study.

2.4. Computational method

The problem defined in the previous section is solved using a large-strain finite element formulation. Eight node isoparametric elements are used. A special Rayleigh–Ritz finite element method has been used to ensure

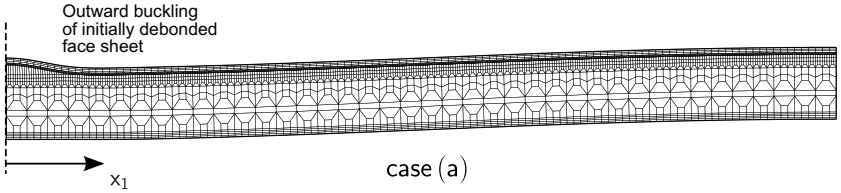

Fig. 5. The sandwich column fails by local buckling of the initially debonded face sheet when $\alpha = 0.01$ and $\beta = 0.01$. The displacements are scaled ×10.

equilibrium solutions, also in the case of snap-back (i.e., when both end-displacement increments and load increments change sign). More details concerning the computational methods can be found elsewhere (Tvergaard, 1990, 1976; Legarth, 2004a). The mesh used for the computations is shown in Fig. 5. A few calculations were carried out using more dense meshes whereby it was shown that the solutions are not mesh-dependent.

3. Results

3.1. Model materials

In the present study we focus on a single model sandwich column that represents a sandwich structure of practical engineering interest. The stiffness parameters of the structure are defined by $\overline{E}_f/\overline{E}_c = 100$ and $\nu_s = \nu_c = 0.3$. The geometry of the structure is defined by $L/(2H+h) = 25$, $\eta = h/H = 8$. The criticality factor, R, (Eq. (17)) for a sandwich column with these parameters has been computed in Table 1 for different crack lengths. The present study will focus on cases where $\ell_0/L \leqslant 0.1$ which, according to (17), is equivalent to $R \leqslant 1.52$.

Unless otherwise mentioned, the following parameters are used for the cohesive law: The fracture toughness of the interface is given by $\Gamma = 10^{-6}E_f H$. The critical separation in the cohesive law is $u_n^* = u_t^* = u^* = H/10$. The initial part of the cohesive law ($\lambda < \lambda_1$, see Fig. 4) gives some artificial compliance to the system, but it is a numerical necessity in cohesive zone modeling (Schellekens and De Borst, 1993). Since the interface initially has zero thickness, u_n and u_t should remain zero until the damage stress ($\hat{\sigma}$) is reached and damage starts to evolve—until that point all deformation should be accommodated by the continuum around the interface. However, in many engineering problems the extra flexibility from the initial part of the cohesive law has only minor influence on the solutions. In connection to the present study, a convergence study showed that the solutions for the actual problem become practically independent the initial part of the cohesive law when the slope, θ (see Fig. 4), fulfills

$$\theta = \frac{\hat{\sigma}}{u^*\lambda_1}\frac{H}{E_f} > 140. \tag{20}$$

Unless otherwise mentioned, the shape parameters are taken to be $\lambda_1 = 0.01$ and $\lambda_2 = \lambda_1 + 0.40$. This choice of λ_1 ensures a cohesive law that fulfills (20) and results in a solution that is practically independent of the initial part of the cohesive law.

As an example consider a sandwich column with face sheets having Young's modulus $E_f = 70$ GPa and thickness $H = 3$ mm. Then, the cohesive zone parameters defined above, correspond to $\Gamma = 210$ J/m^2, $u^* = 30$ μm and $\hat{\sigma} = 1$ MPa (the latter is found from Eq. (12)).

3.2. Imperfection sensitivity for sandwich column with perfectly bonded interface

As an introductory study, we briefly investigate the imperfection sensitivity of a partially debonded sandwich column for the case where the interface outside the debonded region is perfectly bonded. Here, perfectly bonded is defined such that the interface should not be able to open outside the debonded region, i.e., $u_n = u_t = 0$ for $x_1 \notin [-\ell_0/2; \ell_0/2]$. In practice, this is modeled by specifying the cohesive law with extremely high values of Γ and u^*:

$$\Gamma = 10^2 E_f H, \quad u^* = H \cdot 10^7, \quad \lambda_1 = 0.01 \quad \text{and} \quad \lambda_2 = \lambda_1 + 0.4.$$

Table 1
The criticality factor R for different debond lengths

$\frac{\ell_0}{L}$	$R = \frac{\epsilon_{gl}^{cr}}{\epsilon_{loc}^{cr}}$
0.05	0.39
0.075	0.86
0.1	1.52
0.125	2.36

These parameters fulfill (20) so only negligible opening will occur along the interface.

The influence of α, β and ℓ_0/L on the load-carrying capacity is shown in Fig. 6. On the vertical axis is the compressive force per unit width, P, normalized by the buckling load, P^{gl}, predicted by (14). On the horizontal axis is the column-end displacement, ΔL normalized with the column length L. In the preceding, $\Delta L/L$ is referred to as the average-column-strain.

Results for three different crack lengths and various combinations of imperfections are shown. We will now outline the main findings. Taking for instance the case specified with $\ell_0/L = 0.04$, $\alpha = 0.01$ and $\beta = 10^{-5}$, the load increases with increasing end-displacement in a linear manner until the global buckling load is reached near $P/P^{gl} \approx 1$. At the global buckling load a sudden transition into the post-buckling regime appears. Thereafter, continued end-displacement and buckling in the global mode takes place under constant load level (same behavior as for an Euler-column). Identical behavior is seen for a sandwich column with the same debond length and the same column axis imperfection but a larger local imperfection $\alpha = 0.05$. Yet another case has the same initial debond length ($\ell_0/L = 0.04$) and a local imperfection $\alpha = 0.01$ but an increased column axis imperfection, $\beta = 0.01$. In this case, the behavior only differs from the two previous cases in the sense that the transition into global buckling is smoother. For all three cases, mentioned above, the load reaches the global buckling load despite the presence of the debond. This can be explained by studying the openings along the debonded interface $x_1 \in [-\ell_0/2; \ell_0/2]$: The debonded face sheet bends inwards ($u_n < 0$) and gets supported by the core (via the contact law Eq. (9)) and therefore the column practically behaves like an intact sandwich column. In a case with $\ell_0/L = 0.04$, $\beta = 10^{-5}$ and $\alpha = 0.2$ (i.e., a larger local imperfection compared to the three previous cases) the behavior change fundamentally as a study of the openings along the debonded interface $x_1 \in [-\ell_0/2; \ell_0/2]$ shows. For this case, the debonded face sheet buckles outwards ($u_n > 0$). Furthermore, the deformation path now displays a maximum load after which the load decreases monotonically. Consequently, the column would be unstable in load-control, while under displacement control, it would exhibit a stable response.

From Fig. 6 can be concluded that the magnitude of the local imperfection, α, has a large influence on whether the debonded face sheet bends inward or outward. Results not included in Fig. 6 show that the larger the column axis imperfection, β, the larger the local imperfection, α, must be to ensure that the face sheet buckles outward.

Focusing on the influence of the initial debond length, Fig. 6 show results for three debond lengths $\ell_0/L = 0.04$, $\ell_0/L = 0.075$ and $\ell_0/L = 0.1$. The effect of this is strong. From $\ell_0/L = 0.04$ to $\ell_0/L = 0.075$ the maximum achieved load is reduced from approximately $P/P^{gl} = 1$ to approximately $P/P^{gl} = 0.7$. From $\ell_0/L = 0.075$ to $\ell_0/L = 0.1$ the corresponding reduction is only around 0.1. The results also show that the

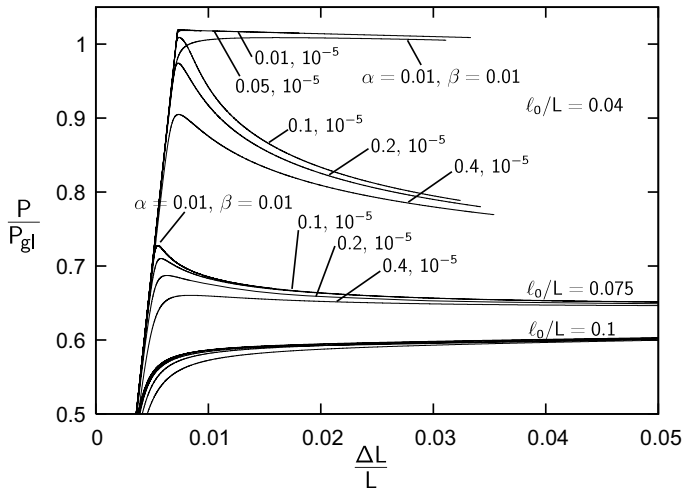

Fig. 6. Influence of the global imperfection parameter β and the local imperfection parameter α on the compressive strength of a sandwich column with infinite fracture toughness of the interface.

curves are located closer together for longer debonds, i.e., the imperfection sensitivity decreases with increasing debond length.

3.3. Imperfection sensitivity—effect of debond crack growth

In this section we study the effect of imperfections on a sandwich column where the interface properties are specified according to Section 3.1:

$$\Gamma = 10^{-6} E_f H, \quad u^* = H/10, \quad \lambda_1 = 0.01 \quad \text{and} \quad \lambda_2 = \lambda_1 + 0.4.$$

For these interface parameters, the cohesive law constitutes a more realistic bonding between the face sheet and the core.

We study the influence of the three imperfections ℓ_0/L, α and β. In the previous section, a brief, introductory, study illustrated that the sandwich column is strongly sensitive to the imperfections and that load-controlled loading of the column would result in an unstable collapse. Furthermore, it was shown that for certain combinations of the imperfections the debonded face sheet buckles outward; and for other combinations the face sheet bends inward and is supported by the core. In this section we will start off by studying two cases that result in outward buckling and inward bending of the face sheet, respectively. The two cases are specified with imperfections given by

- Case (a): $\alpha = 0.01$, $\beta = 0.01$ (outward buckling).
- Case (b): $\alpha = 0$, $\beta = 0.01$ (inward bending).

The initial debond length is chosen as $\ell_0/L = 0.075$ for both cases.

Fig. 7 shows the response of the sandwich columns for case (a) and case (b). On the vertical axis is load, P/P^{gl} and on the horizontal axis is the average-column-strain, $\Delta L/L$. Initially, the force rises in a linear manner for increasing average-column-strain. When the load bearing capacity, P^{cr}, is reached both structures suffer unstable snap-back collapse.

For case (a) the collapse takes place at the same time as the debonded face sheet buckles outward and the interface fractures. Fig. 5 shows the deformed shape of the sandwich column just after the maximum load for the structure was reached. The displacements are exaggerated by a factor of 10. The post-buckling response can be divided into a number of stages as shown in Fig. 7: After the first unstable stage (1. snap-back), where

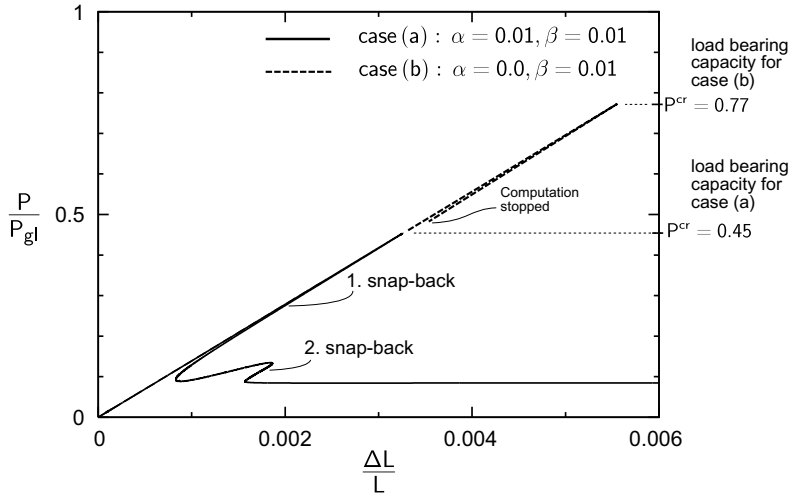

Fig. 7. Load curves resulting from two different combinations of the imperfections. In both cases the columns fails by a snap-back. The sandwich column from case (a) failed by local buckling of the face sheet and the sandwich column from case (b) failed by interface sheer fracture.

debond crack growth initiates, the debond has extended to a length where a load increase is again required for increasing end-displacement. Next, a second unstable collapse (2. snap-back) causes the debond to extend to the ends of the sandwich column. The final part of the response for case (a) consists of a horizontal segment that corresponds to the buckling load of the fully debonded sandwich column.

The circumstances associated with the collapse of the sandwich column in case (b) are different: In this case, the debonded face sheet bends inwards and gets supported by the core. Therefore, the load continues to increase and the sandwich structure is compressed beyond the failure level for case (a) where the face sheet buckled outward. However, due to the geometrical imperfections, deformation in the global mode increases as the global buckling load is approached. This makes shear stresses build up in the interface and eventually interface shear fracture initiates near $x_1 = L/4$. At that point the maximum load (or load bearing capacity), P^{cr}, is also reached. In the following the term load bearing capacity and maximum load are used interchangeably. Hereafter the structure experiences unstable snap-back collapse as seen from the dashed line in Fig. 7 (The computation for case (b) was stopped just after the onset of crack growth). Fig. 8 shows a deformed mesh from case (b) with the displacements scaled ×10. The load carrying capacity for the two structures are quite different; for case (a) $P^{cr}/P^{gl} = 0.45$ and for case (b) $P^{cr}/P^{gl} = 0.77$. However, the results for case (b) will be sensitive to the presence of debonds located near the point where the interface shear fracture initiates ($x_1 \approx L/4$). Therefore, to get a full understanding of failure mode for case (b), an additional imperfection should be included near the shear fracture initiation point. This will however not be pursued in the present paper; here we focus mainly on failure mode seen in case (a).

The transition between the failure modes in case (a) and case (b) takes place over a narrow interval of α and β: For example, with $\ell_0/L = 0.1$ and $\alpha = 0.01$ the failure mode is outward buckling as in case (a) when $\beta = 0.02$. When increasing the column axis imperfection to $\beta = 0.021$ the failure mode becomes as in case (b). Also, inside the window of α and β combinations that result in outward buckling of the face sheet, a significant dependence on the values of α and β is seen. Fig. 9 shows the load bearing capacity, P^{cr}, normalized by P^{gl} versus β for a range of α-values and different initial crack lengths, ℓ_0/L.

Taking for instance, $\alpha = 0.01$ and $\ell_0/L = 0.1$, the load increases slightly in the interval $\beta = 0$ to $\beta = 0.021$. In this range, failure starts by face sheet buckling and debond crack growth, a failure mode as in case (a). At $\beta = 0.021$, the curve displays a rapid rise of the failure load to $P^{cr}/P^{gl} = 0.76$. This rise reflects the shift in the failure mode to failure by global buckling and interface shear fracture (similar to case (b)). For $\beta > 0.021$ failure mode (b) develops and for increasing β ($\alpha = 0.01$ still) the failure load decreases slightly. It is noted that the curve segment corresponding to failure mode (b) is independent of the crack length and of α. This is because the interface failure does not start at the initial debond.

Focusing on the failure associated with outward buckling of the face sheet (the part of the curves located to the left of the jumps in Fig. 9), the sensitivity to α is pronounced; when increasing the face sheet imperfection from $\alpha = 0.01$ to $\alpha = 0.04$ the maximum load, P/P_{gl}, is reduced from 0.93 to 0.66 for a case with $\ell_0/L = 0.05$ and $\beta = 0.0035$. This reduction is much larger than the reduction caused by the column axis imperfection β.

The results in Fig. 9 predict that the buckling load of a perfect column ($\alpha \to 0, \beta \to 0$) is slightly higher than the buckling load, P^{gl}, predicted by (16). This may be explained by higher order effects not captured by (14); for example, as the beam is compressed the Poisson's effect increases the distance between the face sheets, this increases the stiffness and the buckling load of the column. Furthermore, including a shear correction factor (Huang and Kardomateas, 2002) may result in a more accurate prediction. For this study the observed deviation is not important.

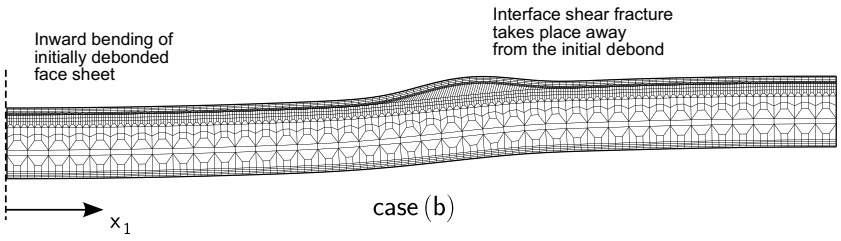

Fig. 8. When $\alpha = 0.0$ and $\beta = 0.01$, the sandwich column initially deforms in a global buckling mode but an interface crack emerges due to the shear stress in the interface. The displacements are scaled ×10.

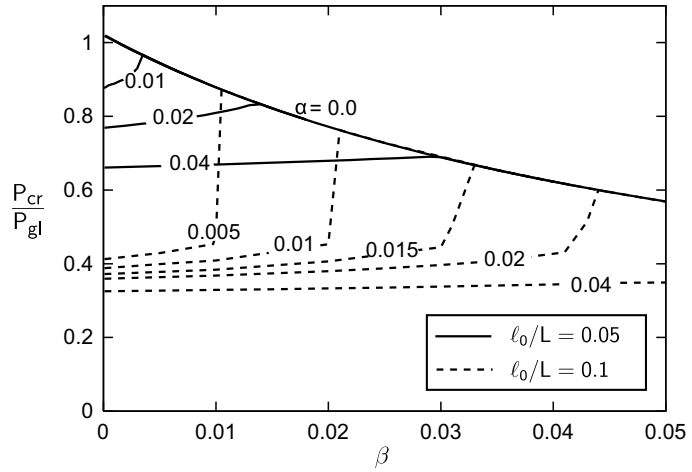

Fig. 9. Influence of the global imperfection parameter β and the local imperfection parameter α on the compressive strength of the sandwich structure.

Another parameter that has a major influence on the load bearing capacity of the sandwich column is the initial debond length ℓ_0/L. Fig. 10 shows the maximum load as a function of the initial debond length. The curves consist of a horizontal line (constant P/P^{gl}) and a decreasing part for increasing ℓ_0/L. When ℓ_0/L is below a critical value (and $\beta = 0$), the load reaches the horizontal line at $P_{cr}/P^{gl} = 0.87$, where interface shear fracture takes place as a result of the global buckling, as in case (b). For ℓ_0/L-values exceeding the critical length, failure mode (a) outward buckling becomes active and the load bearing capacity is rapidly reduced for increasing ℓ_0/L. The critical value of ℓ_0/L is affected by the imperfections α and β as is seen in Fig. 10: When the face sheet imperfection, α, is increased the critical ℓ_0/L decreases. The column axis imperfection, β, has the opposite effect—when this is increased the critical ℓ_0/L-value also increases.

3.4. Detail study at the crack tip

It is of interest to investigate the behavior near the debond crack tip when the fracture process zone is modeled by a cohesive zone. Fig. 11 shows the state of the interface as the sandwich column collapses in a case (a) situation. Compressive load normalized by the global buckling load, P/P^{gl}, is on the vertical axis and the hor-

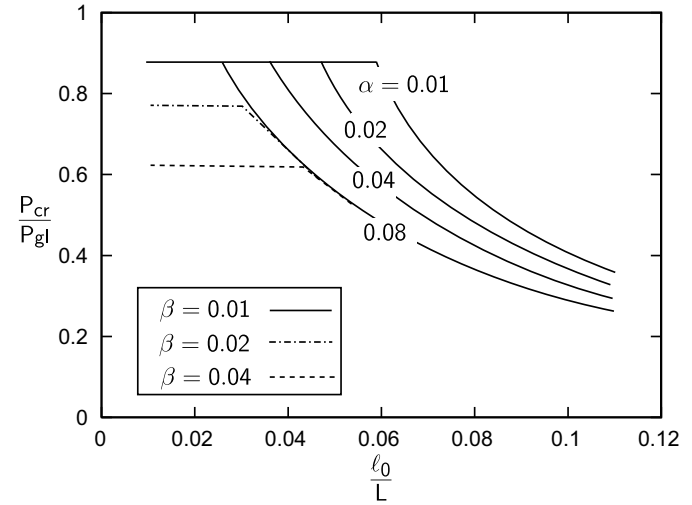

Fig. 10. Relation between crack length and maximum load the column can support.

izontal axis shows the normalized distance to the mid-section, $2x_1/L$. First, focus on the solid line. This represents the correlation between the load and the location of the point in the interface at which damage is just present ($\lambda = \lambda_1$); in front of this point the interface is intact ($\lambda < \lambda_1$). In the initial stage of the loading, the entire interface in front of the initial debond is intact ($\lambda < \lambda_1$) and no damage front is present. When the load reaches $P/P^{gl} = 0.25$, the cohesive element just in front of the debond crack tip ($x_1 = \ell_0/2$) starts to develop damage ($\lambda \geqslant \lambda_1$); therefore, the solid line emerges at $x_1 = \ell_0/2$. As the loading continues the damage front extends forward. At $P/P^{gl} = 0.45$ the load reaches a maximum and starts to decrease while the damage front still continues to move forward. Now focus on the thin dashed line that shows the location of the crack front ($\lambda = 1$). When the load has decreased to $P/P^{gl} = 0.38$, $\lambda = 1$ at the initial crack tip, so that the debond crack tip starts to propagate. The horizontal distance between the solid line and the dashed line represents the current length of the damage zone ℓ_{DZ}. For example, in Fig. 11, the length of the damage zone is $\ell_{DZ} \approx 7H$ at the onset of crack growth and it remains approximately constant in size throughout the collapse. From Fig. 11 it is also seen that throughout the process the damage front and the crack tip propagate continuously forward.

Figs. 9 and 10 have shown that the $P - \Delta L$ relationship is significantly influenced by the local imperfection α. The dependence on the imperfection amplitude α may be attributed to the crack growth mechanism and the development of a damage zone prior to collapse. In order to clarify this we study how α influences what occurs at the crack tip.

In Fig. 12 the horizontal axis is the position of the damage front, x_1/H, and the vertical axis is the load, P/P^{gl}. The lines represent the location of the damage front ($\lambda = \lambda_1$) for different values of α. Taking for instance $\alpha = 0.02$ the damage front starts to form at the debond crack tip at $x_1/H = 18.75$ when $P/P_{gl} = 0.175$. The damage front then moves forward and when it is at $x_1/H = 26$ the maximum load is reached and the load starts to decrease. The results show that, for increasing face sheet imperfection, α, the length of the damage zone at the maximum load, $\hat{\ell}_{DZ}$, increases. At the same time the maximum load the column can carry decreases. A physical explanation of this behavior is now proposed. Initially, the debonded face sheet acts as an imperfect strut that has some rotational flexibility at its ends, $x_1 = \pm\ell_0/2$. Since the interface is very rigid, the rotational flexibility at the ends results mainly from flexibility of the core. However, as the sandwich column is loaded, the debonded face sheet bends outward and the interface tractions increase. Eventually, the peak stress, $\hat{\sigma}$, is reached and a damage zone starts to develop from the debond crack tip. The damaged zone is softer and adds extra rotational flexibility at the ends of the debond. This makes the face sheet deform like an effectively longer strut and the buckling of it takes place at a lower load.

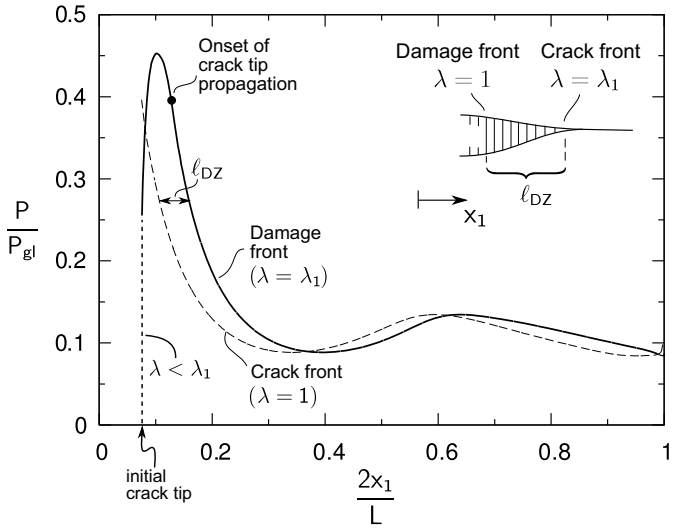

Fig. 11. Location of the damage front ($\lambda = \lambda_1$) along the interface is given by the solid line. Location of the crack front ($\lambda = 1$) is given by the dashed line.

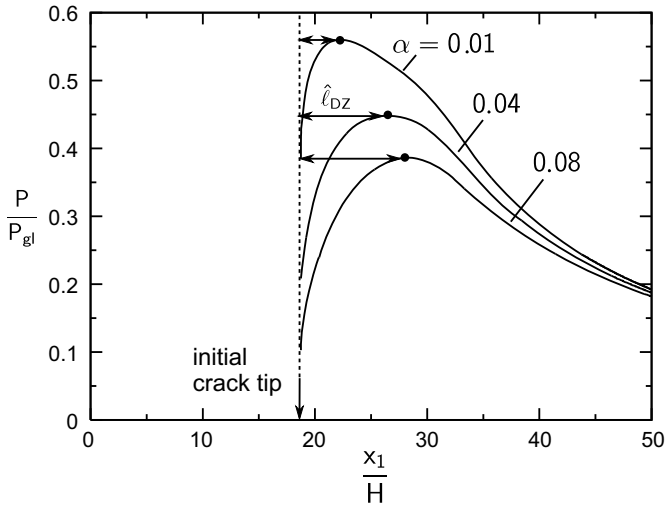

Fig. 12. Influence of α on the damage zone developing at the debond crack tip.

3.5. Influence of the non-dimensional interface fracture toughness on the overall response

The results in the previous section have shown how the debond growth results in a structure that is very sensitive to imperfections and collapses by a snap-back mechanism. In this section we investigate how the highly unstable collapse behavior of the sandwich column (illustrated in Fig. 7) is influenced by the non-dimensional interface fracture toughness, Γ/E_fH. The imperfections are as in case (a), i.e., $\alpha = \beta = 0.01$.

The non-dimensional interface fracture toughness is modified by changing the critical opening u^* and the peak stress $\hat{\sigma}$ proportionally, see Fig. 13a. For instance, to accommodate a factor ϕ increase of Γ/E_fH the parameters $\hat{\sigma}$ and u^* are both increased by a factor $\sqrt{\phi}$. Figs. 14–16 show the normalized compressive load, P/P_{gl}, against $\Delta L/L$, for different non-dimensional interface fracture toughness values and different initial debond lengths. Results for values of Γ/E_fH ranging from 10^{-6} to ∞ are shown in the figures.

The example in Fig. 7 illustrated that the collapse comprised two snap-backs. The present results (Figs. 14–16) show that increasing the values of the non-dimensional interface fracture toughness raise the post-buckling response and ultimately it reaches a limit defined by a curve for $\Gamma/E_fH \to \infty$. Along with this tendency, increasing Γ/E_fH also changes the characteristics of the first snap-back. Taking for instance $\ell_0/L = 0.05$ (Fig. 14), we see that as the fracture toughness is increased the slope of the curve right after the maximum load is changed. Thus, the slope is negative for $\Gamma/(E_fH \cdot 10^{-6}) > 1000$. From a practical point-of-view this implies that the structure is stable under prescribed displacement. Taking instead $\ell_0/L = 0.1$ (Fig. 16), we see that while $\Gamma/(E_fH \cdot 10^{-6}) = 20$ results in a snap-back, the snap-back has disappeared for

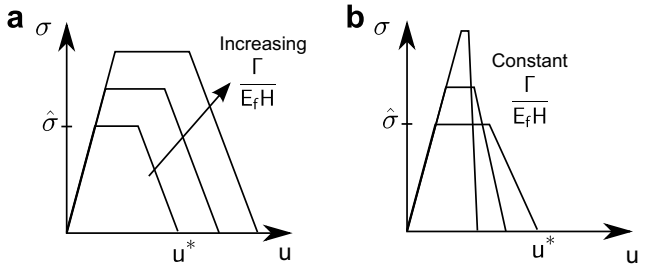

Fig. 13. Modification of the cohesive law for the parameter studies: (a) The work of separation is modified by varying the critical separation, u^*, and the maximum cohesive stress $\hat{\sigma}$ proportionally. (b) $\hat{\sigma}$ and u^* are varied inversely proportional so the work of separation is kept constant.

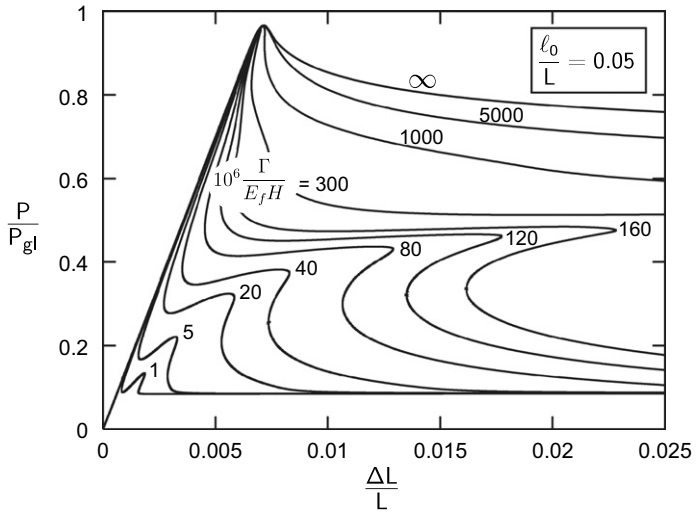

Fig. 14. Response of a sandwich column with a debond of length $\ell_0/L = 0.05$ and different interface fracture toughness values.

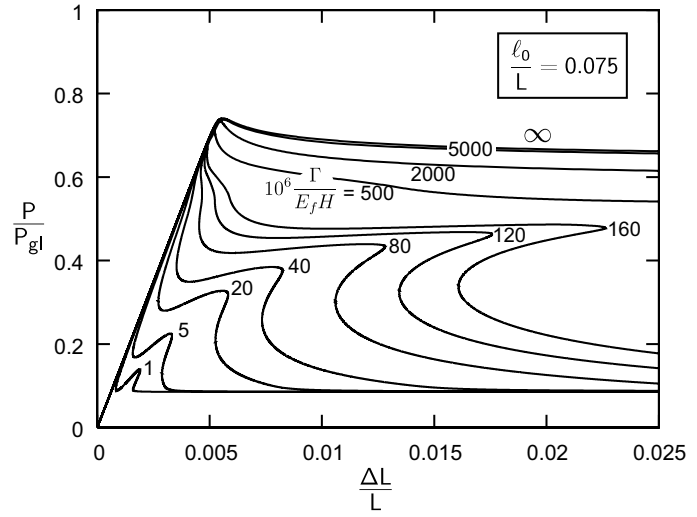

Fig. 15. Response of a sandwich column with a debond of length $\ell_0/L = 0.075$ and different interface fracture toughness values.

$\Gamma/(E_f H \cdot 10^{-6}) = 80$. These two examples show the general trend that the longer the debond is, the less interface fracture toughness is needed to ensure that it is stable under displacement-control.

The non-dimensional interface fracture toughness also influences the occurrence of a second snap-back. For instance, in Fig. 15, the sandwich column with $\Gamma/E_f H = 10^{-6}$ experienced the second snap-back at $\Delta L/L = 0.0018$ whereas an interface with $\Gamma/(E_f H) = 40 \times 10^{-6}$ increases this value to $\Delta L/L = 0.008$ which also is larger than the strain level at which the first snap-back sets in ($\Delta L/L = 0.005$).

3.6. Influence of the peak stress and the critical separation of the interface

In Figs. 14–16 the increase of the interface fracture toughness was accommodated by a proportional increase of the interface parameters. In the present section the response of the sandwich column is computed with different combinations of the critical separation, u^*, (see Eq. (5)) and $\hat{\sigma}$ while $\Gamma/E_f H$ is maintained at a fixed value, see Fig. 13b. This way of varying the cohesive law represents the effect of changing the type of

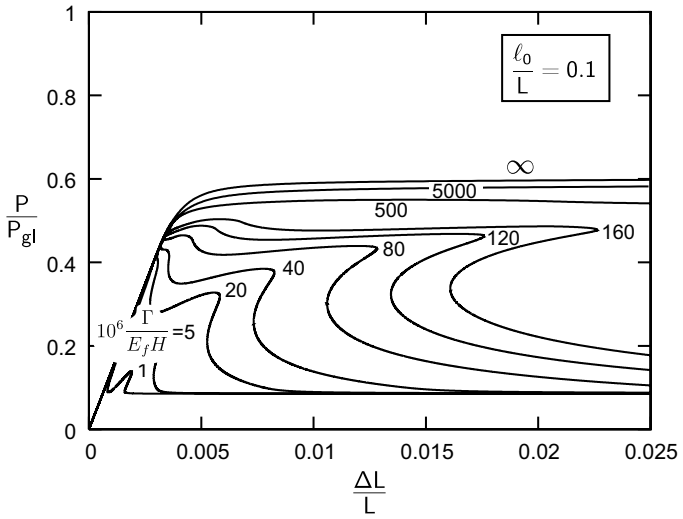

Fig. 16. Response of a sandwich column with a debond of length $\ell_0/L = 0.1$ and different interface fracture toughness values.

fracture mechanism. The actual shape of the cohesive law may also have an appreciable effect on the response (see for instance Chai, 2003, who showed that the strength of a panel with a central hole depends somewhat on the actual shape of the cohesive law). For this study, $\Gamma/(E_f H \times 10^{-6}) = 40$ is selected to represent the interface fracture toughness and the initial debond is selected as $\ell_0/L = 0.075$. The results are shown in Fig. 17 for values of u^* ranging from $0.1H$ to $2.5H$. According to (12) each u^* corresponds to one $\hat{\sigma}$, see Table 2.

The results show that the load carrying capacity increases as u^* decreases (and $\hat{\sigma}$ increases). This trend may be explained as follows: As described in Section 3.4 the finite deflection of the debonded face sheet prior to its buckling, causes interface stresses to build up at the debond crack tip. When these stresses reach the peak stress a softened damage zone starts to develop in front of the crack tip. This zone provides extra rotational flexibility and the debond buckling is pushed forward. However, when the interface peak stress, $\hat{\sigma}$, is increased, a larger finite deflection is needed to initiate damage at the crack tip and therefore the sandwich structure fails at a higher external load level, despite the fact that the fracture toughness is unchanged.

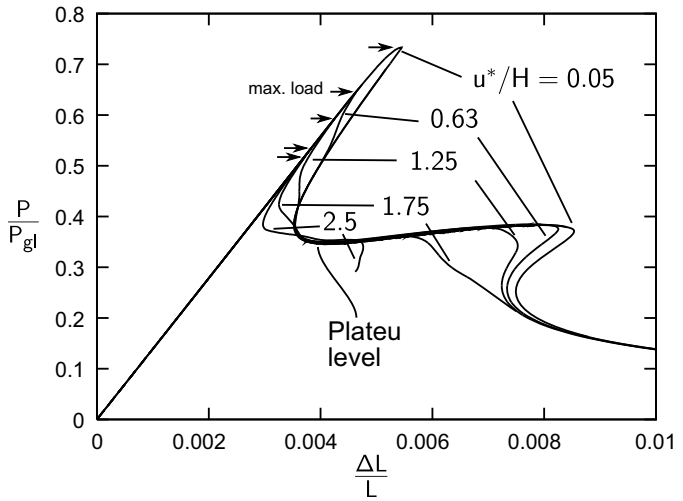

Fig. 17. The response of a sandwich column with an interface fracture toughness of $\Gamma/(HE_f \times 10^{-6}) = 40$. The curves represent different combinations of $\hat{\sigma}$ and u^*. Each u^* corresponds to one $\hat{\sigma}$, see Table 2. The maximum loads achieved are indicated by the arrows.

Table 2
Combinations of u^*/H and $\hat{\sigma}/E_f$ that together with $\lambda_1 = 0.01$ and $\lambda_2 = 0.41$ provide an interface toughness value $\Gamma/HE_f = 40 \times 10^{-6}$

u^*/H	$\hat{\sigma}/E_f$
0.05	14×10^{-4}
0.63	0.91×10^{-4}
1.25	0.46×10^{-4}
1.75	0.33×10^{-4}
2.5	0.23×10^{-4}

Fig. 17 also shows that after the 1st snap-back, all curves coincide at a plateau level that is independent of the actual combination of u^* and $\hat{\sigma}$. However, continued compression of the sandwich column causes the curves to branch off depending on the actual combinations of u^* and $\hat{\sigma}$. Furthermore, the results show that the 2nd snap-back occurs at higher strains as u^* is decreased (or as $\hat{\sigma}$ is increased).

4. Discussion and concluding remarks

This study considered the influence of a global column axis imperfection and a local face sheet imperfection on the compressive strength of a sandwich column containing an initial debond. The results show a strong dependence on the imperfections: The actual combination of the imperfections controls whether the debonded face sheet bends inward and is supported by the core or if it buckles outward and triggers an overall collapse. The type of failure mode selected has a major influence on the load bearing capacity of a sandwich structure. In the case of inward bending, the face sheet does not buckle and the load continues to increase until another failure mechanism limits the load bearing capacity. In the case of a perfectly bonded interface, that limiting mechanism is global buckling. If the interface is able to fracture, the model predicts that interface shear fracture limits the load bearing capacity. However, for a true sandwich structure other failure mechanisms may limit the load bearing capacity, e.g., shear failure in the core, or yielding in the core. Also the face sheet may fail because the compressive strength or the yield stress is exceeded.

Indeed, the amplitude of the face sheet imperfection, α, has a strong influence on the load bearing capacity for the cases where the column fails by outward buckling of the debonded face sheet. For instance, for a debond length $\ell_0/L = 0.05$ and global imperfection $\beta = 0.0035$ the onset of failure is reduced from 93% to 66% of the global buckling load when the face sheet imperfection is increased from $\alpha = 0.01$ to $\alpha = 0.04$. For a real sandwich column having a face sheet thickness $H = 3$ mm the difference between these values corresponds to no more than 90 μm. Face sheet irregularities of this order of magnitude are commonly encountered. When fiber reinforced polymers are used as face sheets a slightly unsymmetrical layup may have imperfections of this magnitude or larger and would seem perfect prior to loading.

A physical explanation of the imperfection sensitivity was sought. A detailed study at the crack tip showed how a damage zone develops from the debonded crack tip during loading of the sandwich column. The crack tip damage zone corresponds to an effectively longer debond and therefore the debonded face sheet reaches its buckling load at a lower load, viz. the sandwich column fails at a lower load. The magnitude of the face sheet imperfection has a significant effect on the extent of the crack tip damage zone and consequently also on the buckling load of the debonded face sheet and the failure load of the sandwich column.

It is not possible to conclude that imperfection sensitivity is only introduced through the damage zone development. As shown in Section 3.2 severe imperfection sensitivity is also present even if the interface is perfectly bonded. That was interpreted as interaction of buckling modes. In a general case, imperfection sensitivity may result from a complex interplay of buckling mode interaction and development of damage at the debond crack tip.

In an experimental context, the imperfection sensitivity implies that severe scatter of the load bearing capacity can be expected. Other structures that are very sensitive to imperfections such as circular cylindrical shells also exhibit large experimental scatter. For these structures, the imperfection sensitivity has lead to the practice of using a knock-down factor for the strength to achieve more useful engineering predictions of strength (Brush and Almroth, 1975).

The properties of the interface (the cohesive zone parameters) clearly has an influence on the overall collapse response of sandwich structures. To understand the influence in greater detail, we investigated the effect of interface toughness on the collapse mechanism. Generally, increasing the interface toughness was shown to have a stabilizing effect on the collapse. In some cases, increasing the (non-dimensional) interface fracture toughness changed the snap-back into a stable collapse, where both load and strain are monotonically increasing. This was seen for the longest crack lengths analyzed, $\ell_0/L = 0.1$, in Fig. 16. For the shorter crack lengths ($\ell_0/L = 0.075$ and $\ell_0/L = 0.05$, Figs. 14 and 15) increasing the interface toughness can change the snap-back curve into an unstable curve that displays a continuously increasing end-displacement but a decreasing load during the collapse. The curves in Figs. 14–16 show that as the initial crack length is increased a lower (non-dimensional) interface fracture toughness is required to avoid the 1st snap-back.

Acknowledgments

The author wish to acknowledge Prof. Viggo Tvergaard and Dr. Lars P. Mikkelsen for inspiring discussions. The work was supported by the Frame Work Programme "Interface Design of Composite Materials" (Danish Research Council (STVF)), Grant No. 26-03-0160.

References

Allen, H., 1969. Analysis and Design of Structural Sandwich Panels. Robert Maxwell M.C.,M.P., London.
Bao, G., Suo, Z., 1992. Remarks on crack bridging concepts. Applied Mechanics Review 45 (8), 355–366.
Barenblatt, G., 1959. Equilibrium cracks formed during brittle fracture rectilinear cracks in plane plates. Journal of Applied Mathematics and Mechanics 23 (4), 1009–1029.
Bazant, Z., Beghini, A., 2004. Sandwich buckling formulas and applicability of standard computational algorithm for finite strain. Composites Part B: Engineering 35 (6–8), 573–581.
Bazant, Z., 2003. Shear buckling of sandwich, fiber composite and lattice columns, bearings, and helical springs: paradox resolved. Journal of Applied Mechanics, Transactions ASME 70 (1), 75–83.
Blackman, B., Hadavinia, H., Kinloch, A., Williams, J., 2003. The use of a cohesive zone model to study the fracture of fibre composites and adhesively-bonded joints. International Journal of Fracture 119 (1), 25–46.
Brush, D., Almroth, B., 1975. Buckling of Bars, Plates, and Shells. McGraw-Hill Book Company, New York.
Cantwell, W., Scudamore, R., Ratcliffe, J., Davies, P., 1999. Interfacial fracture in sandwich laminates. Composites Science and Technology 59 (14), 2079–2085.
Chai, H., 2003. Interfacial mixed-mode fracture of adhesive bonds undergoing large deformation. International Journal of Solids and Structures 40 (22), 6023–6042.
Dugdale, D., 1960. Yielding of steel sheets containing slits. Journal of the Mechanics and Physics of Solids 8 (2), 100–104.
Fleck, N., Sridhar, I., 2002. End compression of sandwich columns. Composites Part A: Applied Science and Manufacturing (Incorporating Composites and Composites Manufacturing) 33 (3), 353–359.
Frostig, Y., 1998. Buckling of sandwich panels with a flexible core-high-order theory. International Journal of Solids and Structures 35 (3–4), 183–204.
Herrmann, A.S., Zahlen, C.Z., Zuardy, I., 2006. Sandwich structures technology in commercial aviation—present applications and future trend. In: Sandwich Structures 7: Advancing with Sandwich Structures and Materials. Aalborg University, pp. 13–26.
Huang, H., Kardomateas, G., 2002. Buckling and initial postbuckling behavior of sandwich beams including transverse shear. AIAA Journal 40 (11), 2331–2335.
Hunt, G.W., Da Silva, L.S., Manzocchi, G.M.E., 1988. Interactive buckling in sandwich structures. Proceedings of The Royal Society of London, Series A: Mathematical and Physical Sciences 417 (1852), 155–177.
Hutchinson, J., Evans, A., 2000. Mechanics of materials: top-down approaches to fracture. Acta Materialia 48 (1), 125–135.
Jeelani, S., Carlsson, L., Saha, M., Islam, S., Mahfuz, H., 2005. Buckling of sandwich composites; effects of coreskin debonding and core density. Applied Composite Materials 12 (2), 73–91.
Kim, S., Sridharan, S., 2005. Analytical study of bifurcation and nonlinear behavior of sandwich columns. Journal of Engineering Mechanics 131 (12), 1313–1321.
Kwon, Y., Yoon, S., 1997. Compressive failure of carbon-foam sandwich composites with holes and/or partial delamination. Composite Structures 38 (1–4), 573–580.
Legarth, B.N., 2004a. Fracture and damage with plastic anisotropy. Ph.D. Thesis, DCAMM, Report No. S91, Technical University of Denmark.
Legarth, B., 2004b. Unit cell debonding analyses for arbitrary orientation of plastic anisotropy. International Journal of Solids and Structures 41 (26), 7267–7285.
Li, S., Thouless, M., Waas, A., Schroeder, J., Zavattieri, P., 2005. Use of a cohesive-zone model to analyze the fracture of a fiber-reinforced polymer-matrix composite. Composites Science and Technology 65 (3–4), 537–549.

Needleman, A., 1987. A continuum model for void nucleation by inclusion debonding. Transactions of the ASME. Journal of Applied Mechanics 54 (3), 525–531.

Østergaard, R., Sørensen, B., ndsted, P.B., 2006. Interface fracture toughness of sandwich structured loaded under mixed mode loading. Journal of Sandwich Structure and Materials 47 (6), 813–824.

Prasad, S., Carlsson, L., 1994. Debonding and crack kinking in foam core sandwich beams-i. analysis of fracture specimens. Engineering Fracture Mechanics 47 (6), 813–824.

Schellekens, J., De Borst, R., 1993. On the numerical integrations of interface elements. International Journal for Numerical Methods in Engineering 36 (1), 43–66.

Somers, M., Weller, T., Abramovich, H., 1992. Buckling and postbuckling behavior of delaminated sandwich beams. Composite Structures 21 (4), 211–232.

Thomsen, O.T., 2006. Polymer composites materials for wind power turbines. In: Proceedings of the 27th Risø International Symposium on Materials Science. Risø, Danish National Laboratory, pp. 97–114.

Tvergaard, V., 1976. Effect of thickness inhomogeneities in internally pressurized elastic–plastic spherical shells. Journal of the Mechanics and Physics of Solids 24 (5), 291–304.

Tvergaard, V., 1990. Effect of fibre debonding in a whisker-reinforced metal. Materials Science and Engineering A: Structural Materials: Properties, Microstructure and Processing A125 (2), 203–213.

Tvergaard, V., Hutchinson, J., 1992. The relation between crack growth resistance and fracture process parameters in elastic–plastic solids. Journal of the Mechanics and Physics of Solids 40 (6), 1377–1397.

Tvergaard, V., Hutchinson, J., 1993. The influence of plasticity on mixed mode interface toughness. Journal of the Mechanics and Physics of Solids 41 (6), 1119–1135.

Vadakke, V., Carlsson, L., 2004. Experimental investigation of compression failure of sandwich specimens with face/core debond. Composites Part B: Engineering 35 (6-8), 583–590.

Van Der Neut, A., 1973. The sensitivity of thin-walled compression members to column axis imperfection. International Journal of Solids and Structures 9 (8), 999–1011.

Wadee, M.A., 2002. Localized buckling in sandwich struts with pre-existing delaminations and geometrical imperfections. Journal of the Mechanics and Physics of Solids 50 (8), 1767–1787.

Wadee, M.A., Blackmore, A., 2001. Delamination from localized instabilities in compression sandwich panels. Journal of the Mechanics and Physics of Solids 49 (6), 1281–1299.

Zenkert, D., Shipsha, A., 2005. Compression-after-impact strength of sandwich panels with core crushing damage. Applied Composite Materials 12 (3–4), 149–164.

Zenkert, D., 1995. An Introduction to Sandwich Construction. Engineering Materials Advisory Services Ltd., London.

Solid Mechanics

Department of
Mechanical Engineering

Technical University
of Denmark

Nils Koppels Allé, Building 404
DK-2800 Kgs. Lyngby, Denmark
Phone + 45 4525 4250
Fax + 45 4593 1475
info.fam@mek.dtu.dk
www.mek.dtu.dk

ISBN 978-87-89502-67-0

DCAMM
Danish Center for Applied
Mathematics and Mechanics
Nils Koppels Allé, Building 404
DK-2800 Kgs. Lyngby, Denmark
dcamm@dcamm.dk
www.dcamm.dk
ISSN 0903-1685